Aperture Synthesis Studies of the Chemical Composition of Protoplanetary Disks and Comets

Thesis by

Chunhua Qi

In Partial Fulfillment of the Requirements

for the Degree of

Doctor of Philosophy

California Institute of Technology

Pasadena, California

2001

(Defended August 21^{st}, 2000)

For my parents Shujia and Siping

and for Yan

Acknowledgements

There are many people to thank for their support and encouragement, without whom this thesis would have not been possible. First of all I would like to thank Geoff Blake, as my thesis advisor, for guiding me through my five years at Caltech. His deep understanding of chemistry and physics, and his fascination with astronomy and the earth sciences, are what have inspired me most. While allowing and encouraging me to work independently, he was always ready to offer helpful suggestions and insightful comments. In spite of his many responsibilities, he was never too busy to give detailed comments (including correcting my naive grammar mistakes) on my papers or simply to chat. I truly believe I could not have had a better advisor, and his attitude towards science, education and even personal life will serve as a role model for me in the years to come.

I thank other members of my Thesis Advisory Committee, Mike Brown, Anneila Sargent and Dave Stevenson, for their useful criticisms and suggestions, and general enthusiasm for the work included in this thesis. I am especially grateful to Anneila Sargent, Director of Owens Valley Radio Observatory, for her tireless efforts on behalf of the Caltech millimeter group and for her support of my work and several conference trips. I also would like to thank Dave Koerner, though not part of my thesis committee, for his stimulating comments on my thesis.

I wish to express my heart-felt gratitude to my academic advisors, Bruce Murray and Yuk Yung, for all their help and encouragement throughout my entire graduate student life.

This thesis is based on the immensely successful operation of the Owens Valley Millimeter Array. I am deeply thankful for the open-minded operation of the telescopes, from which I have learned so much that I will appreciate it my whole life. I am especially grateful to Nick Scoville, for his intuition regarding science and software development for interferometry, and for his humor and delightful manner which made a foreigner like me feel at home in millimeter group meetings. I would like to thank the past and present engineering and technical staff at the observatory: David Woody, Steve Scott, James Lamb, David Hawkins, Mark Hodges, Hemant Shuka, Ray Finch, Ron Lawrence and Curt Giovanine. I am also thankful for my fellow millimeter group members, especially for our extensive discussions about

array operations, data acquisition and reduction: Aaron Evans, David Frayer, Shardha Jogee, Ralf Launhardt, Vince Mannings, Kevin Marvel, Kazushi Sakamoto, Eva Schinnerer, Leonardo Testi and Fabian Walter. A special word of thanks must go to Andrew Baker, John Carpenter and Debra Shepherd who taught me patiently and carefully about array operations and explained everything they knew about the array. I am afraid I tested their good nature by coming to them with any number of observational questions.

My personal thanks go to Eugene Chiang, Jackie Kessler and Sheng-Yuan Liu for their friendship and dedication. Our lively discussions on every topic made me comfortable, like talking in Chinese.

It has been a great pleasure to be a student in the Planetary Science option at Caltech. I would like to thank both Divisions in which I have worked – Geological & Planetary Sciences and Math, Physics & Astronomy – for providing resources and funding for my research throughout this PhD. I think I was very lucky to be admitted to GPS: I went to Baja California to learn Geology; I used UARS satellite data from JPL to study ozone chemistry; I enjoyed learning about our understanding of the fascinating range of surfaces and atmospheres of solar system objects; and, finally, I could easily access OVRO to pursue my thesis research in astronomy. This Division offered me so many opportunities, and it is clear that I could only learn about one percent of them over my whole life, much less the five short years of my stay. I would like to thank all the faculty mentioned above and also Peter Goldreich, who makes you believe you can enjoy science and sports together your whole life; to Duane Muhleman, who taught "nonsense" stuff which made sense later; to Andy Ingersoll, "shall we go to play table tennis or go back to Red Spot of Jupiter ?"; and to Mark Allen, "this is fine but you can accomplish much better!".

Graduate school life can be a dreary existence, so I thank my fellow talented graduate students for making it a pleasant experience overall. To name a few: Dave Kass, Liz Moyer, Anton Ivanov, Hui Zhang, Zhiming Kuang, Mark Roulston, Antony Toigo, Sarah Stewart, Antonin Bouchez ... Kay Campbell, Irma and Mike Black and Leticia Calderon did everything to make our life easy and free of the administration and computer worries.

Finally I would like to thank the Submillimeter Array project of the Smithsonian Astrophysical Observatory and the Institute of Astronomy and Astrophysics of the Academia Sinica of Taiwan, who bravely employed me as a Postdoctoral Fellow, so that I can continue my research with another instrument on the cutting edge of technology. My special thanks

go to Jim Moran, Director of the SMA, and Paul Ho, SMA project scientist and my direct boss, who offered me a great office and computer with which to polish my thesis, and who solved my visa problem which plagued me greatly after graduation. I've had useful discussions of relevant astrophysical issues with Ted Bergin, David Wilner, Qizhou Zhang, Mark Gurwell, Tyler Bourke and Phil Myers at the CfA. I benefited a great deal from on-site testing through discussions with Masao Saito, Eric Keto, Jun-Hui Zhao, Nimesh Patel, TK Sridharan, Satoki Matsushita, Kazushi Sakamoto(again) and Tak Tsutsumi. Some of their thoughts are reflected in the thesis.

I thank my beloved family whose love and encouragement were extremely important to me; my parents for their instructions to "be a man first"; my brother for reviving my interest in science when I thought I would play soccer and table tennis for my whole life; and my wife Yan for her love.

The OVRO Millimeter Array is operated by the California Institute of Technology under funding from the National Science Foundation (AST99-81546). Additional support from the NASA Origins of Solar Systems Program is gratefully acknowledged.

Abstract

There is an intimate connection between the solar nebula and the interstellar medium from which it formed. Improvements in observational methods have now made it possible to directly observe planet-forming environments around young stars and to better characterize the most primitive relics of planetary growth in our own solar system. This thesis describes one such method, aperture synthesis imaging using the Owens Valley Radio Observatory (OVRO) Millimeter Array, and its application to the chemical composition of circumstellar accretion disks and comets.

Circumstellar disks and envelopes around currently forming stars have become the subject of increasingly detailed investigations with high spatial resolution astronomical techniques. To date, however, little is known about the cosmochemical evolution of the gases, ices, and dust grains that form the building blocks from which planetary systems are assembled. A fuller understanding of the details of disk chemistry requires images of several species in each important chemical family (C-, N-, O-, and S-bearing) with the kind of sensitivity, dynamic range, and high spatial resolution that has only recently become possible with (sub)millimeter-wave interferometric arrays. The observations presented in this thesis concentrate on $\lambda\sim3$ mm transitions of HCN/HCO^+ and ^{13}CO/CN in LkCa 15, GM Aur, MWC 480, and HD 163296. These disks were chosen based on their large spatial extent, Keplerian kinematic patterns, and strong CO emission. Two surround classical T Tauri stars and two encircle Herbig Ae stars, enabling the influence of the central stellar luminosity on the chemical composition of the disk to be investigated. All are well isolated from dense molecular clouds.

Even at a resolution of $2''$ (or a linear scale of $\sim$300 AU at the distance of Taurus and Ophiuchus), the OVRO observations show that the chemistry in circumstellar disks is sensitive to both the central stellar luminosity and the degree of dust settling toward the disk midplane. Abundance ratios such as CN/HCN and HCO^+/CO serve as unique probes of pivotal processes such as photoevaporation or cosmic ray induced ionization. The observed lower limit to the fractional ionization of 10^{-10} is sufficient to support magnetorotational instabilities that are likely to dominate the transport mechanisms in the outer reaches of

protoplanetary disks. CN/HCN gradients in the T Tauri and Herbig Ae star disks appear to be correlated with the local UV radiation field and with the degree of dust settling as judged by recent fits to their spectral energy distributions, illustrating the important role of photochemistry at large disk radii.

The disk emission toward LkCa 15 is particularly intense, with many molecules being detected, including HCN/HCO^+ and their ^{13}C-isotopomers, DCN, CN, HC_3N, CH_3OH, CS, ^{13}CO, and $C^{18}O$. The overall abundance patterns are consistent with recent models of photon-dominated chemistry in the near surface regions of flaring circumstellar disks that also provide a natural explanation for the mid- and far-infrared properties of the disk spectral energy distribution. The strength of the CO emission and the double peaked nature of the CN and HCN distribution, however, is most naturally explained by a cold disk interior underlying the chemically active disk surface(s). Substantial volatile depletion onto grain mantles occurs in the interior, and as a result the emission from molecular lines is a more robust tracer of the disk velocity field than its mass. Finally, the detection of DCN has made possible the first determination of the critical D/H ratio in protoplanetary gas. At present, the data provides an approximate value of 0.01 for the DCN/HCN ratio, a value close to that found in the dark molecular clouds, but one that clearly arises from *in situ* disk chemistry.

Direct ties between accretion disks and the formation of planetary systems can be tested by examining primitive solar system bodies such as comets. Comet Hale-Bopp was observed at OVRO from 1997 March 29 to April 2 in a variety of spectroscopic settings between 3.4 and 1.2 mm. The resulting aperture synthesis millimeter-wave continuum and molecular line images reveal in great detail the inner coma. The millimeter-wave continuum brightness of Hale-Bopp is dominated by emission from dust grains in the coma even with beam sizes of $3''$ and $1''$ at $\lambda = 3$ and 1.3 mm, respectively. An emissivity index of $\beta = 0.5 \pm 0.2$ yields a wavelength independent dust production rate of 2.4×10^5 kg s^{-1} for an assumed $\kappa(1.3\ \mathrm{mm}) = 0.9$ cm^2 g^{-1} and a dust expansion velocity of 100 m s^{-1}. The low value of β is similar to that derived for circumstellar accretion disks. By subtracting a spherically symmetric coma model from the continuum visibilities, the millimeter-wave flux from the nucleus has been isolated, and leads to an estimated radius of 19-22.5 km. The range in size arises primarily from uncertainties in the surface temperature of the nucleus and its millimeter-wave emissivity.

The large size of comet Hale-Bopp accounts for its extraordinary outgassing rates, which permitted the aperture synthesis observations of over 18 millimeter transitions of HCN, DCN, HDO, HC_3N, HNC, HNCO, CS, H_2S, SO, OCS, CO, CH_3OH and CH_3OCH_3. The OVRO Millimeter Array was able to image, for the first time, molecular analogs of the dust jets commonly observed at optical and infrared wavelengths. This is particularly significant for investigating the true composition of comets, since jets are known to lift off large, icy grains from which direct sublimation can occur as they are exposed to the Sun. The production rates derived from the aperture synthesis images are similar to those found by other researchers, and reveal a marked similarity between the composition of Hale-Bopp and that derived for dense molecular clouds, in particular the hot cores observed near massive young stars. In addition, quite substantial D/H fractionations, comparable to the OVRO DCN/HCN measurement in LkCa 15, are found in the jets. While this clearly suggests an evolutionary history in which cometary materials remain at very low temperatures throughout their assemblage and for the bulk of their lives, the complex, kinetically controlled chemistry revealed in the OVRO images of the cold, outer regions of disks around young stars means that it is difficult to characterize cometary volatiles as being primarily "interstellar" or "nebular" in origin.

Contents

List of Figures

List of Tables

Chapter 1 Introduction

There is an intimate connection between the early solar nebula and the interstellar medium from which it formed. My research interests lie in studying these chemical connections. The chemical evolution of solar system materials took place within a wide diversity of physical and chemical environments, as gas and dust were transported from a molecular cloud core to their final destinations in planetary bodies and atmospheres. In order to understand the chemical processing of those materials transferred from the interstellar medium to a mature planetary system, the physical conditions and time scales endured by gas and dust must be known. Improvements in observational methods have now made it possible to directly observe analogs of the early solar system. Indeed, circumstellar disks and envelops around currently forming stars have become the subject of increasingly detailed investigations with high-resolution astronomical techniques (Beckwith & Sargent 1996).

This thesis centers on the use of one such technique, millimeter-wave aperture synthesis or interferometry. At millimeter wavelengths, a variety of molecular line tracers and dust continuum emission serve to characterize the physical and chemical processes at work in the formation of stars and planetary systems. The specific targets of interest here are the accretion disks around the T Tauri stars LkCa 15 and GM Aur and the Herbig Ae stars MWC 480 and HD 163296. These first high spatial resolution measurements of the chemistry in the outer regions of circumstellar disks tell us about the formation and evolution of other protoplanetary nebulae, and by inference about our own. More direct ties between accretion disks and the formation of planetary systems can be tested by examining primitive solar system bodies such as comets and Kuiper belt objects. Comets are among the most pristine remnants of the early solar nebula, and thus provide a historical record of the evolution of ices and gases in the outer solar system. This thesis work has therefore also included a detailed observational study of the inner coma of comet Hale-Bopp. We next briefly outline the current paradigm for the formation of isolated, low mass stars such as the Sun before turning to an outline of the thesis.

1.1 Star Formation and the Origin of the Solar System

Rapid improvements in observational capabilities, coupled with equally dramatic strides in analytical theory and numerical computation, have led to the first broadly accepted outline for the stages associated with the birth of Sun-like stars (Shu et al. 1993; Beckwith & Sargent 1996). Planetary systems are thought to be the natural result of the final dissipation stages of the circumstellar disks that serve as the conduits for mass and angular momentum in young stellar objects. Figure 1.1 presents an overview of the scenario that has been developed, along with some of the simple molecules that can be used as tracers of both the physical conditions and chemical evolution throughout the star formation process.

When enough material has accumulated in a small, dense core such that thermal and magnetic pressure can no longer support the weight of the core against gravity, the collapse of an interstellar cloud begins. So too does the chemical processing of protostellar and protoplanetary gas and dust. Materials forged in the interstellar medium are subjected to many processes, including radiation from the central protostar, interaction with ionized jets and bipolar outflows, and tremendous density and temperature changes as the collapse proceeds. Furthermore, infalling matter impacts directly onto the surface of a circumstellar accretion disk with a velocity that depends sensitively on the radial distance. Disk material accreting at distances smaller than 30 AU from a Sun-like star is unlikely to retain much of its interstellar volatile content, though refractory materials can survive. Most of the gas and dust entry into the disk environment, an analog of the early solar nebula, occurs at distances of order 100 AU, where little processing takes place.

When this infall phase has ceased and the surrounding envelope rendered transparent, the young stars become visible and enter the so called T-Tauri star (TTs) phase. TTs range in mass from 1-3 $M_{\odot}$, and their fluxes at infrared and ultraviolet wavelengths are considerably greater than that expected from the stellar photosphere alone. Herbig Ae stars are somewhat higher mass counterparts to the TTs, and also show strong departures from purely photospheric emission. A large fraction of T Tauri and Herbig Ae stars possess spectral energy distributions, or SEDs, that are dominated by the radiation reprocessing of dusty disks, similar to those expected for forming planetary systems (Beckwith & Sargent 1993). Aperture synthesis imaging of GM Aurigae (GM Aur) was the first to demonstrate that gas was rotationally supported throughout the radial extent of a circumstellar disk

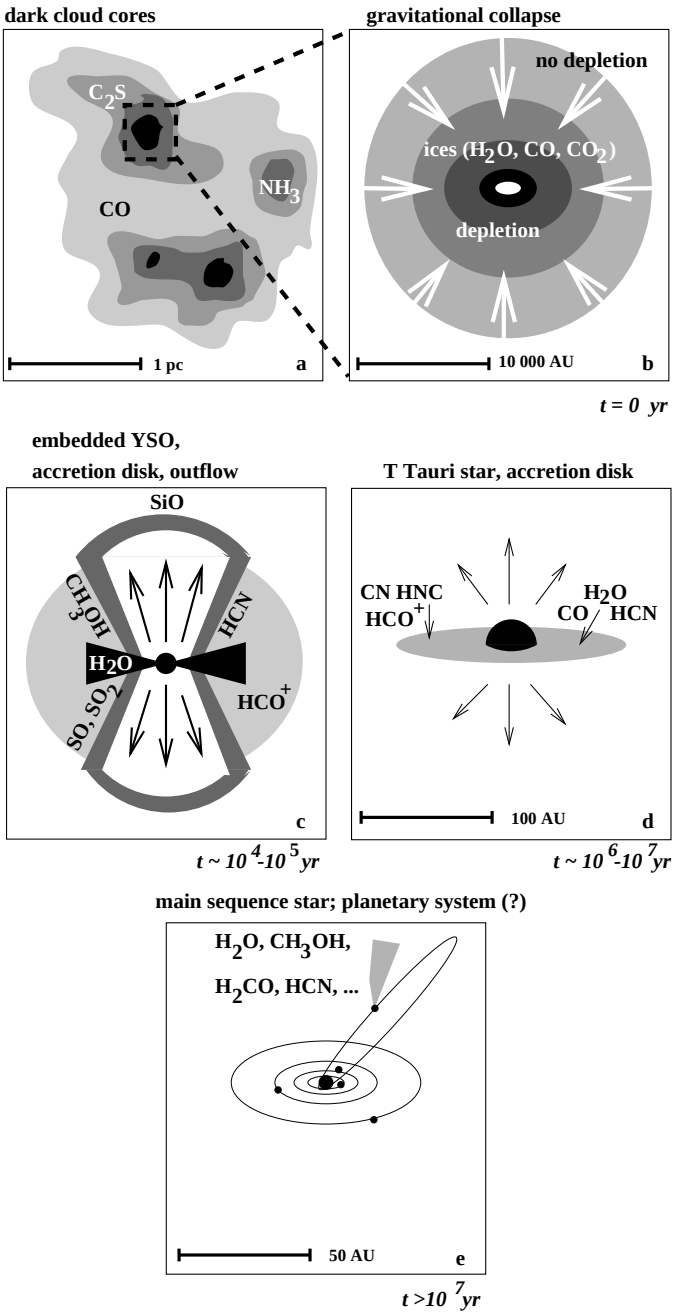

Figure 1.1: A schematic view of the birth of low-mass stars: (a) Dark cloud cores, some 1 pc in diameter, gradually contract via ambipolar diffusion until (b) Magnetic support is overcome and inside-out collapse begins at $t = 0$. (c) In the main accretion, or embedded protostellar phase, which lasts some ∼10,000-100,000 yr, both mass inflow and supersonic outflow occurs. (d) Either through outflow stripping or inward flow of material, the envelope is cleared to leave a young T Tauri star encircled by a residual protoplanetary accretion disk, that, (e) on time scales of several million years, dissipates to leave a mature planetary system (figure by M.R. Hogerheijde, after Shu et al. 1987).

around a classical T Tauri star (Koerner & Sargent 1995). The GM Aur disk is several hundred AU in radius and has a mass several times that required to form our own solar system, with midplane densities so high the volatile depletion onto dust grain mantles is assured. At the disk surface, however, densities are lower and the radiation field much enhanced over that in translucent and dense clouds. Thus, circumstellar disks are extremely heterogeneous, with certain regions dominated by gas phase photoprocessing and others dominated by condensed phase chemistry.

The time scale and associated mechanism(s) by which disks eventually disperse are not yet quantitatively known, but exceedingly important to nebular chemistry and to the formation of planetary systems. Surveys of the near-infrared excesses of T Tauri stars yield dissipation time scale estimates of order a few million years (Strom et al. 1989), but the nature and duration of the dissipation event is not well constrained yet critical to the chemical evolution of young planetary systems. It should be stressed that different mechanisms may operate within the outer and inner regions of disks. Photoevaporation may provide a way to deplete disk gas beyond a critical radius, for example, while accretion onto the star may remove material from the inner disk (Johnstone 2000). The chemical evolution of gas and dust within the disk is poorly characterized observationally, and forms the major topic of this thesis.

Tenuous debris disks are found to survive for several tens, perhaps hundreds, of millions of years after the classical T Tauri phase for at least 15% of young main sequence stars (Habing et al. 1999). Some show evidence for the dynamical influence of larger bodies as well as transient spectroscopic features from infalling objects proposed to be comets perturbed from analogs of our own Kuiper belt (Lagrange-Henri et al. 1988). Just as comets record the evolutionary history of the outer solar system, so these objects should reflect the chemical processing within the disks around young stars. Present instrumentation only permits transient characterization at optical wavelengths, however, and so the observations are only sensitive to the purported comets as they pass extremely close to the star. Information on their original volatile and dust content is therefore lost, and so studies of debris disk chemistry must rely on objects in the outer solar system.

The last few years have seen the appearance of two remarkable comets, comet Hyukutake (C/1996 B2) in the spring of 1996 and comet Hale-Bopp (C/1995 O1) in the spring of 1997. Comet Hyukutake passed extremely close to the Earth, while comet Hale-Bopp was

extraordinarily bright. A number of astronomical facilities, including several millimeter-wave arrays, had been substantially upgraded during the interval between the apparitions of comet Halley in 1987 and those of Hyukutake and Hale-Bopp. As a result, our understanding of the chemical composition of comets has improved tremendously, and detailed comparisons between the composition observed for interstellar gas and dust and that seen in comets are now possible.

1.2 Organization of the Thesis

To provide a common footing for the chapters that follow, Chapter 2 introduces what is expected in the continuum and spectral line observations of disks and comets. Data analysis and reduction procedures are outlined, as are the roles of radiative transfer and modeling.

The third chapter discusses in detail the OVRO observations of chemistry in the disks surrounding the T Tauri stars GM Aur and LkCa 15 and the Herbig Ae stars MWC 480 and HD 163296. Various morphological patterns observed for different molecules are interpreted in terms of the likely physical state and age of the disks.

Chapter 4 presents the results from the OVRO comet Hale-Bopp observing campaign, concentrating on the role of high spatial and temporal resolution observations in determining the outgassing properties of comets and chemistry within the coma. A comparison of comet/ISM chemistry is also presented based on our and other observations.

The final chapter draws upon the general conclusions of Chapters 3 and 4 to speculate on how the next generation of observational capabilities will impact our understanding of star and planet formation. New tools are becoming available across the electromagnetic spectrum, but (sub)millimeter-wave aperture synthesis will play a dominant role in examining the chemical evolution in planet-forming environments. Comments are therefore directed specifically toward the capabilities of the Smithsonian SubMillimeter Array (SMA), the proposed Combined Array for Research in Millimeter Astronomy (CARMA), and the Atacama Large Millimeter Array (ALMA).

Chapter 2 Disks, Comets and Millimeter-wave Interferometry

2.1 Disks and Interferometry

As the means by which mass is transferred from molecular clouds to young stars and as the birth sites of planets, circumstellar accretion disks are the pivotal link between star formation and exoplanetary/planetary science. Primarily through the sustained effort of radial velocity searches, the number of known planets outside the solar system now exceeds 60 [1], but the diversity of masses and orbits so far uncovered challenges the view that our solar system is typical (Marcy et al. 1999). Protoplanet/disk interactions are the likely means by which planetary migration occurs (Ward & Hahn 2000), and so to place the ongoing extrasolar planet detection programs in perspective, it is essential to understand the physical and chemical properties of disks in detail.

Hundreds of disks around stars have been inferred by their near IR excess emission(Lada et al. 2000), and a very small number of disks have been beautifully resolved by HST and ground based scattered light imaging in Orion and Taurus (e.g., O'dell & Wong 1996; Padgett et al. 1999b; Koresko et al. 1999). The geometries needed for such studies are rare, however, and over the past several years the presence of disks around many T Tauri and Herbig Ae stars has been confirmed by detailed (sub)millimeter continuum and line images, which show gas in Keplerian rotation (e.g., Koerner & Sargent 1995; Dutrey et al. 1996; Mundy et al. 1996; Mannings & Sargent 1997, 2000 see Sargent 1996 for a review). Such long wavelength studies are general and limited only by sensitivity because they directly detect emission from the bulk of the cold material in disks, and have revealed that their overall masses ($\sim 10^{-3} - 10^{-1}$ $M_\odot$) and sizes ($\sim$ 100 AU) are comparable to those inferred for the primitive solar nebula. Nevertheless, our quantitative understanding of the physical properties of such disks — in particular their sizes, radial and vertical temperature and density structures, and gas survival time scales — and their chemical evolution has been,

[1] www.cnn.com/2001/TECH/space/04/05/new.planets/index.html

until recently, poor, due to their small angular size compared to the resolution typically available at (sub)millimeter wavelengths with single dish telescopes.

Aperture synthesis mapping at millimeter wavelengths offers a particularly effective way to investigate circumstellar accretion disks. The spatial resolution achievable with currently-operating millimeter-wave interferometers, $\lesssim 0.''5$, corresponds to 70 AU at the nearest star-forming molecular clouds, sufficient for initial star/disk studies. Disk material at a typical radius of 100 AU with a temperature of 20-30 K will radiate preferentially at millimeter wavelengths, in which a rich selection of spectral lines are accessible for observation. The morphology of the circumstellar gas, and an independent estimate of disk mass, can be derived from these spectral line measurements. Interferometer maps of the millimeter-wave continuum emission from circumstellar particles constrains the dust morphology and mass. The temperature and density structure, as well as disk chemistry, can be established through high resolution mapping in different molecular species and isotopes. Molecular line interferometry also has the advantage of enabling investigations of disk velocity structure. Moreover, because aperture synthesis measurements are insensitive to relatively constant, large-scale emission, contributions by the remnant parent clouds are expected to be minimal (Sargent & Beckwith 1994). The major challenge poised by disks to interferometry is their size. The brightness temperature sensitivity of an interferometric map scales inversely with the square of the synthesized beam diameter. Thus, the very small beams that are needed to investigate the thermal emission from the inner regions of circumstellar disks demand arrays with large maximum dimensions and superb sensitivity.

2.2 Comets and Interferometry

Comets present a very different suite of challenges to aperture synthesis imaging. As optical and infrared studies have long shown, their comae often extend several degrees on the sky, yet the physical and chemical structure of the near-nucleus environment can be highly anisotropic and time variable due to the presence of jets. As discussed below, with present-sized arrays, earth rotation synthesis must be used to generate beams with acceptable imaging performance. The large overall size and small scale structure/variability of comets makes the interpretation of aperture synthesis data difficult, and as a result it is only within the past decade or so that radio and millimeter-wave observational and data reduc-

tion capabilities have become sufficiently robust to routinely conduct comet studies. From decameter to submillimeter wavelengths, techniques have been developed which probe all of the major cometary components: the nucleus, the dust, the neutral gas and the plasma. Continuum radio observations at millimeter wavelengths are especially sensitive to large dust particles in the coma and thermal emission directly from the nucleus. Although there have been many attempts to detect radio and millimeter-wave emission from comets nucleus, only a few were successful before Hale-Bopp (see de Pater et al. 1998). Millimeter waves also provide a means to observe some cometary molecules that are otherwise difficult to study at shorter wavelengths.

The spatial distribution of the dust and molecular emission from comets can be measured accurately by making use of interferometers if care is taken in the interpretation of the observed flux densities (de Pater et al. 1991). As shown below, the resolution for an interferometer pair is roughly $\frac{\lambda}{D}$, with λ being the observing wavelength and D the projected antenna-pair separation. The resolution in an image is determined approximately by the largest antenna pair separation, while the shortest antenna pair separation determines the "detectability" of large scale structures. That is, source structures that lie on angular scales larger than those sampled by the shortest array spacings are effectively resolved out by the interferometer. For objects such as comets that are known to be quite extended, it is therefore necessary to utilize other observations to constrain the large scale structure or to model the expected interferometric sampling bias if high resolution array configurations are used. Because of this, previous aperture synthesis observations carried out with the VLA and with BIMA most often utilized compact arrays in order to sample large distances from the nucleus. Only a few molecules, mostly OH, CO and H_2CO (see the review by de Pater et al. 1991) were able to be studied.

2.3 Data Analysis and Reduction Procedures

2.3.1 Basic Ideas of Aperture Synthesis

Thompson et al. (1986) and Perley et al. (1989) provide extensive treatments of aperture synthesis in radio astronomy [2]. The basic requirement for aperture synthesis imaging is a

[2]For a concise summary of the theory and practice of millimeter interferometry, see Appendix A of Andrew Baker's thesis (CIT, 2000).

pair of telescopes that are separated by some baseline vector $\vec{B}$. Given a suitable temporal delay that compensates for the different arrival times of a plane wave from the source to the different telescopes, the product of the intensities measured by each telescope is proportional to a single Fourier component of a source's brightness distribution at the observing wavelength λ – in particular, to a component whose spatial frequency depends on $\vec{B}/\lambda$. As the earth rotates under a source, the effective value of $\vec{B}/\lambda$ (that is, the *projected baseline*) changes so that the two telescopes can measure many Fourier components of the sky brightness distribution over the course of several hours. The measured intensity products are complex, having both phase and flux components. These so-called visibilities, and the effective separation of the telescopes, are measured in what is known as the (u, v) plane. Typically, antenna separations or (u, v) distances are measured in $k\lambda$, or units of one thousand times the observing wavelength. For $N \geq 2$ telescopes operating as an array, the number of baselines and sampled Fourier components increases as $N(N-1)/2$. Ideally, with enough telescopes and observing time, nearly all of a source's Fourier components can be measured (that is, the (u, v) plane can be nearly filled), and the original sky brightness distribution, modulo attenuation by the primary beam response of the individual telescopes, can be recovered via the Fourier transform. The angular resolution determined by $\sim B_{max}/\lambda$.

Several non-trivial problems call for special attention, however:

- Sampling of the Fourier plane may be far from complete if the number of baselines is relatively small. For the OVRO Millimeter Array with 6 telescopes, there are 15 different baselines for any suite of telescope locations, or configurations. Typically, several different configurations (with nonredundant baselines) are used to improve sampling of the Fourier plane by cycling the telescopes. The sources are usually observed over the full possible range of hour angles in each configuration. This approach has been used for the studies of circumstellar disks presented in Chapter 3. For rapidly varying objects such as comets, however, only one configuration can be used, and to examine the time variability the range of hour angles observed will necessarily be small. Fortunately, sources at northern declinations can be more easily imaged than those near the equator, and so even with only a single configuration and averaging times of 2-3 hours the emission from comet Hale-Bopp could be successfully imaged.

- Sampling with an interferometer is always incomplete at low spatial frequencies. For telescopes with a diameter D, the projected baselines can never be shorter than D/λ without shadowing (the blocking of radiation received at one telescope by another). An array therefore behaves as a spatial filter, "resolving out" any emission that is smooth and extended on angular scales larger than $\sim D/\lambda$. For sources such as comets that possess very extended comae, this can be a serious problem if it is not accounted for. Observationally, the data taken by millimeter interferometry can be combined with filled-aperture (i.e., single-dish) spectra that are sensitive to spatial frequencies $< D/\lambda$. Assignments of the relative weights for different sets of visibilities can be a serious problem for merging interferometric and single-dish data, but modern data reduction routines have made this a straightforward task. For time variable objects such as comets, it is essential that the single dish and aperture synthesis data be taken simultaneously.

- Atmospheric fluctuations, such as those due to the column densities of water vapor along the observing path, can cause phase drifts and amplitude decorrelation of the incoming signals, and are typically baseline dependent. At millimeter wavelengths the mean atmospheric drift and decorrelation can be minimized by interleaving integrations on the science source with visits to a relatively bright (~ 1 Jy) and nearby ($\Delta\theta \leq 20^\circ$) quasar calibrator. To a limited extent (see Lay 1997), the source and calibrator will see the same atmospheric structure, whose effects on phase and amplitude (i.e., the complex gain) can then be corrected for the source if they are well-measured as a function of time for the stronger proxy. Typically these calibration measurements occur on the several minute to half-hour time scale, and so cannot remove any rapid atmospheric fluctuations. These rapid fluctuations limit the imaging capability of interferometers, just as they limit the seeing at optical and infrared wavelengths. Robust imaging at sub-arcsecond resolution thus requires the millimeter-wave equivalent of adaptive optics.

- The non-linear nature of the Fourier transform required to generate images from the typically sparsely-filled (u, v) plane means that rigorous error propagation is difficult to achieve in the image plane. For truly quantitative results, it is best to fit the observed visibilities to models of the source structure. This is straightforward when

the source structure is simple (Guilloteau & Dutrey 1998), and such an approach is in fact used in the derivation of dust production rates from comet Hale-Bopp that follows. For more complex source structures, however, model fits to a wide variety of phase centers must be attempted, and so most researchers carry out error analyses in the (u, v) plane despite the non-linearities involved.

Different types of tracers have different spectral signatures, with some appearing as sharp spectral features while others emit broad continuum emission with a particular frequency dependence. In the following sections we summarized the data interpretation methods used for continuum and line radiation from protoplanetary disks and comets.

2.3.2 Continuum Observations

Both disks and comets are known to have substantial quantities of dust, and this emission can provide information primarily about the mass of such objects but also their temperature:

- A 1.3 mm continuum survey conducted by Beckwith et al. (1990) in the Taurus-Auriga dark clouds shows that 42% of the TTs therein have detectable emission from small particles. The thermal emission from small particles in disks is optically thin at wavelengths of order 1 mm and is proportional to the total particle mass.

- Recent continuum imaging of comets Hyukutake and Hale-Bopp can only be plausibly explained by the thermal emission from large particles in the coma that have sizes comparable to the observing (sub)millimeter wavelengths (Jewitt & Matthews 1999). Even with the enhanced emissivity provided by large particles, the estimated dust/gas ratio exceeds unity.

Consider the case where the dust emission is taken to be optically thin. As the dust is generally significantly warmer than the cosmic microwave background radiation, we obtain

$$I_\nu = S_\nu \tau_\nu = \frac{2h\nu^3}{c^2} \frac{1}{e^{\frac{h\nu}{kT_{dust}}} - 1} \tau_\nu \quad , \tag{2.1}$$

where we substitute $B_\nu(T_{dust})$ for the source function S_ν. If we now invoke the Rayleigh-Jeans approximation ($h\nu \ll kT_{dust}$) and assume that the optical depth varies with frequency

as ν^{β}, this becomes

$$I_{\nu}(\tau_{\nu}) \propto \frac{2kT_{dust}}{c^2}\nu^{\beta+2} \quad . \tag{2.2}$$

For thermal blackbody emission from a large object, β in (2.2) should be 0, i.e. the index $q = \beta + 2$ should be equal to 2 if fitting a power law $S \propto \nu^{q}$, where S is the observed flux density. As described below, however, the 1.3 mm continuum imaging of Hale-Bopp reveals that even in beams of 1-2$''$ most of the millimeter-wave radiation originates from dust in the comet's coma and not from the nucleus itself. Modeling of the dust emission sampled by the array allows subtraction of this coma emission from the visibilities in order to constrain the thermal blackbody emission from the nucleus. With an assumed emissivity and the surface temperature motivated by related millimeter-wave and infrared studies, an estimate of the nucleus radius is obtained.

Continuum Emission from Comet Hale-Bopp

Continuum emission from Hale-Bopp between 89 and 244 GHz is readily detected by OVRO. At perigee (1.3 AU), a beam width (FWHM) of 1$''$ corresponds to a 1000 km linear distance at the comet. Continuum data designed to be as free of line contamination as possible were collected on 1997 April 2 for λ = 3 mm and 1997 March 31 for λ = 1.3 mm. The resulting peak intensities and integrated fluxes along with their associated errors, including calibration uncertainties, are listed in Table 2.1.

Table 2.1: Comet Hale-Bopp Continuum Emission

Dave (UT)	ν (GHz)	Beam (arcsec)	Total(mJy)	Nucleus(mJy)
1997 March 31	88.1	2.6×1.9	11.5 ± 3.5	1.92 ± 1.8
	91.1	2.4×2.2	10.0 ± 3.0	1.82 ± 2.1
	220.3	1.2×0.8	39.0 ± 10.3	7.62 ± 1.4
	223.3	1.0×0.8	41.2 ± 11.4	8.32 ± 4.2
1997 April 2	101.1	2.5×1.8	12.2 ± 1.54	2.22 ± 1.45

Figure 2.1 shows the naturally weighted, cleaned 101 GHz continuum image from 1997 April 2, where the lowest contour is equal to twice the root mean square (rms) noise in the image. The peak emission is offset from the adopted ephemeris position of the nucleus by about 3$''$ to the east in RA and 3$''$ to the north in DEC. Similar offsets are observed

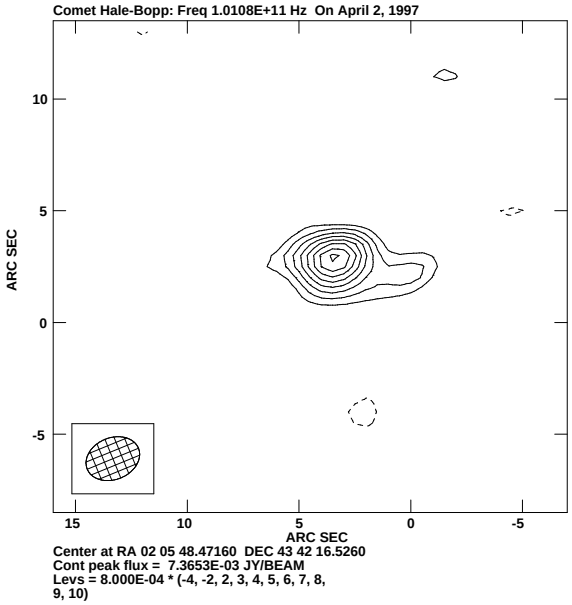

Figure 2.1: OVRO continuum image of comet Hale-Bopp at 101 GHz. The contours start at 1.6 mJy/beam and are spaced by 0.8 mJy/beam. The synthesized beam is shown by the hatched ellipse at lower left.

by de Pater et al. (1998) and Altenhoff et al. (1999). The source of this discrepancy is not known at present, for later solutions to the ephemeris do not remove it. In Figure 2.3 we present the vector-averaged visibility amplitudes as a function of the projected baseline length for Hale-Bopp, averaged in 5-10 kλ wide bins. This plot essentially gives the Fourier transform of the symmetric part of the sky brightness about the phase, or source, center. A point source has a flux independent of baseline length, while the flux of an extended source decreases with increasing (u, v) distance. The flux density clearly increases toward the shorter spacings, as expected for a resolved source.

The measured visibilities represent the sum of the thermal emission from dust in the coma as well as that from the nucleus. In order to isolate the point source flux density from the nucleus, the following three-step procedure has been used:

1. Calculate the sky brightness corresponding to a specified coma model.

2. Subtract this model from the observed visibilities.

3. CLEAN (an AIPS algorithm, other deconvolution software can also be used) the resulting differenced (u, v) data. Any additional point source should then be visible

once the coma emission has been removed.

Continuum Emission from the Coma

According to the three steps described above, it is first necessary to model the visibilities associated with the coma emission. The radio continuum brightness of a cometary coma is determined in part by the size distribution, composition and shape of the dust particles therein. Other important factors are the optical depth of the coma within the synthesized beam, the emissivity of the particles, and the dust production rate. Radio through submillimeter observations of comets Hyukutake (C/1996 B2) and Hale-Bopp are consistent with the bulk of the long wavelength flux arising from large (~millimeter-sized) grains (Jewitt & Matthews 1997, 1999; Altenhoff et al. 1999). In reality, a range of particle sizes is present. So long as the observing wavelength is sufficiently large compared to the range of particle sizes and the emission is optically thin, the determination of the dust mass inside the observing beam is relatively insensitive to the details of the dust size distribution. If the optical depth of the coma exceeds unity, the flux density becomes largely insensitive to the dust mass of the coma, and it becomes difficult to obtain flux density measurements of the nucleus.

Hogerheijde & van der Tak (2000) have developed a two-dimensional Monte Carlo radiative transfer code for the millimeter-wave study of a variety of astronomical sources. This code has been adapted to the study of cometary comae by including additional parameters such as the dust production rate and particle emissivities, and uses as inputs radial distributions in density and temperature that are specified by the user. The generated brightness distribution is then sampled in the (u, v) plane to compare directly with observations. In this way the sky brightness and optical depth within the observing beam can be calculated for a specific coma model. At millimeter wavelengths the emissivity is for the most part set by the coagulation of dust particles, i.e., whether they stick together, and whether they form compact or more porous structures. Previous continuum measurements of comets reveal spectral energy distributions that are quite similar to those inferred for dust in star-forming cloud cores and circumstellar disks (Jewitt & Matthews 1997, 1999). We thus use the emissivity data complied by Ossenkopf & Henning (1994), who combine theoretical models of grain coagulation with laboratory measurements of various candidate materials to predict a mass opacity coefficient of $\kappa_{dust}(1.3 \text{ mm}) = 0.9 \text{ cm}^2/\text{g}$. For a production rate of 3.2×10^5 kg

s^{-1} (Senay et al. 1997) and the adopted millimeter-wave mass opacity, the dust continuum optical depth is 3.9×10^{-3} at 223 GHz. Even smaller optical depths are predicted for longer wavelengths, and so the coma of Hale-Bopp is optically thin for all frequencies accessible to the OVRO Millimeter Array. We next fit our data to derive the dust emissivity and production rate that is consistent with the measured continuum visibilities.

In order to calculate the dust thermal emission from the coma, we use a simple model in which the dust moves radially away at a constant terminal velocity. Hence, the dust density in the coma will decrease with distance, r_c, as r^{-2} for a spherically symmetric outflow. Since the shortest baselines probe extended regions of the comet's coma, they provide the most accurate estimate of the dust density distribution. This density gradient is used along with an isothermal temperature profile (T_{dust} = 300 K) in the Monte Carlo radiative transfer model, and sampled at the appropriate (u, v) spacings to compare with the observed visibilities. If a power law $Q_\nu \propto \nu^\beta$ applies, where Q_ν is the emissivity of the particles at frequency ν, the 3 mm and 1.3 mm data can be used to constrain the index β, for which we find $\beta = 0.5 \pm 0.2$. Jewitt & Matthews (1999) derive a nearly identical value of 0.6 ± 0.13 from JCMT observations, while Altenhoff et al. (1999) calculate an emissivity index of 0.8 from combined array and single dish measurements.

Besides the emissivity of the cometary dust grains, the Monte Carlo model assumes a parameterized Haser (spherically symmetric) distribution For the dust density, or

$$n(\mathrm{kg/m^3}) = n_0(1000\ \mathrm{km})(\frac{r}{1000}\ \mathrm{km})^{-2}$$

where n_0 is the dust density at a distance of 1000 km from the nucleus. The output of the Monte Carlo model is convolved with the same Gaussian beam (that is, using the same (u, v) sampling) that served to restore the cleaned images of the 1.3 mm and 3 mm continuum visibilities. The coma dust fitting is based mainly on the comparison of visibility amplitudes at the shortest spacings observed. The brightness can be fit by a large range in v_{dust} (the dust expansion velocity) and κ_{dust}, but this does not affect the flux vs. (u, v) distribution. Figure 2.2 shows such a fit with $n_0 = 1.9 \times 10^{-10}$ kg/m^3 for $\kappa_{dust} = 0.9$ cm^2/g and v_{exp} = 100 m/s, while Table 2.1 presents the derived flux densities of the nucleus after the model fit to the dust coma emission at 1.3 and 3 mm has been subtracted. The flux densities of the nucleus are consistent with blackbody emission, as shown in next section.

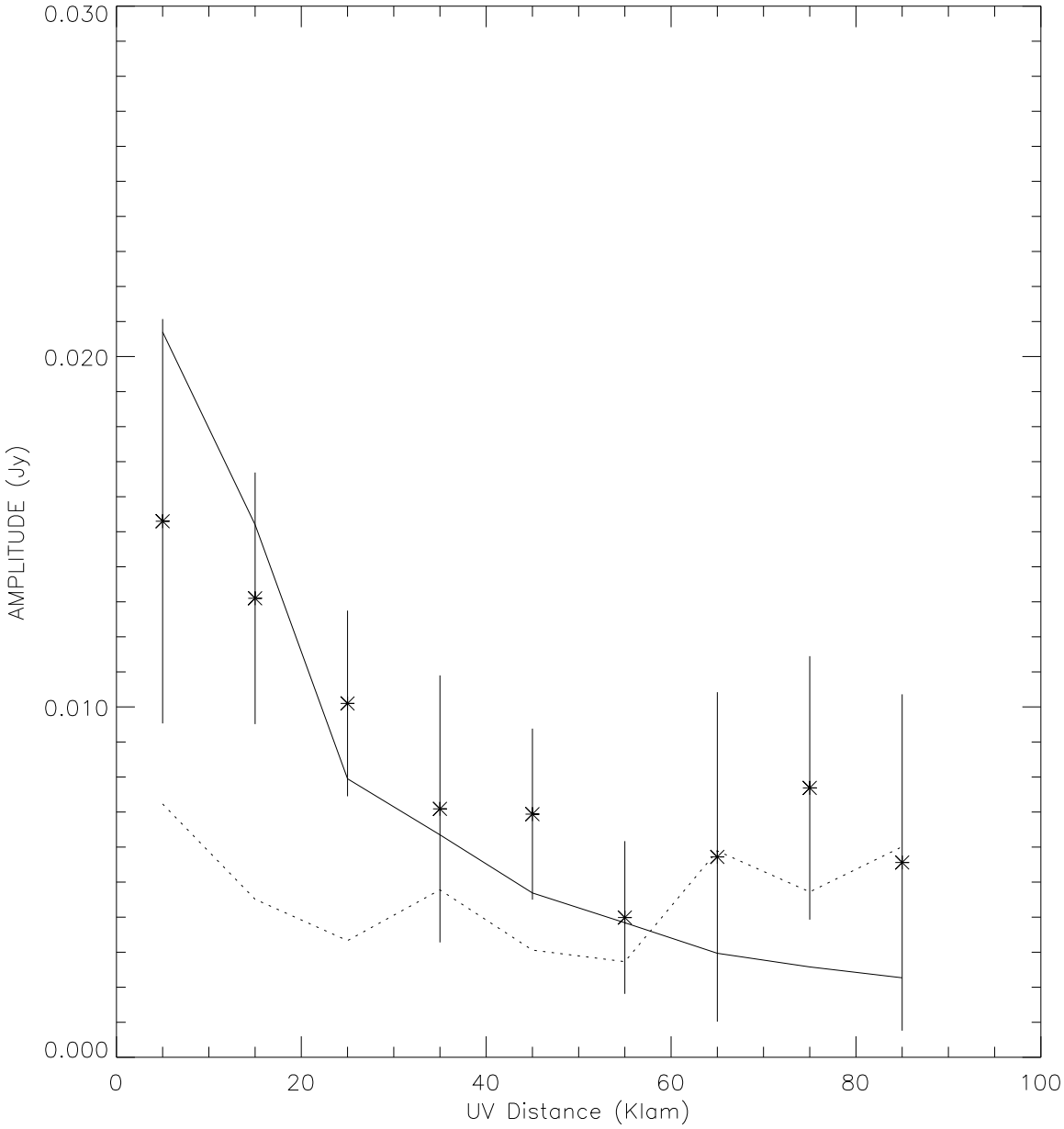

Figure 2.2: Observed visibilities of the coma emission from comet Hale-Bopp with error bars. The solid line shows the result of the Monte Carlo radiative transfer model which is sampled at the appropriate (u, v) spacings to compare with the observed visibilities. The dotted line indicates the noise expectation level of the observations.

Provided the Haser (r^2) dust density approximation of a spherically symmetric outflow holds, the total dust production rate Q can be defined

$$Q(kg/s) = 4\pi r^2(\mathrm{m}^2)\, n(\mathrm{kg/m}^3)\, v_{exp}(\mathrm{m/s}) \quad ,$$

where v_{exp} is the dust expansion velocity. To derive the dust production rate from the estimated dust density distribution, the dust expansion velocity must be estimated. Micron-sized particles should be carried away from the nucleus at the gas expansion velocity (approximately 1.3 km/s for Hale-Bopp near perihelion, Biver et al. 1997a), while the several hundred micron to millimeter-sized particles that dominate the millimeter-wave flux will have much smaller radial velocities (of order 200-50 m/s for ~millimeter-sized grains for Hale-Bopp near perihelion, Jewitt & Matthews 1999). Adopting a value of 100 m/s yields a dust production rate of 2.4×10^5 kg s^{-1} using the dust density $n_0 = 1.9 \times 10^{-10}$ kg/m^3 at 1000 km as derived from the combined 3 and 1.3 mm data set. Other recent estimates of the dust production rate range from 0.8×10^5 kg s^{-1} (Altenhoff et al. 1999) to $1.5 - 1.8 \times 10^6$ kg s^{-1} (de Pater et al. 1998; Jewitt & Matthews 1999). Our measured visibilities are roughly 50% smaller than those observed by de Pater et al. (1998), but are well within the error bars of those reported by Altenhoff et al. (1999). Indeed, we stress that the differences between the reported dust production rates are nearly entirely attributable to various assumptions about the dust mass opacity coefficients and the dust expansion velocity, and not to actual observational differences in the millimeter-wave brightness of Hale-Bopp as seen by various telescopes and arrays.

Thermal Emission from the Nucleus

The flux density of a comet nucleus depends upon its temperature (T), radius (r) and emissivity (ϵ). As we indicate above, in order to isolate this flux density, it is necessary to subtract the model of the coma sky brightness distribution derived above. Specifically, the output of the Monte Carlo model is convolved with the same Gaussian beam (that is, using the same (u, v) sampling) that served to restore the cleaned image in Figure 2.3. The model is then subtracted from the data to yield the difference map shown in Figure 2.3, which represents an upper limit to the point source emission from the nucleus itself. The remaining integrated flux at 3 mm is $\lessapprox$ 2 mJy, while that at 1.3 mm is $\lessapprox$ 8 mJy (Table 2.1,

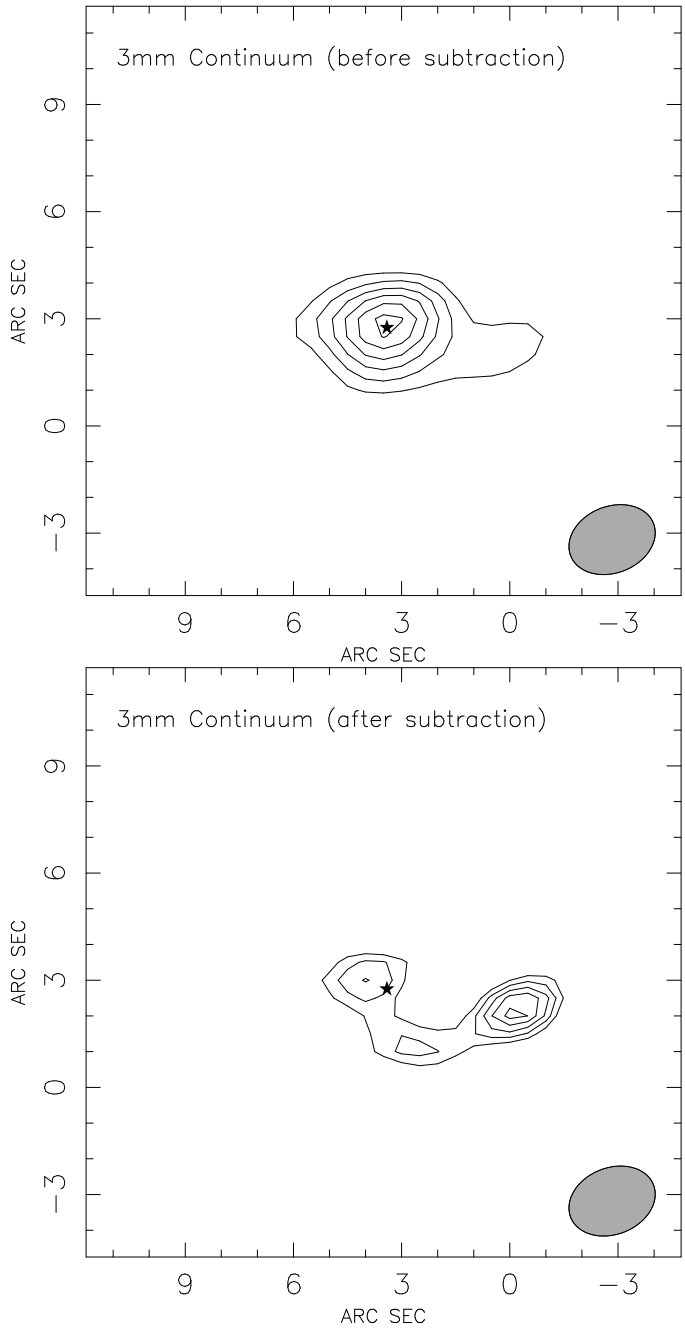

Figure 2.3: Maps of the continuum emission from Hale-Bopp before and after subtraction of the coma emission. The source to the west is associated with jet activity from the nucleus, and so is not subtracted by the Haser (spherically symmetric) model of the coma.

whose error bars include uncertainties in the array calibration and model subtraction).

At millimeter and submillimeter wavelengths, comets are sufficiently warm that the Rayleigh-Jeans limit of the Planck law,

$$B(\nu, T) = \epsilon \frac{2\nu^2}{c^2} kT \quad ,$$

is an excellent approximation for the flux density. From millimeter-wave measurements of the flux densities of the Gallilean satellites and other outer solar system bodies, the millimeter-wave emissivity should be of order $\epsilon = 0.8(+0.1, -0.3)$ (Muhleman & Berge 1991). Although the coma-subtracted images are noisy, they do yield a flux density frequency dependence that is very close to that expected for thermal blackbody emission. The resulting point source fluxes are close to the rms sensitivity of the maps, and so are perhaps most appropriately regarded as estimates of the maximum flux density (and hence maximum size) of the nucleus at 1.3 and 3 mm.

The minimum surface temperature of the nucleus should be set by the sublimation temperature of water-ice (195 K). Given the geocentric distance of $\Delta = 1.359$ AU on 1997 April 2 and $\Delta = 1.344$ AU on 1997 March 31, the flux density can be written as

$$F = B\Omega = B\pi \left(\frac{r}{\Delta}\right)^2 \quad .$$

The nucleus flux densities derived from subtraction of the dust coma model at 101 GHz (2.2 mJy) and in 223 GHz (8.3 mJy) yield a radius of 22.5 km for comet Hale-Bopp, slightly larger than that inferred from VLA observations (Fernandez et al. 1997). The low albedo derived for comet Halley suggests that the surface temperatures of comets may be much higher than that controlled by water ice sublimation, and could be as high as the equilibrium temperature expected for blackbodies at the same heliocentric distance. Near perihelion for Hale-Bopp this would correspond to temperatures of nearly 280 K, in which case the estimated radius would be reduced to $\sim$19 km. A plot of the surface temperature versus the radius of the nucleus is shown in Figure 2.4.

Similar interferometric observations were carried out for comet Hyukutake in the spring of 1996, and resulted in a 3σ upper limit of 8-10 mJy for the thermal continuum at 1.3 mm. The geocentric distance at the time of the observations was only $\Delta = 0.15$ AU, and so the

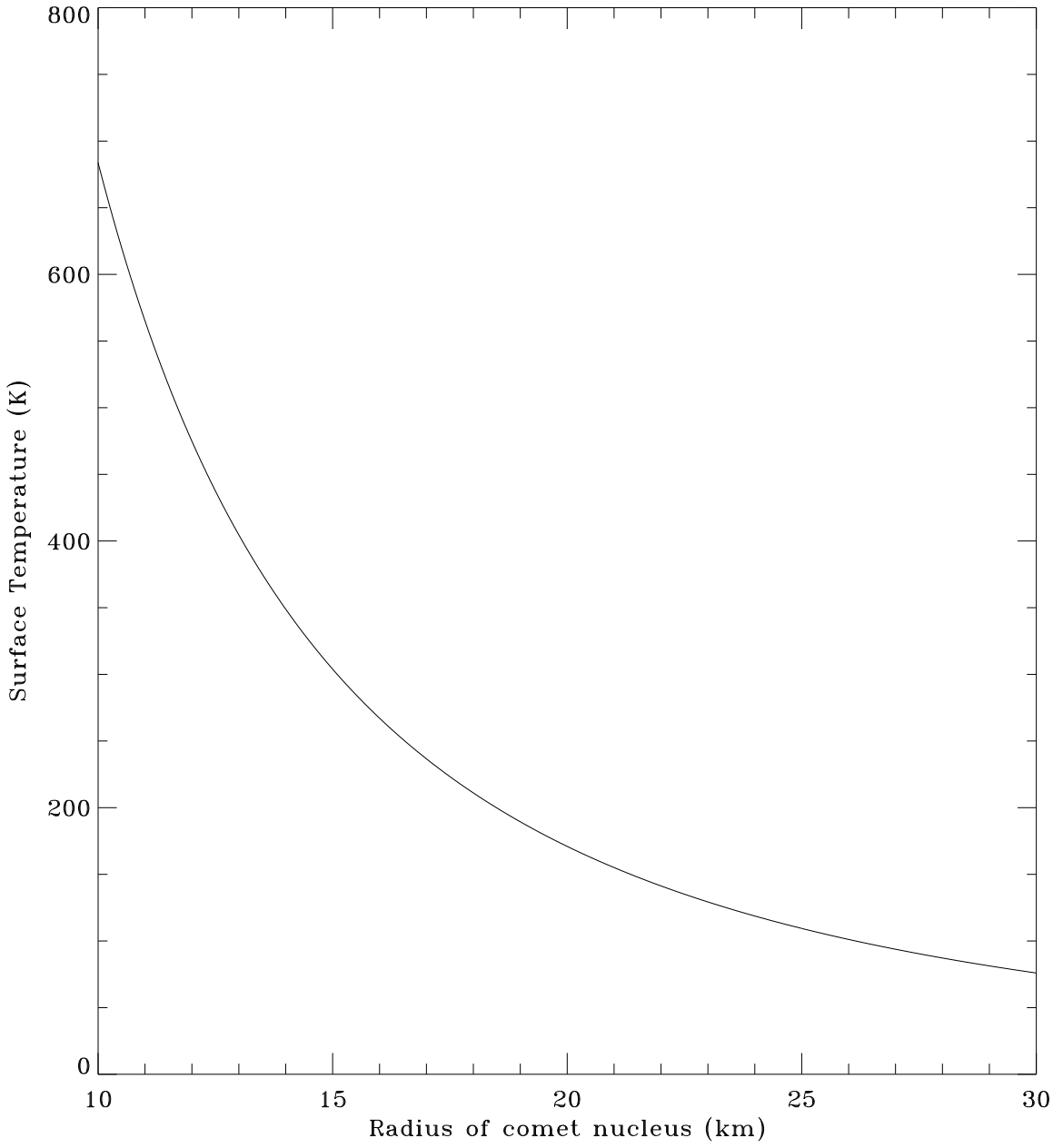

Figure 2.4: Surface temperature versus the radius of the nucleus of comet Hale-Bopp for the $\lambda = 3$ and 1.3 mm OVRO point source flux continuum measurements.

estimated upper limit to the radius of Hyukutake is of order 2 km for a surface temperature of 195 K. This value is similar to other upper limits from thermal continuum measurements (Altenhoff et al. 1999), and is consistent with the size estimated from radar cross-section studies (Harmon et al. 1997).

2.3.3 Continuum Observations of Circumstellar Disks

The thermal emission from circumstellar disks is optically thin at millimeter wavelengths (Beckwith et al. 1990), which provides an excellent way to measure disk masses directly:

$$F_\nu = \int I_\nu d\Omega = \int S_v \tau_v d\Omega = \int \frac{2kT}{\lambda^2} \kappa \Sigma \, d\frac{\sigma}{D^2} = \frac{2kT}{\lambda^2 D^2} KM \quad , \tag{2.3}$$

where $M = \int \Sigma d\sigma$, F_ν is flux density, κ is the mass opacity, Σ is the surface density of the disk and σ is the area of the disk.

More detailed constraints to the density and temperature structure can be derived by fitting the spectral energy distributions (SED) of young star/disk systems. Early models of radiation reprocessing by a passive disk used flat blackbody geometries (Adams et al. 1987), and produce an SED of the form $\nu F_\nu \propto \nu^n$, with an infrared spectral index of $n = \frac{4}{3}$ (Adams et al. 1987 and references therein). Contrary to this prediction, most sources exhibit flattish spectra having $n < \frac{4}{3}$ (see, e.g., Beckwith et al. 1990). Hydrostatic, radiative equilibrium models of passive T Tauri disks predict a flared geometry that intercepts a greater amount of stellar radiation (Kenyon & Hartmann 1987). Such a flared, passive disk divides naturally into two regions: a surface layer that contains dust grains directly exposed to central starlight, and a cooler interior that is encased and diffusively heated by the surface (Chiang & Goldreich 1997; D'Alessio et al. 1998).

In the two-layer formalism, exactly half of the radiation reprocessed by the surface layer escapes directly into space. The remaining half is directed towards the disk interior. The height of the disk photosphere, H, is assumed to be proportional to the vertical gas scale height, h, with a fixed constant of proportionality of 4 in the model of Chiang & Goldreich (1997). If the dust and gas are in interstellar properties and well mixed, the H/h ratio is closer to $\sim$5 for a distance of 1 AU, but decreases monotonically to $\sim$4 at 100 AU. In the numerical models of Chiang et al. (2001), the H/h ratio is fit as a constant parameter. The two-layer model satisfactorily fits the infrared excesses and millimeter wavelength emission

of the T Tauri stars such as GM Aur, as is shown in Figure 2.5. Here we briefly summarize the dependence of the SED on certain disk parameters that are important to molecular line observations and assessments of disk chemistry. For more detailed descriptions of the model, the interested reader is referred to the undergraduate thesis of Moo Kwang Joung (CIT, 2000) and Chiang et al. (2001). Summaries of the disk SED fits to the sources observed at OVRO are presented in Chapter 3.

- Millimeter-wave fluxes are most sensitive to Σ_0 (the surface density at 1 AU), $p \equiv -\frac{d\ln\Sigma}{d\ln a}$, $r_{max,i}$ (the maximum grain radius in the interior) and $q_i \equiv -\frac{d\ln N}{d\ln r}$. The first two variables determine the amount of mass in the cool disk interior at large radius; the latter two variables affect the millimeter-wave opacity in the disk interior.

- In the Rayleigh-Jeans limit, the millimeter-wave opacities are independent of how the total condensible mass in water and silicates is distributed across particle size.

- Radiation at λ = 2-4 mm emerges from optically thin material.

- The radial locations of condensation boundaries in disk surface layers move outward approximately as $T_*^{(4+\beta)/2} \approx T_*^3$. Consequently, as T_* increases, surface emission from water ice diminishes noticeably. The disk interior gradient does not scale quite so cleanly, but is similarly dependent on the stellar luminosity.

- The height of the disk photosphere in units of the gas scale height, H/h, appears to be one of the best constrained parameters from fits to the observed SEDs. Low values of H/h are interpreted to mean that dust in disk surface layers has settled vertically towards the disk midplane. In such disks, the reduced UV opacity away from the disk midplane will greatly increase the importance of photochemical processing.

2.3.4 Spectral Line Observations

Spectral Line Profiles and Jets from Comets

The surfaces of comets in the outer solar system are believed to be covered almost completely by a very thin, fragile layer of highly volatile ices intermixed with dust. This shallow frosting – sometimes called the mantle – begins to sublime directly from the solid state into the surrounding vacuum while the comet is still quite far from the Sun. Comet Hale-Bopp,

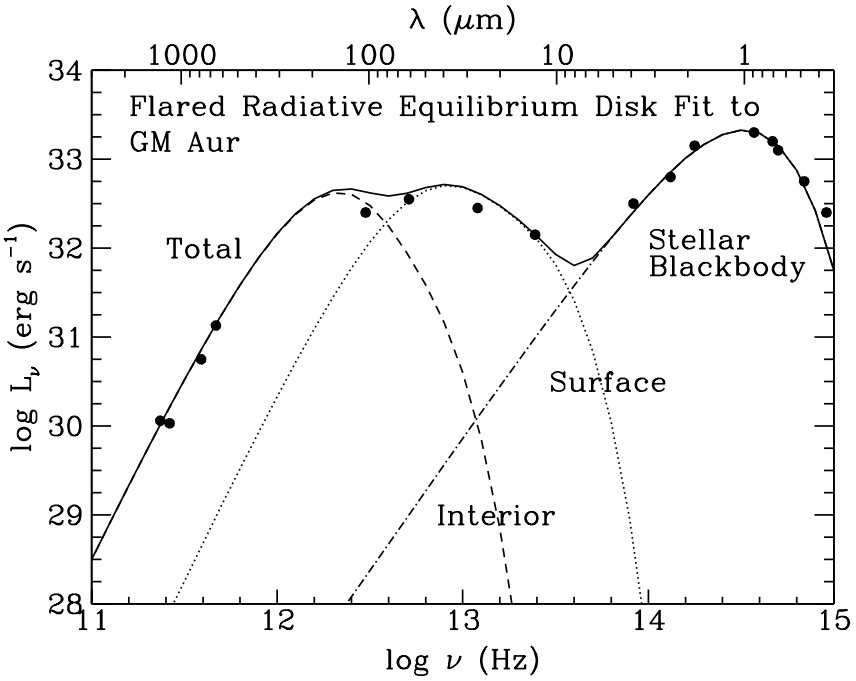

Figure 2.5: Standard two-layer passive circumstellar disk fit to the SED of the T Tauri star GM Aur. From Chiang & Goldreich (1997).

for example, showed signs of activity beyond 7 AU (Jewitt et al. 1996; Biver et al. 1996), while 95P/Chiron has been active beyond 10 AU (Luu & Jewitt 1990). As the comet moves into the inner solar system, the increased solar insolation drives outgassing over the entire sunward surface of the comet, expelling copious amounts of entrapped dust and creating a large, highly reflective coma. Occasionally, the outgassing will selectively drive breaches in the comet's crust that become active when exposed to sunlight – the formation of jets.

The existence of cometary jets has been known for some time, primarily from ground based imaging. In addition, the Giotto and the two Vega spacecraft investigated the near nucleus environment of comet P/Halley. One of the unexpected surprises was that about 90% of the coma gas and dust was shown to be emitted in jet-like features from a few compact, active source regions that comprised only about 20% of the illuminated surface area at the time of the Giotto encounter. It is assumed that the visible jets are caused by the onset and termination of activity as gas- and dust-producing areas on the nucleus come into sunlight and leave it again with each rotation. Thus, visible dust jets are typically used in the determination of nucleus rotation parameters from brightness variability studies.

Similar jet-like features have also been detected in gas phase molecules such as CN. The dust and gas features are typically only a few arc seconds in size at most, and so high spatial resolution observations on time scales short compared to the rotational period are needed to characterize the near surface environment of the nucleus. High spatial and temporal resolution molecular line images over a wide range of heliocentric distances will ultimately be required to acquire a clear understanding of differential outgassing and chemistry in the inner coma of comets.

The exceptionally high production rates of comet Hale-Bopp made possible several long-term observational campaigns, including those that sought to derive the rotational parameters of the nucleus by monitoring jet structures in the inner coma. Figure 2.6 shows the processed images of the central coma of Comet Hale-Bopp taken by one such program (Licandro et al. 1998) using the facilities of the Teide Observatory (Instituto de Astrofisica de Canarias). The images are ordered day-by-day and phased according to the 11.35 hr rotational period to show images for the same orientation of the nucleus and jets over the course of several days. Three spiral jets, labeled A, B, and C, and some expanding shells can be observed as dark, curved structures. Although these images are obtained via the sunlight reflected by dust, that dust is lifted off the nucleus by gas flow, implying that the gas is also emitted in jets, although it disperses more rapidly than does the dust.

The spectral line profiles observed at millimeter wavelengths can be affected by the anisotropic flow associated with jets. The main cause of the broadening of cometary lines is the Doppler shifts produced by various sub-regions within the flow with different line-of-sight components of the outflow velocity (Appenzeller et al. 1984). For a spherically symmetric flow, or Haser model, all lines of site are present within any finite observing beam. Consider, however, the case of a flow restricted to a cone of half angle ω, where the axis of the cone makes an angle ψ with the line-of-sight (Figure 2.7). This problem can be dealt with by determining the angular length of the arc of the emitting ring which is intersected by the flow cone. High spectral resolution and a detailed trigonometric model of the cone are needed to quantitatively analyze the jet information contained within the line shapes and velocity shifts observed at high spatial resolution. The OVRO comet Hale-Bopp data set is still fairly limited in terms of its spectral and spatial resolution, and so only a preliminary analysis is possible (Chapter 4). Future interferometers will do much better.

In order to derive the production rates of different molecules from the observed spectral

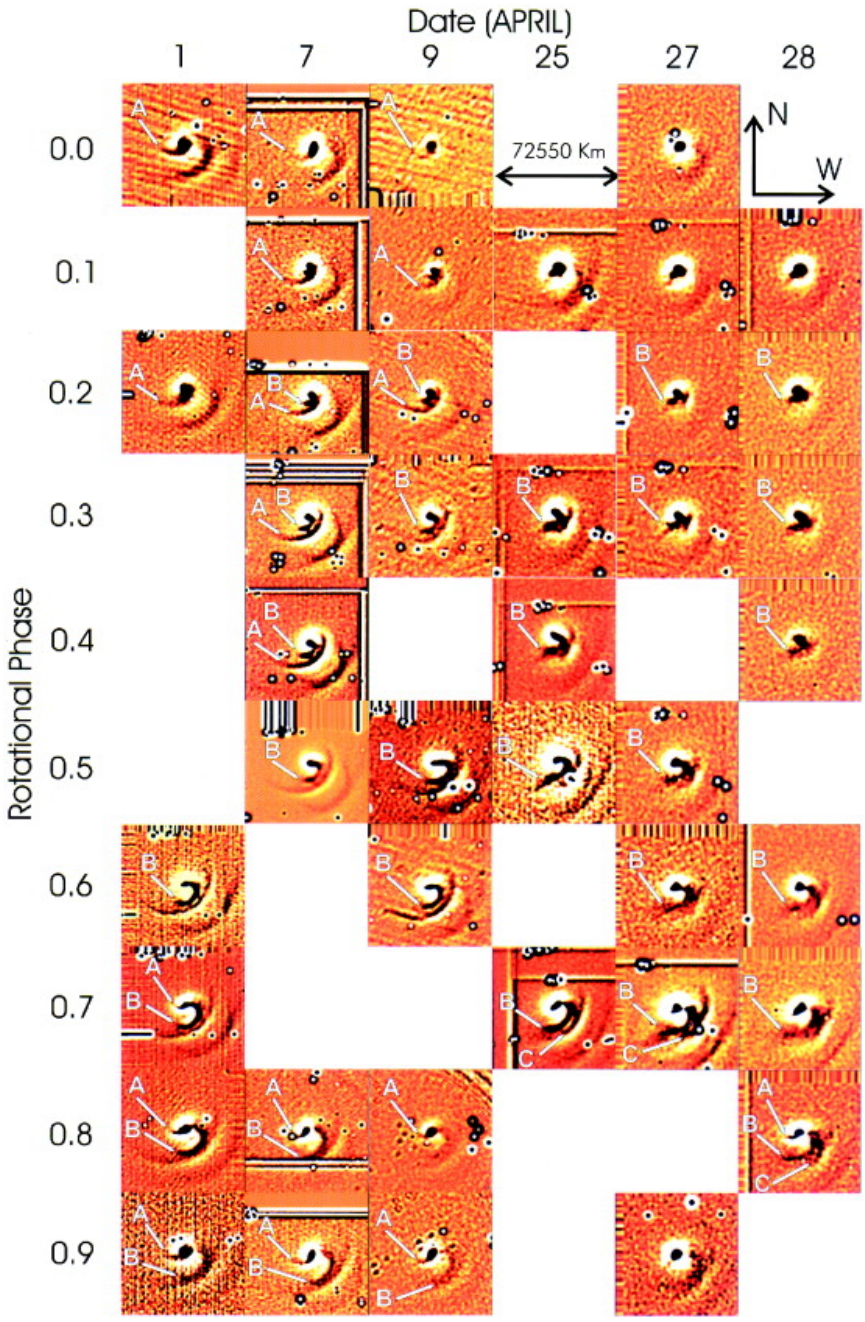

Figure 2.6: Processed images of the central coma of Comet Hale-Bopp, from which the estimated rotational period of 11.35 hr is derived. See Licandro et al. (1998) for details.

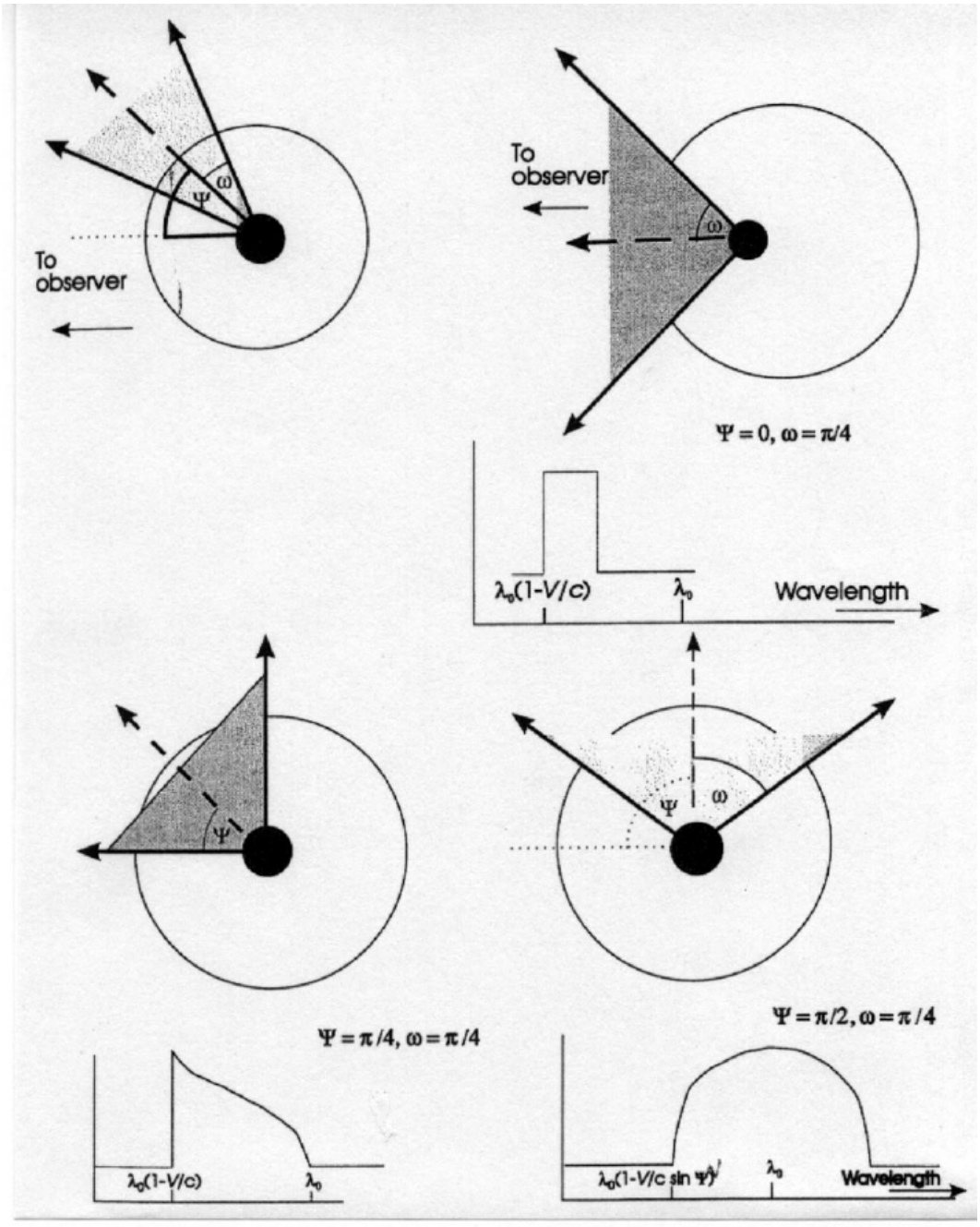

Figure 2.7: Spectral emission line profiles for a cone-shaped cometary jet source. From Emerson (1996).

line intensities in Chapter 4, we use a number of simplifying assumptions. First, we assume the various molecular transitions are optically thin throughout our observing period. Very strong emitters such as HCN have the greatest chance of becoming optically thick, but the observed ratio between the three hyperfine components is close to the line strength ratio, 5:3:1 for the F=2-1, 1-1, 0-1 components of the ground state J=1-0 transition. These ratios are also stable over time, and the modest optical depth derived for the HCN J=4-3 line (Irvine et al. 1998b) suggests that $\tau < 0.1$ for the J=1-0 transition. Monte Carlo radiative transfer calculations of the emission from comet Hale-Bopp, described in greater detail in Chapter 4, predict optically thin conditions for all of the species and transitions detected at OVRO. We also invoke the local thermal equilibrium (LTE) approximation, which is certainly valid in the inner coma (within 10,000 km of the nucleus).

Finally, a Haser model is used, that is we assume a spherically symmetric, radial outflow at a constant velocity. While the interferometry data reveal departures from the Haser model, the limited coverage of the (u, v) plane tends to exaggerate the actual deviations from spherical symmetry. By using the Haser model as a first approximation and by combining it with the Monte Carlo radiative transfer calculations, we can quantitatively compare the interferometric results with those from single dishes. For clearly anisotropic outgassing, revealed either by the images themselves or in spectral data cubes, the estimated production rates must be corrected for the jet solid angle filling factors as estimated by the observed velocity widths. Possible extended dust sources and photolysis on large spatial scales to which the interferometer is insensitive must also be considered.

Radiative Transfer Models of Circumstellar Disks

The millimeter-wave radiative transfer situation for circumstellar disks is very different from that in comets. While the resolving out of emission is a serious concern for cometary studies, disks are sufficiently compact that the vast majority of the line flux is easily recovered by an array. For comets like Hale-Bopp with high production rates, thermal excitation is ensured and for all volatiles save water optically thin emission is the norm. Once the sampling bias of the Haser flow and the nature of the anisotropic outgassing from jets are understood, estimates of molecular column densities and abundance ratios become straightforward.

The observed line intensities in circumstellar disks, however, are a complex function of the physical structure of the disk and of the line/continuum optical depth. The complex

geometry within the disk demands that flexible and efficient radiative transfer techniques be utilized, and of the many techniques available the Monte Carlo approach has shown great promise (Choi et al. 1995). Since Monte Carlo techniques utilize integration paths chosen at random, any number of coordinate systems can be used. The high optical depth of many transitions in circumstellar disks generates very short photon mean free paths, however, and so unless aggressive acceleration schemes are employed, the Monte Carlo approach can be very slow. Computational instabilities and poor convergence can result, but efficient one-dimensional (1D) and two-dimensional (2D) Monte Carlo treatments of the line radiative transfer based on the two-layer passive disk models outlined above have now begun to appear (Hogerheijde & van der Tak 2000; van Zadelhoff et al. 2000). In all such approaches, the intensity of each line is calculated by solving the radiative transfer equation:

$$\frac{dI_\nu}{ds} = \alpha_\nu \left(\frac{j_v}{\alpha_v} - I_\nu \right) \quad ,$$

where I_ν is the intensity, s the path length along a ray normal to the disk, j_ν the emission function, and α_ν the absorption function, or inverse of the mean free path.

2D approaches are necessary to quantitatively treat inclined disks, but a great deal can be learned about the radiative transfer in disks from simpler 1D models that are appropriate for face-on geometries. Here we briefly summarize the results of van Zadelhoff et al. (2000), who utilize an interactive ray-tracing statistical equilibrium (SE) method to calculate the emergent line intensity from circumstellar disks. In SE approaches, the molecular level populations are not assumed to be in LTE, but are calculated using a detailed balance approach in which the radiation field and the role of collisions are considered. These calculations identify regions of the disk where common molecular line tracers are likely to become optically thick, and so provide a useful measure of the volume of the emitting region that we will use in Chapter 3.

Figure 2.8 presents the upper right quadrant of the disk model of D'Alessio et al. (1999). Specifically, the top panel depicts the density profiles predicted, while the bottom panel presents the temperature profiles. Overlaid on these contours are plots of the $\tau = 1$ surfaces for a number of low-J transitions from CO, HCO^+, and their ^{13}C isotopomers at abundances similar to those derived for dark clouds.

As can be seen, the ^{12}CO lines become optically thick in the upper, warm layer of the

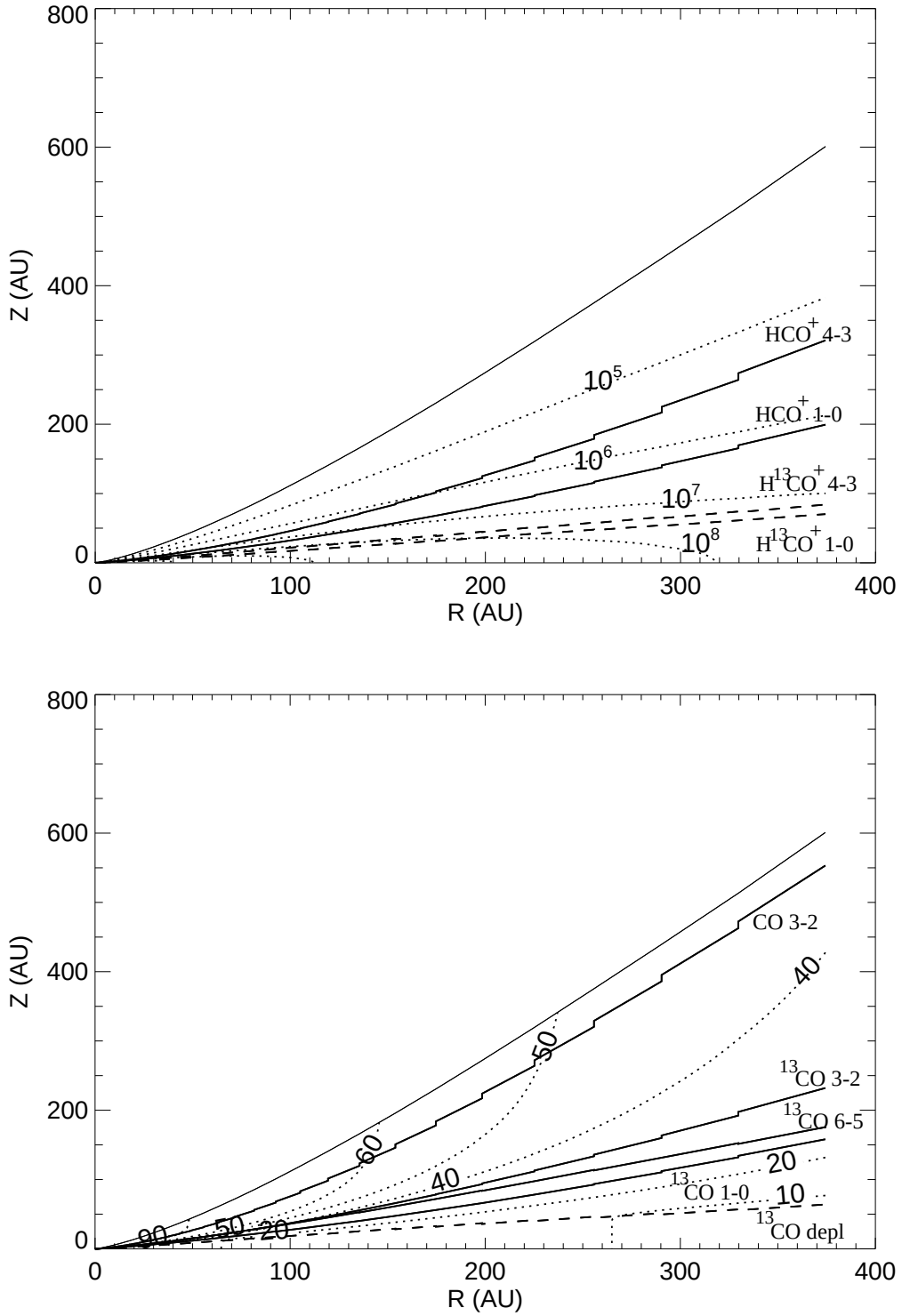

Figure 2.8: The τ=1 surfaces for CO and HCO^+ transitions, along with those from their ^{13}C isotopomers, overplotted on the density (top) and temperature (bottom) distribution in the disk model by D'Alessio et al. (1999). The dotted contours are iso-temperature or iso-density contour lines. See van Zadelhoff et al. (2000) for details.

disk where $T > 40$ K. While the ^{13}CO lines are also optically thick, the $\tau = 1$ surface lies deeper within the colder region of the disk. Thus, the ^{12}CO excitation temperature should be higher than that of ^{13}CO, which must be taken into account in the analysis of isotopomeric line ratios. The higher frequency CO 3–2 and 6–5 lines have larger optical depths than does the 1–0 line, and thus probe better the warm upper layer. At the standard abundances, C^{18}O is only marginally optically thick, with $\tau \approx 1 - 2$. The 1D calculations indicate that for the 1$\rightarrow$0 transition of C^{18}O, 40% of the total disk mass lies outside the C^{18}O $\tau_{(1-0)}$=1 surface for a face-on disk, compared to values of only 0.5% and 3% for the same transition in ^{12}CO and ^{13}CO, respectively. For inclined disks, the path lengths increase and so too should the overall optical depths. Depletion onto grain mantles will lower the overall optical depth, but cannot be constrained without high sensitivity observations of several transitions in each of the important isotopomers. In either case, tracing the disk gas mass with CO observations will clearly be difficult.

For standard HCO$^+$ abundances, the 1$\rightarrow$0 to 4$\rightarrow$3 lines are again optically thick in the outer layers, whereas those of H^{13}CO$^+$ are close to being optically thin throughout the disk. Thus, the HCO$^+$ lines are predicted to probe densities of order $10^5 - 10^6$ cm^{-3}, below the critical density of the 4$\rightarrow$3 transition (so LTE cannot be safely assumed). For H^{13}CO$^+$, the populations will be closer to thermal equilibrium because its emission arises primarily from regions with densities of $10^7 - 10^8$ cm^{-3}. The HCN 1$\rightarrow$0 to 4$\rightarrow$3 lines show a behavior similar to that HCO$^+$. Parent isotopomeric lines are therefore likely to be optically thick for many species in disks, and so whenever possible in Chapter 3 we utilize the emission from isotopically substituted species in deriving relative molecular abundances.

Chapter 3 OVRO Observations of Chemistry in Disks

3.1 Introduction

A thorough understanding of the physical and chemical structure of disks around older T Tauri and Herbig Ae stars is important for constraining models of dust processing, settling, and agglomeration; and for estimating the dispersal timescales for nebular gas and dust, the critical building blocks from which planets are assembled. Indeed, the amount of gas (and dust) available within an accretion disk and the timescale over which it is dissipated play major roles in determining what kind of planetary system, if any, can be formed. Furthermore, an understanding of how various volatile species (water, carbon monoxide, methane, ammonia, nitrogen, etc.) are distributed in the outer regions of circumstellar disks is particularly important to examining the connection between interstellar and nebular processes in the formation of icy planetesimals such as comets and Kuiper Belt Objects.

To date, most of the imaging of classical T Tauri and Herbig Ae stars outlined above has been carried out in various isotopomers of CO for reasons of sensitivity. For three T Tauri stars, namely DM Tau, GG Tau (Dutrey et al. 1997) and TW Hya (Kastner et al. 1997), single dish surveys have been carried out in which a number of species (HCN, CN, HNC, H_2CO, HCO^+, CS, ...) are detected whose emission intensity is similar to that of ^{13}CO or $C^{18}O$. These important first data suggest that, at least in appropriate disks, chemical studies regarding the nature and variation of the disk composition with radius can now be profitably pursued. They further reveal that both ion-molecule chemistry and photon-dominated chemistry must contribute to the observed abundances at large disk radii, since the ratios of species such as CN/HCN and HNC/HCN are too high to be accounted for by quiescent chemical models alone (Spaans 1996; Dutrey et al. 1997; Kastner et al. 1997). At abundances appropriate for YSO envelopes, the optical depths of transitions from species such as HCN and HCO^+ are sufficiently large that their emission should be comparable to that of ^{12}CO if the gas is well mixed and uniform (Hogerheijde & van der Tak 2000). The

fact that they are lower implies that either their abundances are depleted, or, as may be more likely, that the sizes of the emitting regions are strongly species dependent (Dutrey et al. 1997).

The observed emission strengths can be compared with those predicted by current models of the chemistry in the outer regions of circumstellar accretion disks (for recent examples, see Aikawa et al. 1997; Aikawa & Herbst 1999; Finocchi et al. 1997; Finocchi & Gail 1997; Bauer et al. 1997; Willacy et al. 1998; Willacy & Langer 2000). Several models assume that only thermal desorption occurs, while others use cold disk mid-plane temperatures that are inconsistent with recent self-consistent treatments of the radiative transfer in such objects (Chiang & Goldreich 1997; D'Alessio et al. 1997). A number do not include any direct chemical effects of radiation from the young star, and therefore maximize the likelihood of depletion onto grain mantles, resulting in too low abundances compared with observations. The most complete models now include effects such as X-rays, short-lived radionuclide ionization, and photochemistry to examine the radial variations in disk chemistry (Glassgold et al. 1997; Aikawa & Herbst 1999; Willacy et al. 1998;Willacy & Langer 2000), but other important processes, such as dust versus gas settling and size sorting, have not yet been incorporated.

To date, the observations of line emission from molecules other than CO in disks has been carried out in beams much larger than the angular sizes of the disks themselves. Furthermore, a direct comparison to the molecular abundances in models is made difficult by the large potential line optical depths outlined in Chapter 2. A fuller understanding of the details of disk chemistry obviously requires images of several species in each important chemical family (C-, N-, O-, and S-bearing) at the best sensitivity, dynamic range, and spatial resolution (<100 AU preferably) achievable. We have therefore embarked upon a high-resolution interferometric continuum and molecular line survey of isolated protoplanetary disks using the Owens Valley Radio Observatory (OVRO) Millimeter Array. In this chapter, we present our results for two T Tauri stars and two Herbig Ae stars. Section 3.2 describes the sources that have been imaged to date. The details of our aperture synthesis observations are given in Section 3.3, while the line and continuum maps are presented and analyzed in 3.4. Finally, the results are summarized in 3.5.

3.2 Objects Studied

The selected objects, LkCa 15, GM Aur, MWC 480, and HD 163296, have been taken from the recent OVRO surveys of T Tauri and Herbig AeBe stars (Sargent & Koerner 2000; Mannings & Sargent 1997) based on their largish gaseous disk size, excellent fit of pure Keplerian rotational patterns to the observed molecular line images, and strong dust plus CO emission. These features plus their lack of strong outflows make it likely that line emission from the circumstellar disk is dominant. Two are classical T Tauri stars, and two are Ae stars, chosen to investigate the influence of the central stellar luminosity on the chemical composition. A limited set of observations were also acquired for the T Tauri star AA Tau. Table 3.1 presents a summary of the source coordinates, spectral types, distances, luminosities, and ages as judged from recent pre-main sequence stellar evolution models (Siess et al. 2000). The absolute error in such models can be large, but should provide a more robust measure of their relative ages.

Table 3.1: Stellar Properties of OVRO Disk Sources

Star	Spectral Type	d (pc)	R.A.(1950)	Decl.(1950)	T_{eff}(K)	$R_*(R_\odot)$	$L_*(L_\odot)$	$M_*(M_\odot)$	Age(Myr)	V_{ref}
LkCa 15	K5:V	140	04 36 18.4	+22 15 11	4365	1.64	0.72	0.81	11.7	6.0
GM Aurigae	K5V:e	140	04 51 59.0	+30 17 12	4060	1.78	0.8	0.84	1.8	5.6
HD 163296	A0	120	17 53 20.61	-21 56 57.3	9550	2.2	30.2	2.3	6	6.0
MWC 480	A3	130	04 55 35.66	+29 46 07.0	8710	2.1	32.4	2	4.6	5.1

[1]Note.— Units of right ascension are hours, minutes, and seconds, and units of declination are degrees, arcminutes, and arcseconds.

All of the sources have mid- and far-infrared SEDs that are dominated by circumstellar disk emission, and high spatial resolution OVRO observations of GM Aur, MWC 480, and HD 163296 in the CO or ^{13}CO J = 2 $\rightarrow$ 1 transitions have revealed velocity structures consistent with Keplerian velocity fields for the disks. CO J = 2 $\rightarrow$ 1 results collected for LkCa 15 as part of the OVRO T Tauri star disk survey are presented in this Chapter. HD 163296 and MWC 480 are Herbig Ae stars with estimated ages of $\sim$5 Myrs. LkCa 15 and GM Aur are K5 T Tauri stars located at a distance of 140 pc in Taurus, but have very different estimated ages – GM Aur is estimated to be $\sim$2 Myrs old, while the age for LkCa 15 is closer to $\sim$10 Myrs, making it the oldest object in the sample. LkCa 15 is also found to have a very low mass accretion rate from Hα observations (Hartmann et al. 1998), and so may be an example of a waning disk.

3.3 Observations

All measurements were made between 1997 October and 2000 April using the OVRO Millimeter Array at Big Pine, California. The array consists of six 10.4 meter telescopes with an rms surface precision of 35 microns. The pointing accuracy is about $4''$ (day and night), except for brief excursions at sunrise and sunset. Combinations of five array configurations were used to map the sources, with antenna spacings ranging from 20 to 400 m east-west and from 25 to 440 m north-south. Cryogenically cooled SIS receivers on each telescope produced average single sideband system temperatures of 450, 1300, and 1200 K at the frequencies of the ^{13}CO(1-0), CO(1-0), and CO(2-1) lines, respectively. The receivers were tuned for double sideband (DSB) operation so that both the upper and lower sidebands (USB,LSB) could be used for molecular line studies.

The receiver IF output is sent over fiber optic transmission lines to a pair of 1 GHz bandwidth analog correlators and a 512 lag digital correlator that consists of four separately configurable modules with independent downconverters. Table 3.2 presents the digital correlator setups used for all four sources, including the molecular lines contained within the bands and the velocity resolution employed. Spectral line and continuum measurements are made simultaneously, and can be carried out in both the $\lambda = 3$ and 1.3 mm atmospheric windows with a single local oscillator set up.

Calibration of the visibility phases and amplitudes was achieved with observations of quasars, typically at intervals of 20–30 minutes. The quasar 0528+134 and 0507+179 were used for phase and amplitude calibration of LkCa 15 and MWC 480; 0333+321 and 0507+179 were used for GM Aur; NRAO 530 was used for HD 163296. Measurements of Uranus, Neptune, 3C 273 and 3C 454.3 provided an absolute scale for the calibration of flux densities. All data were phase- and amplitude-calibrated using the software package MMA, developed specifically for OVRO (Scoville et al. 1993). Continuum and spectral line maps were generated and CLEANed using the NRAO AIPS package. Uncertainties in the fluxes and source positions are estimated to be 20% and $0.''5$, respectively.

Table 3.2: Digital Correlator Configurations

Source	Molecular Line	Frequency (MHz)	Bandwidth (MHz)	Resolution (km s^{-1})	Detection
LkCa 15	HCN $1_2 - 0_1$	88631.8470	7.5	0.42	Yes
	$H^{13}CN$ $1_2 - 0_1$	86340.184	7.8	0.22	Marginal
	$H^{13}CN$ $3 - 2$	259011.8211	7.5	0.14	Marginal
	HCO^+ $1 - 0$	89188.523	7.8	0.21	Yes
	$H^{13}CO^+$ $1 - 0$	86754.33	7.8	0.22	Yes
	HNC $1 - 0$	90663.593	7.9	0.21	No
	N_2H^+ $1 - 0$	93173.7	7.9	0.20	Marginal
	^{13}CO $1 - 0$	110201.3541	7.8	0.17	Yes
	$C^{18}O$ $1 - 0$	109782.1734	7.5	0.34	Yes
	CN $1_{23} - 0_{12}$	113490.985	7.8	0.17	Yes
	CN $1_{12} - 0_{12}$	113191.325	7.5	0.34	Yes
	CN $1_{11} - 0_{12}$	113144.19	7.5	0.34	Yes
	CN $1_{12} - 0_{11}$	113170.535	7.5	0.34	Yes
	CN $1_{22} - 0_{11}$	113488.142	31	0.66	Yes
	CN $1_{21} - 0_{11}$	113499.643	31	0.66	Marginal
	CN $2 - 1$	226874.745	7.8	0.08	Yes
	DCN $3 - 2$	217238.63	1.9	0.09	Yes
	SO $5_6 - 4_5$	219949.442	1.9	0.09	No
	SO $5_5 - 4_4$	215220.653	7.5	0.17	No
	SO $6_7 - 5_6$	261843.684	7.5	0.14	Marginal
	SO_2 $3_{13} - 2_{02}$	104029.4183	7.5	0.36	No
	H_2S $2_{20} - 2_{11}$	216710.435	1.9	0.09	No
	CS $2 - 1$	97980.95	7.5	0.38	Yes
	CS $5 - 4$	244935.6435	7.5	0.31	Yes
	$C^{34}S$ $5 - 4$	241016.194	7.5	0.31	Yes
	CH_3OH $5_{14} - 4_{14}$	241767.224	31	0.31	Yes
	CH_3OH $5_{01} - 4_{01}$	241791.431	31	0.31	Yes
	CH_3OH $4_{23} - 3_{13}$	218440.0396	7.5	0.17	Marginal
	CH_3OH $11_{14} - 10_{24}$	104300.46	7.5	0.36	No
	OCS $8 - 7$	97301.2085	7.5	0.39	Marginal
	HDO $2_{11} - 2_{12}$	241561.55	7.5	0.31	Marginal
	HDO $3_{12} - 2_{21}$	225896.72	7.8	0.08	Marginal
	HC_3N $24 - 23$	218324.788	7.5	0.17	Yes
	CCH $3_{44} - 2_{33}$	262004.2266	7.8	0.14	Marginal
	CCH $3_{32} - 2_{21}$	262067.3312	7.8	0.14	Marginal
GM Aur	HCN $1_2 - 0_1$	88631.8470	7.8	0.21	Marginal
	$H^{13}CN$ $1_2 - 0_1$	86340.184	7.8	0.22	Marginal
	HCO^+ $1 - 0$	89188.523	7.8	0.21	Yes
	^{13}CO $1 - 0$	110201.3541	7.8	0.17	Yes
	CN $1_{23} - 0_{12}$	113490.985	7.8	0.17	No
MWC 480	HCN $1_2 - 0_1$	88631.8470	7.5	0.42	Yes
	$H^{13}CN$ $1_2 - 0_1$	86340.184	7.5	0.43	Marginal
	HCO^+ $1 - 0$	89188.523	7.5	0.42	Yes
	^{13}CO $1 - 0$	110201.3541	7.8	0.17	Yes
	CN $1_{23} - 0_{12}$	113490.985	7.8	0.17	Yes
	HNC $1 - 0$	90663.593	7.9	0.21	No
	N_2H^+ $1 - 0$	93173.7	7.9	0.21	No
	SO $2_2 - 1_1$	86093.95	7.5	0.44	Marginal
HD 163296	HCN $1_2 - 0_1$	88631.8470	7.8	0.21	No
	HCO^+ $1 - 0$	89188.523	7.8	0.21	Yes
	$H^{13}CN$ $1_2 - 0_1$	86340.1840	7.8	0.22	No
	^{13}CO $1 - 0$	110201.3541	7.8	0.17	Yes
	CN $1_{23} - 0_{12}$	113490.985	7.8	0.17	Yes
	HNC $1 - 0$	90663.593	7.9	0.21	No
	N_2H^+ $1 - 0$	93173.7	7.9	0.21	No

3.4 Results and Analysis

3.4.1 Continuum Emission

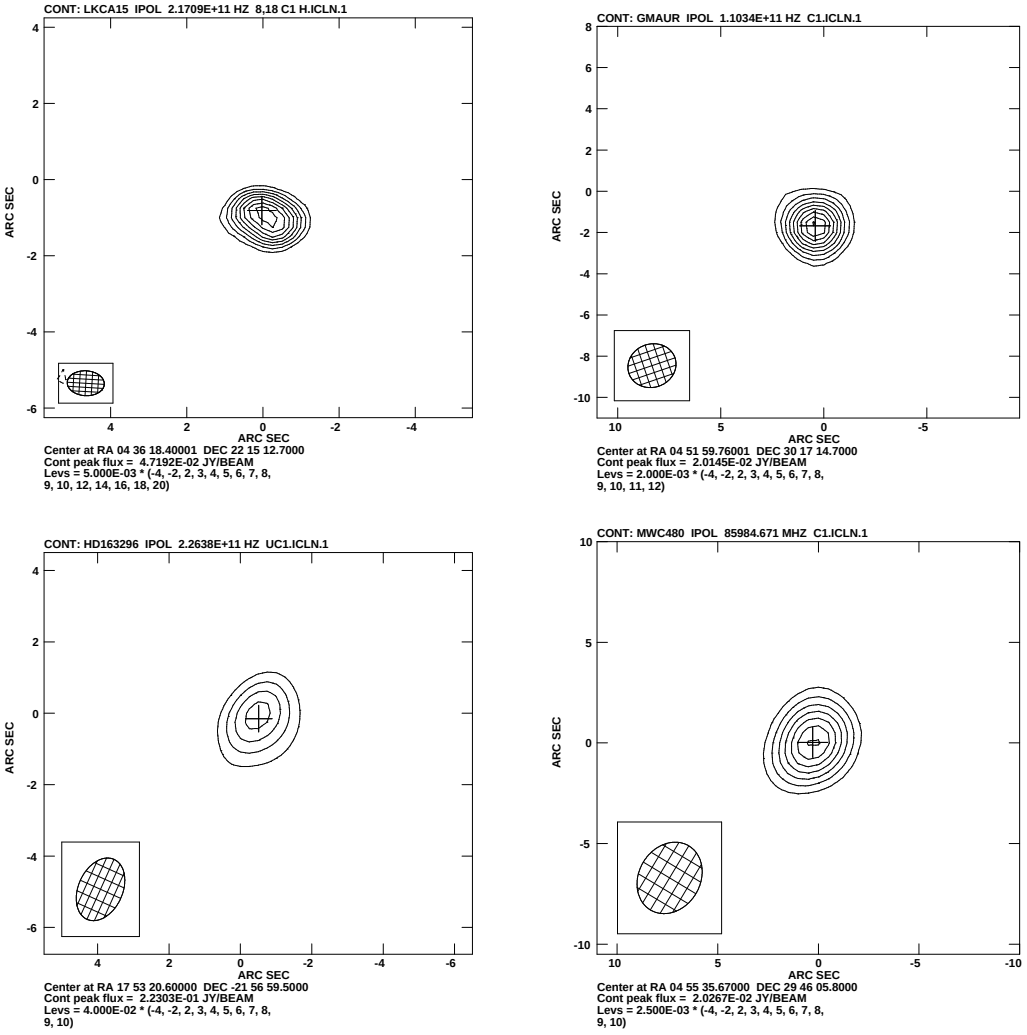

Figure 3.1: Contour plots of continuum emission from LkCa 15, MWC 480, HD 163296 and GM Aur. The centers of the maps correspond to the phase centers of the fields during the measurements with the OVRO Millimeter Array.

Continuum emission is detected from all four systems. The contour maps are shown in Figure 3.1, and the flux densities are listed in Table 3.3. Only the continuum source of LkCa15 is spatially resolved, and even here only in the highest resolution images from 220-260 GHz. Upper limits to the radii of other sources are set by the half-width-half-maximum (HWHM) of the minor axes of the Gaussian-synthesized beams, and have been converted

to a linear scale assuming the source distances listed in Table 3.4.

Table 3.3: OVRO Disk Continuum Observations

Source	Frequency (GHz)	Peak (mJy/beam)	F_ν(mJy)	R_{FWHM}
LkCa 15	86.47	8.01 ± 0.95	10.65 ± 2.00	4.47
	88.98	7.24 ± 0.56	8.06 ± 1.05	3.76
	90.42	9.02 ± 0.37	9.15 ± 0.65	3.85
	97.53	11.30 ± 0.42	11.77 ± 0.74	4.36
	104.26	16.05 ± 0.77	18.59 ± 1.47	4.38
	109.98	16.84 ± 0.69	20.42 ± 1.37	4.43
	110.3	17.90 ± 0.84	20.40 ± 1.58	2.98
	215.27	82.96 ± 3.75	128.94 ± 8.81	1.38
	217.09	75.42 ± 3.34	98.11 ± 6.91	2.87
	223.38	63.83 ± 2.12	93.88 ± 4.80	1.52
	241.47	71.60 ± 2.55	132.47 ± 6.81	1.23
MWC 480	85.98	20.40 ± 0.64	22.0 ± 1.16	3.71
	90.42	21.42 ± 0.61	23.13 ± 1.12	4.33
	110.3	41.59 ± 0.79	45.24 ± 1.43	4.25
HD 163296	85.98	35.47 ± 0.95	40.19 ± 1.79	5.42
	90.42	46.52 ± 1.03	52.59 ± 1.94	9.68
	113.3	82.58 ± 1.84	95.37 ± 3.50	6.24
	226.38	218.12 ± 17.5	387.12 ± 45.2	1.84
GM Aur	85.98	11.31 ± 0.60	13.13 ± 1.16	3.01
	110.34	20.41 ± 0.80	24.57 ± 1.56	2.36

For LkCa 15, the source size is deconvolved from the beam pattern assuming it is elliptical and gaussian. This procedure yields a major/minor axis of $1.''46 \times 1.''08$ ($\pm 0.''1$, 1σ) at a position angle (PA) of 64 ± 10 degrees, values quite comparable to those derived with IRAM Plateau De Bure Interferometer data: 1.45×1.2 at pa 64 ± 13 degrees (Duvert et al. 2000). The corresponding radii derived for the half-maximum intensity of the continuum source are 210 and 153 AU. Assuming the disk is circular, the measured ellipticity predicts an inclination angle (from the disk being face on) of at least 48°. Larger inclination values are not strongly precluded since the continuum minor axis is only marginally resolved, and could in fact be smaller.

As outlined in Chapter 2, the thermal emission from small particles entrained in the disk becomes optically thin at millimeter wavelengths, and so the OVRO measurements provide an excellent means of estimating the disk gas+dust mass directly, the largest uncertainty being the choice of the mass opacity coefficient κ_ν. We assume a standard grain mass opacity form of $K_\nu = 0.1 \left(\frac{\nu}{10^{12} Hz}\right)^\beta$ cm^{2}g^{-1}, where ν is the observing frequency and β is the opacity

index (Beckwith et al. 1990). Fits for LkCa 15, which has the largest number of continuum flux measurements (see Figure 3.2) produce a β value 0.6. Adopting a gas-to-dust ratio of 100, by mass, for an optically thin source with a radially averaged temperature, T, of 40 K, we obtain a gas+dust mass of $\sim$0.2 $M_{\odot}$.

From the more detailed SED analysis of the infrared and millimeter-wave continuum emission within the hydrostatic radiative equilibrium models developed by Chiang & Goldreich (1997), the LkCa 15 disk mass is estimated to be 0.18 $M_{\odot}$ (Chiang et al. 2001), in agreement with the simple calculation outlined above. Results for the four sources are shown in Figure 3.2 and Figure 3.3.

Interestingly, the amount of dust settling is predicted to be quite different for LkCa 15 and GM Aur from the SED fits. The standard model, which fits the GM Aur SED very well, assumes well mixed gas and dust and predicts an H/h ratio of 4, where H is the height of the disk (dust) photosphere and h is the vertical scale height (Chiang et al. 2001). For LkCa 15, the fitted H/h value is only 1.0, which we interpret to mean that dust in disk surface layers has settled vertically towards the midplane. This was expected from the analysis of Chiang & Goldreich (1997), and reinforces similar conclusions by D'Alessio et al. (1999). The H/h parameter is a rather robust one within the confines of the two layer model, for as H/h decreases from 4 to 1 there is a corresponding decrease in the overall level of infrared excess at $\lambda \leq$100 μm since the disk intercepts less stellar radiation. The H/h value fit for MWC 480 is 1.7, again indicative of marked settling of the dust toward the disk midplane. In later sections we will discuss the possible chemical effects of dust settling in order to examine whether the molecular emission observed can be used to trace this important first step along the road to planets.

Dust settling may also help explain the relative paucity of large disks to which the powerful technique scattered light coronography can be applied. The GM Aur disk, for example, has been imaged with both the WFPC2 and NICMOS cameras aboard HST (Stapelfeldt & The WFPC2 Science Team 1997; Koerner et al. 1998). Reflected light contributes about 8% of the total light from the GM Aur system, and the observed extent (450 AU radius) and orientation (45° major axis PA and 60° inclination) of the nebulosity agrees very well with that derived from ^{13}CO J = 2 $\rightarrow$ 1 observations at OVRO (Koerner & Sargent 1995). Coronagraphic imaging of HD 163296 with STIS (Grady et al. 1999; Devine et al. 1999) reveals a 450 AU circumstellar disk, with a disk semi-major axis of 140° $\pm$ 5° and an inclination

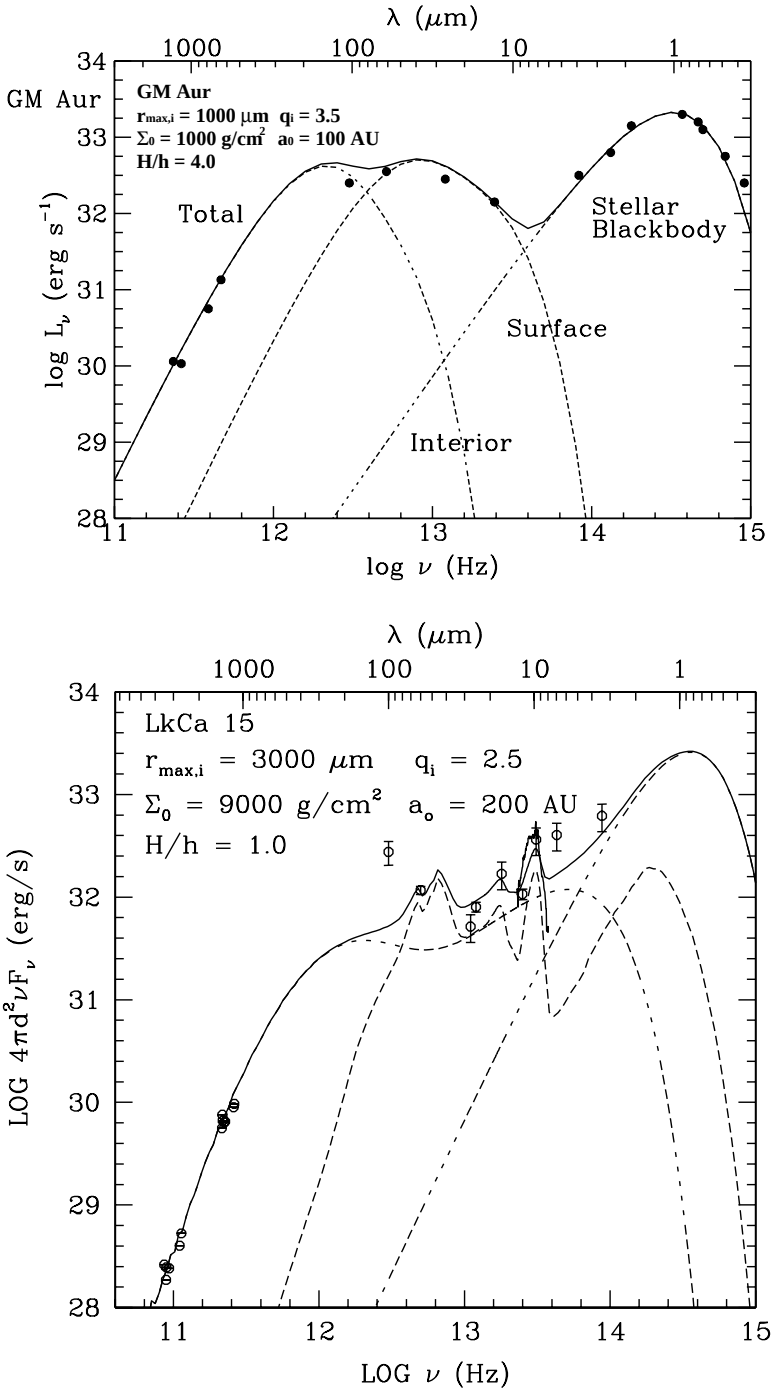

Figure 3.2: SED fits for GM Aur (adapted from Chiang et al. 1997) and LkCa 15 (from Chiang et al. 2001).

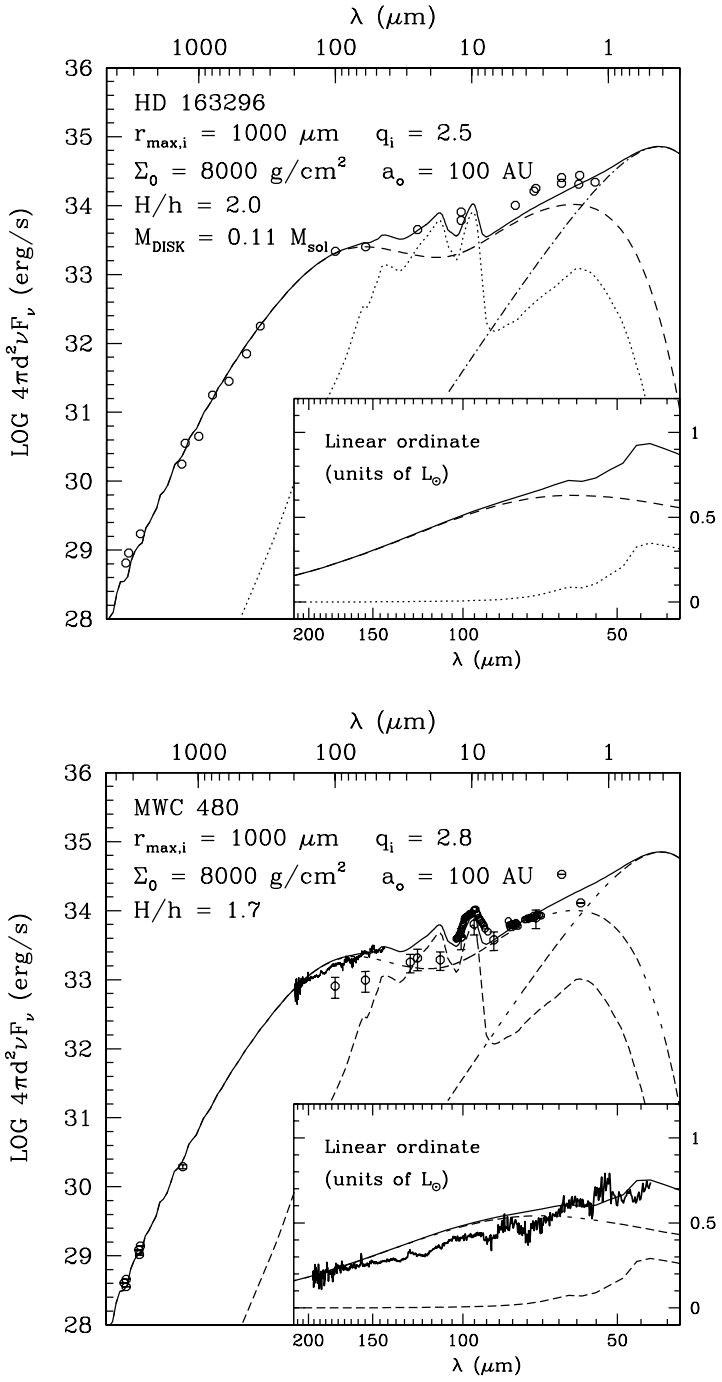

Figure 3.3: SED fits for HD 163296 and MWC 480 (from Chiang et al. 2001).

of 60° ± 5°, both values in reasonable agreement with those derived from millimeter-wave imaging in CO (Mannings & Sargent 1997). The analysis of a broadband reflected light image suggests the HD 163296 disk contains an annulus of depleted material at 325 AU and a partially cleared zone extending inward from ~300 AU to 120-180 AU. A chain of Herbig-Haro knots is weakly observed perpendicular to the disk extension.

Studies of nine additional T Tauri and Herbig Ae stars have been carried out with HST by Padgett et al. (1999a). Despite the known presence of large disks and careful subtraction of the stellar point spread function, no circumstellar reflection nebulosities were detected. They proposed possible reasons for the non-detections including an observational bias toward face-on disks among known T Tauri stars and strongly forward scattering dust grains within the disks, but dust settling such as that inferred for LkCa 15 and MWC 480 (for which no optical or near-infrared disk images exist) would also make scattered light difficult to detect. HST WFPC2 GTO Observation (Krist et al. 1997) of LkCa 15 lack any detectable reflection nebulosity, which is consistent with the different dust setting situation between GM Aur and LkCa 15.

3.4.2 Keplerian Rotation of the Disk

Except for LkCa 15, the high spatial and spectral resolution observations of CO and/or its isotopomers in the J = 2 → 1 transition have been presented in the peer-reviewed literature (Koerner & Sargent 1995; Mannings & Sargent 1997; Mannings et al. 1997). In all cases, the molecular gas emission is found to be more extended than that of the dust, as is shown for LkCa 15 in Figure 3.4a (as compared to the dust emission presented in Figure 3.1). Dust no doubt extends to similar radii, but the sensitivity of current interferometric arrays is such that the weak dust emission at distances greater than ~100 AU cannot be detected (Duvert et al. 2000). Likewise, the molecular emission from the innermost region of the disk (<30-50 AU) is sufficiently beam diluted even at 1-2″ resolution that no direct information on this size scale can be obtained without further improvements in sensitivity and imaging performance. The circumstellar gas emission does robustly trace the line-of-sight velocity component of the outer disk via Doppler shifts measured at high angular resolution, as is shown in the intensity-weighted mean gas velocity map shown in Figure 3.4. Molecular gas southwest of the star is seen to be blue-shifted (that is, to be approaching the observer), whereas that to the northeast is red-shifted, or receding, consistent with orbiting gas in

a disk inclined with respect to the plane of the sky. The presence of a rotating disk and constraints to important disks parameters such as size and inclination can be shown more clearly by analyzing the velocity-dependent morphology and intensity of the gas emission.

Figure 3.5a-k displays the circumstellar emission patterns in velocity intervals of width 0.65 km s^{-1}. For comparison, synthetic spectral line maps, generated by a model of a disk in Keplerian rotation, are shown in adjacent panels. The model disk (Koerner & Sargent 1995; Mannings et al. 1997) uses a two-component gaussian emissivity distribution with half-maximum radii taken from the fit to the integrated map in Figure 3.4b. The inclination angle i, outer cut-off radius R_D, and relative amplitudes of the gaussian emissivity components were varied to match the structure in Figure 3.5. Acceptable fits are found with the stellar mass of $m_{star} = 0.7 \pm 0.1\ M_\odot$. The corresponding inclinations are $i_{disk} = 58° \pm 10°$, while the peak amplitude ratios of the inner and outer gaussian emissivity components are 5:1. The estimated stellar size and inclination are in good agreement with optical and infrared photometry (Bouvier et al. 1995), and with those derived from recent millimeter-wave aperture synthesis imaging with the Plateau de Bure interferometer (Simon et al. 2001). As can be seen, the resulting synthetic maps of a disk in Keplerian rotation agree very well with the CO J=2 $\rightarrow$ 1 spectral line maps of LkCa 15. Similar fits to the other sources yield the disk parameters presented in Table 3.4. In the molecular survey that follows, important disk physical properties are fixed at the values derived from the dust (disk mass) and CO (disk size and orientation) emission.

Table 3.4: Disk Properties as Judged by Dust and CO Emission

Source	Inclination (Degree)	Major Axis PA (Degree)	Disk Mass(Continuum) ($M_\odot$)	R_{out}(CO 2-1) (AU)
LkCa 15	58 ± 10	64 ± 10	0.18	435
GM Aur	54 ± 5	57 ± 5	0.025	525
MWC 480	30 ± 5	157 ± 4	0.029	695
HD 163296	58 ± 5	143 ± 20	0.028	310

3.4.3 $^{13}CO/HCO^+$, CN/HCN

Given the likely interplay of ion-molecule and photon dominated chemistry alluded to in the Introduction, a survey of all four sources using ^{13}CO/CN (LSB/USB) and H^{13}CN/HCN, HCO^+ (LSB/USB) local oscillator settings was carried out first. ^{13}CO provides the opac-

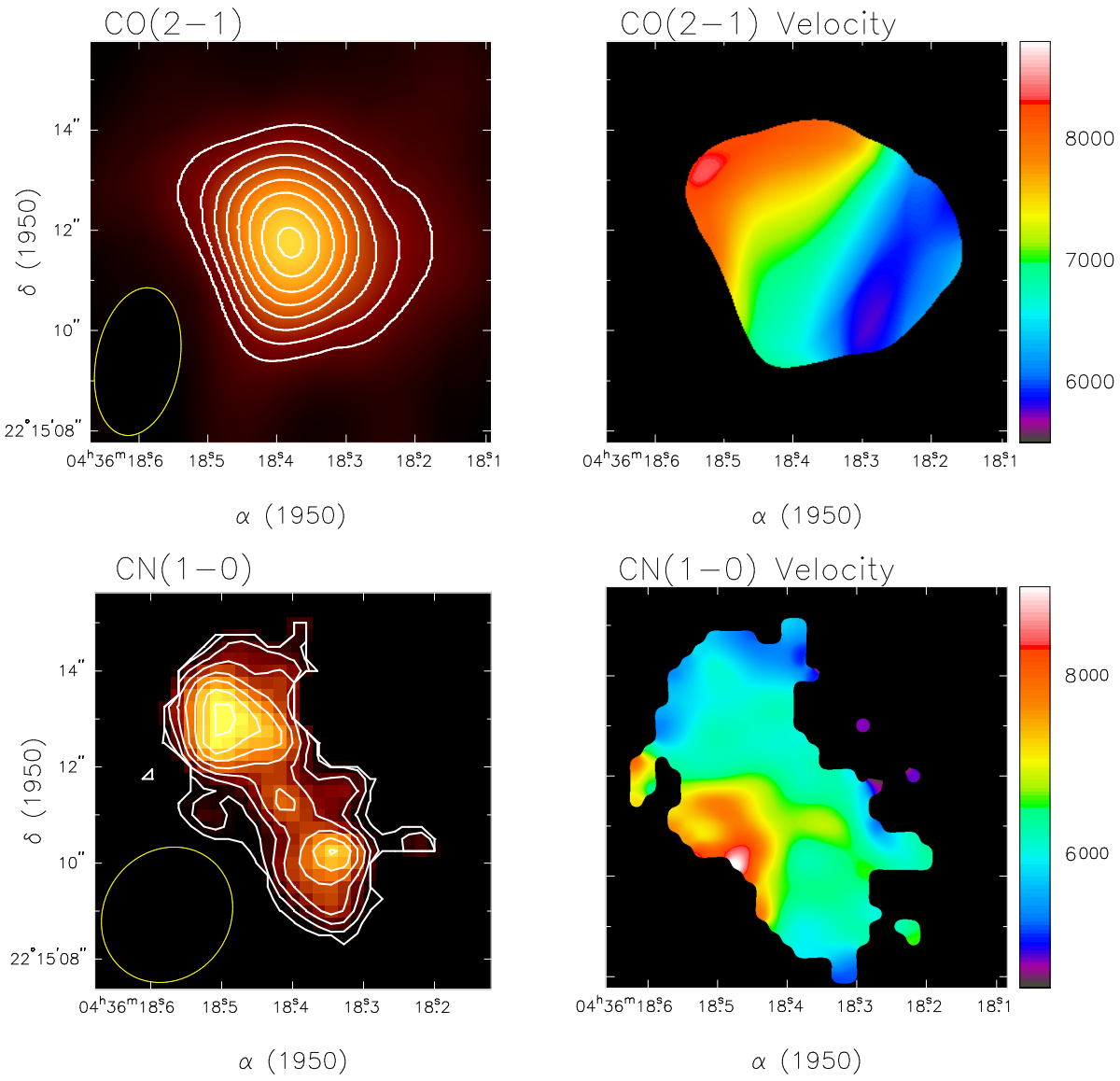

Figure 3.4: CO 2 → 1 and CN 1 → 0 emission toward LkCa 15. The integrated intensity maps for CO 2 → 1 and CN 1 → 0 are shown at left. The velocity fields (first moment maps) over the observed emission region are shown at right.

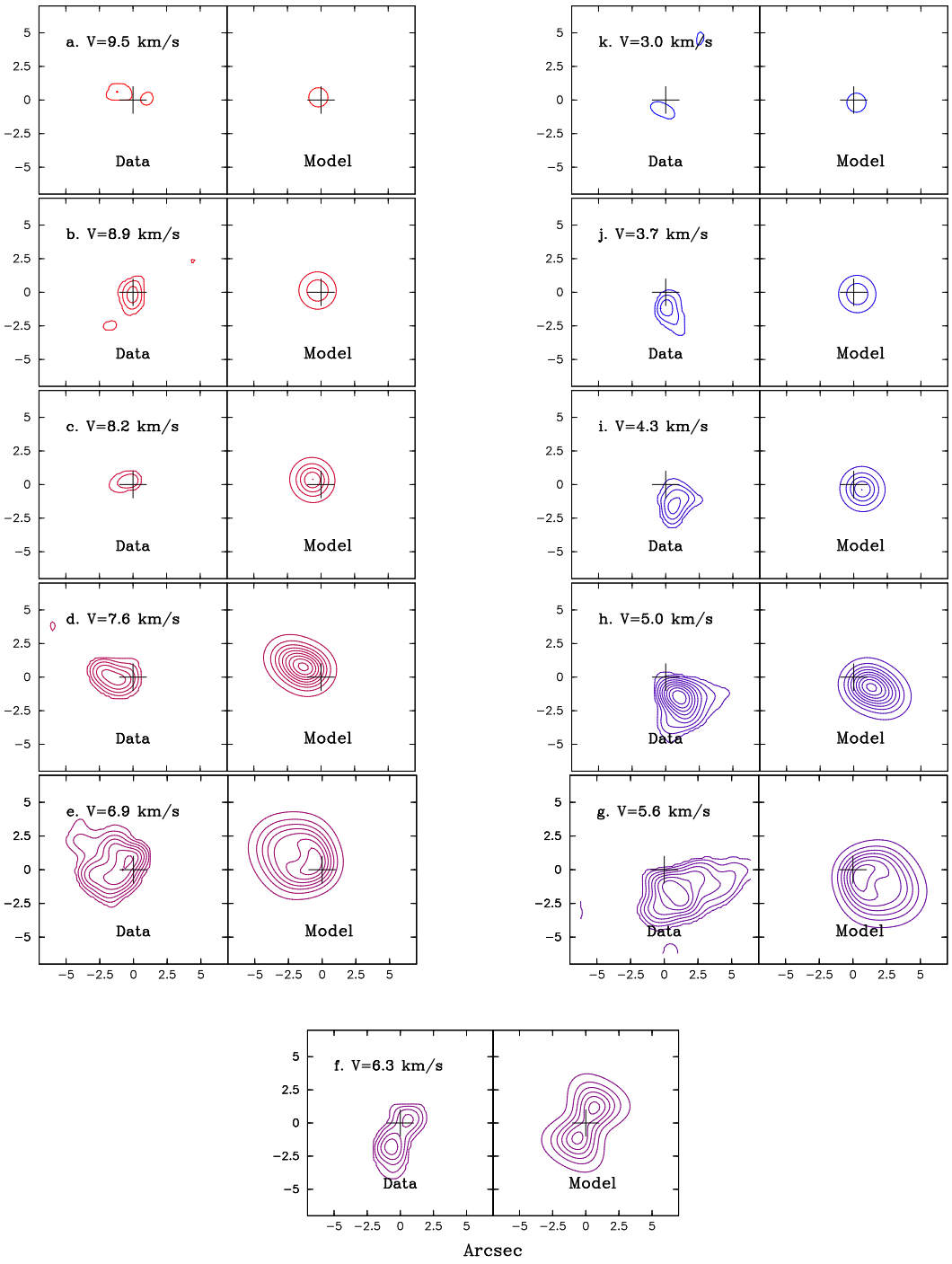

Figure 3.5: CO 2 → 1 from the disk around LkCa 15. The steps are 0.65 km s^{-1} in size, and run over the full range of emission observed. Panels at right depict the results of the best fit disk model discussed in the text.

ity check necessary to use carbon monoxide as a tracer of the disk gas mass, and provides an internal measure of the disk velocity field. The HCN/CN (photochemistry) versus $^{13}CO/HCO^+$ (fractional ionization) line ratios form important diagnostics of the physical and chemical processes in circumstellar disks. Results from these local oscillator settings were then used to gauge whether observations in additional molecules and isotopomers were warranted for a given source.

In certain cases, especially for LkCa 15, there are dramatic differences in the morphologies of the integrated emission from various molecules. Figure 3.6 and Figure 3.7 for example, displays the contour map of ^{13}CO, HCO^+, CN and HCN $1 \rightarrow 0$ emission integrated over the full range of disk velocities observed. CN $1 \rightarrow 0$ data were acquired at the same time and with the same (u, v) spacings as those for ^{13}CO $1 \rightarrow 0$, which is also true for the HCN/HCO^+ $1 \rightarrow 0$ data sets. In the integrated intensity maps, the ^{12}CO (Figure 3.4) and ^{13}CO emission peaks are centered on the continuum source position indicated by the cross, while those of CN and HCN (Figure 3.7) are clearly offset. Indeed, the map of CN shows double peaks along the major axis of the disk, revealing enhanced CN abundances some 200-400 AU from star (2-3″ away from the center). The flux densities for ^{13}CO and CN are nearly identical, and so the observed difference in morphology does not arise from differences in the signal-to-noise (S/N) ratios or (u, v)-sampling of the observations.

Figure 3.8 and Figure 3.9 show the relative positions between red-shifted and blue-shifted integrated intensities for various molecules. For $^{13}CO/HCO^+$, the velocity gradient lies along the disk major axis, with red-shifted emission to the NE and blue-shifted emission to the SW, as was found for CO. Even though the velocity gradient of HCN is elongated at the disk major axis PA, the separation between the red-shifted and blue-shifted maps is much larger than for CO/HCO^+. The CN maps show a rather different velocity gradient lying roughly perpendicular to the disk PA, which is obviously inconsistent with Keplerian rotation models. Interestingly, no evidence for outflow wings are evident in any of the spectra, nor have optical or infrared studies to date revealed evidence of outflow from LkCa 15.

Several different transitions of CN have been observed toward LkCa 15. Figure 3.10 shows the CN $1 \rightarrow 0$ emission at low spectral resolution. Three hyperfine lines have been detected. The CN $1_{22} \rightarrow 0_{11}$ and CN $1_{23} \rightarrow 0_{12}$ components are strong enough to compare the difference of the integrated red-shifted and blue-shifted emission. Because the blue-

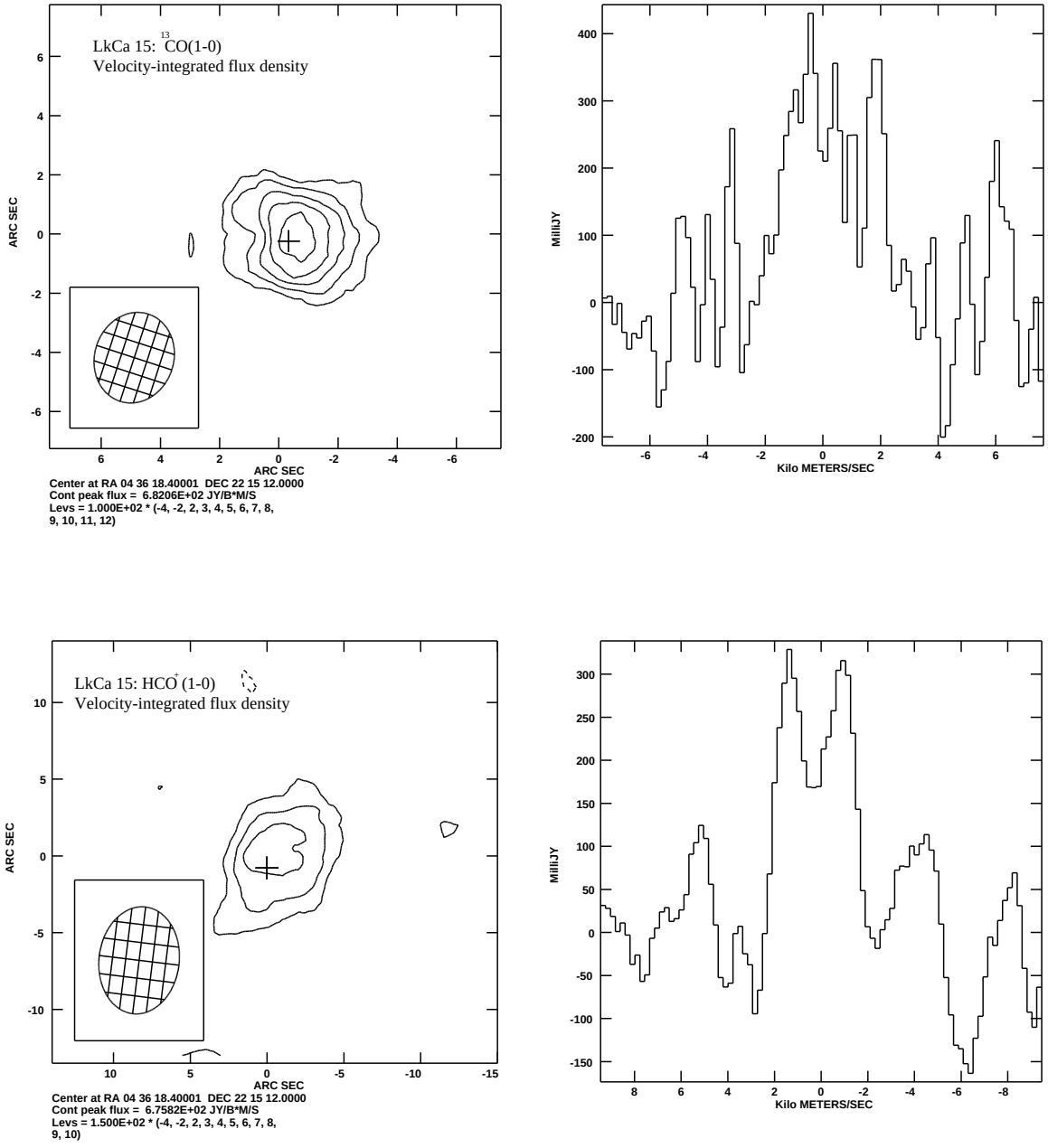

Figure 3.6: OVRO observations of the ^{13}CO and HCO$^+$ $1 \rightarrow 0$ emission from LkCa 15. Integrated intensities are shown at left, spectra averaged over the disk area at right.

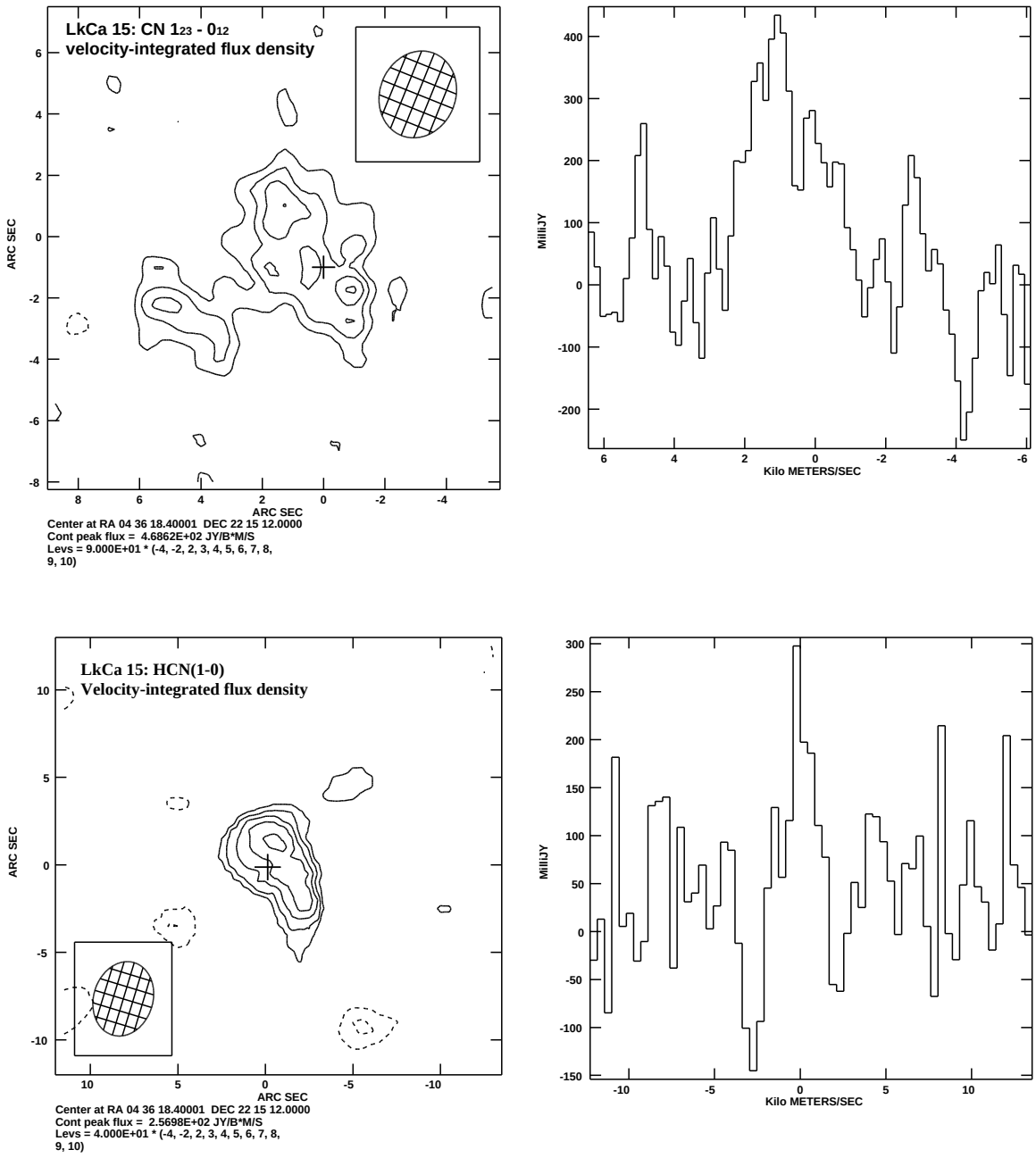

Figure 3.7: OVRO observations of the CN and HCN $1 \rightarrow 0$ emission from LkCa 15. Integrated intensities are shown at left, spectra averaged over the disk area at right.

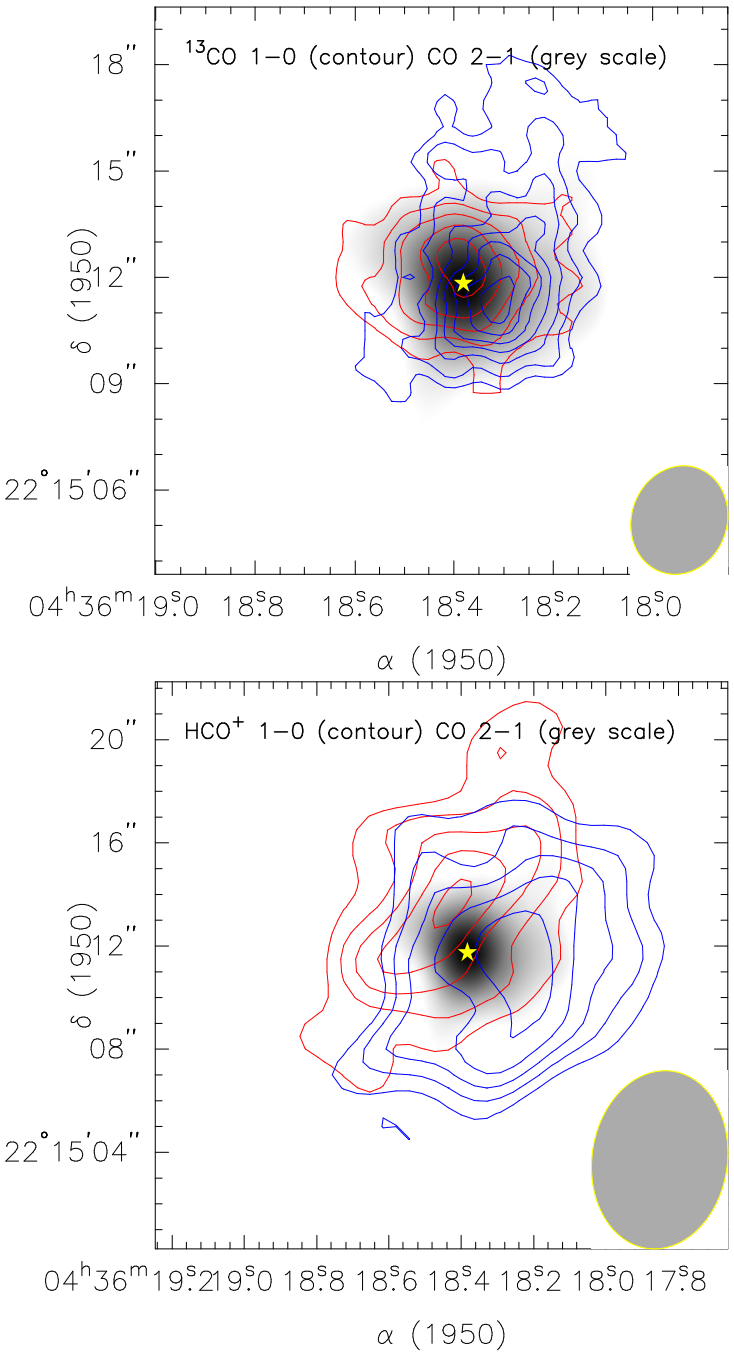

Figure 3.8: OVRO observations of the ^{13}CO and HCO$^+$ $1 \rightarrow 0$ emission from LkCa 15. Intensities are integrated over the blue-shifted and red-shifted line components, respectively (also indicated by color).

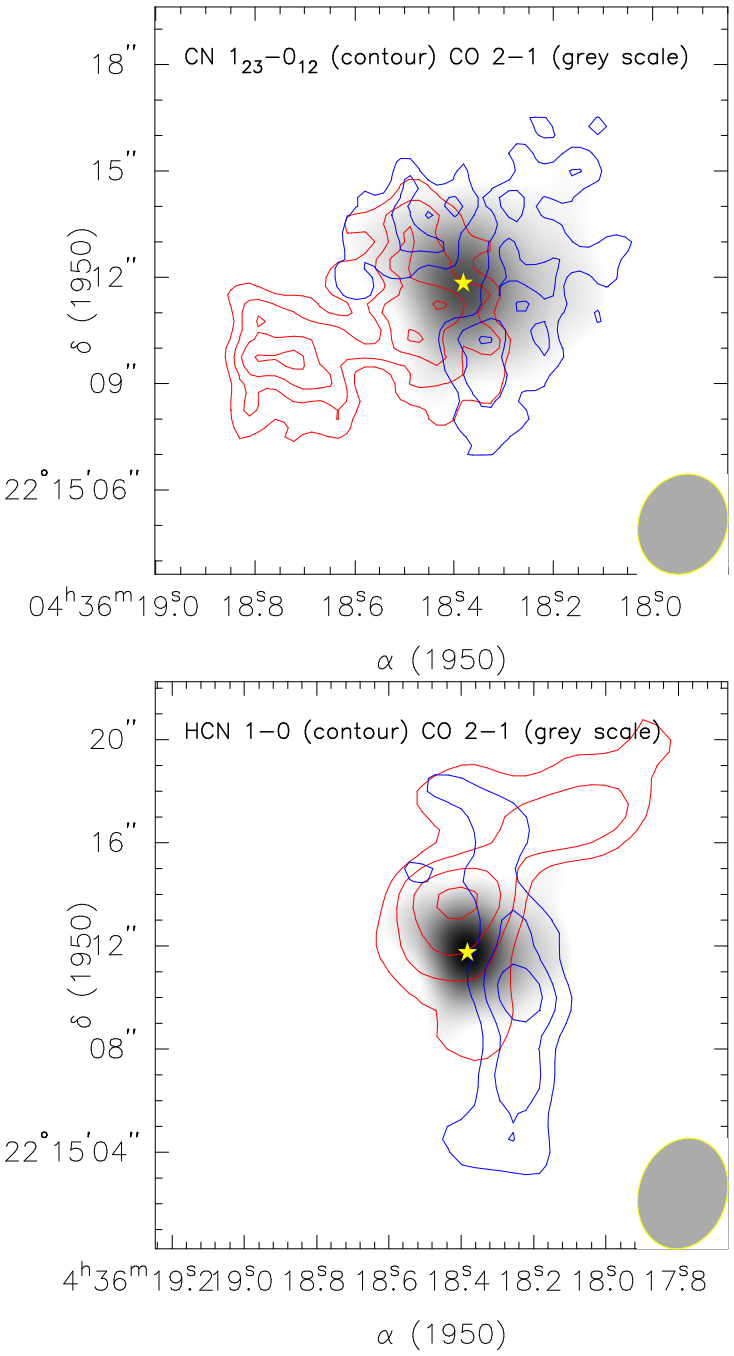

Figure 3.9: OVRO observations of the CN and HCN 1 → 0 emission from LkCa 15. Intensities are integrated over the blue-shifted and red-shifted line components, respectively (also indicated by color).

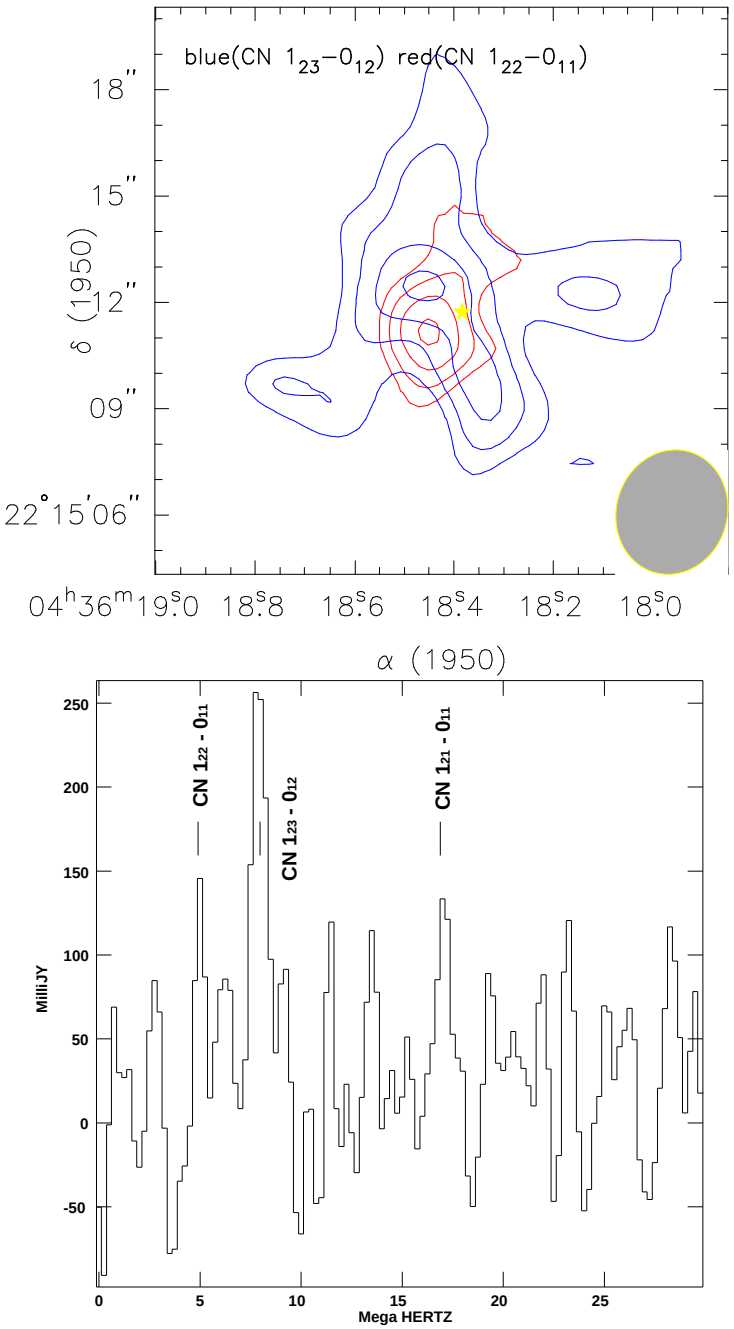

Figure 3.10: OVRO observations of the CN 1 → 0 emission from LkCa 15. Intensities are integrated over the blue-shifted and red-shifted line components, respectively (also indicated by color).

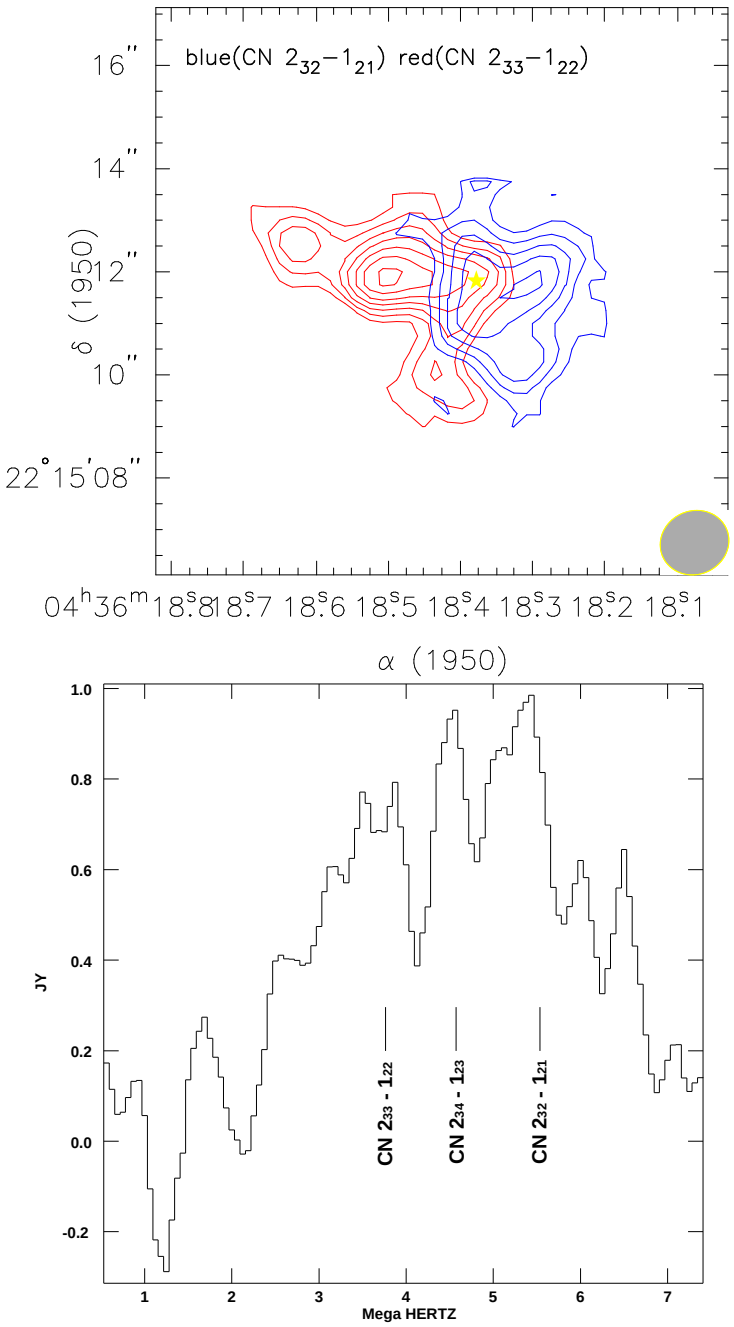

Figure 3.11: OVRO observations of the CN 2 → 1 emission from LkCa 15. Intensities are integrated over the blue-shifted and red-shifted line components, respectively (also indicated by color).

shifted part of CN $1_{22} \rightarrow 0_{11}$ might be confused with the red-shifted part of CN $1_{23} \rightarrow 0_{12}$, we only plot red-shifted velocities for CN $1_{22} \rightarrow 0_{11}$ and blue-shifted velocities for CN $1_{23} \rightarrow 0_{12}$. The relative positions of the red- and blue- shifted emission indicate the same velocity gradient shown previously. 1.3 mm observations of the CN $2 \rightarrow 1$ transition have also been conducted, and the results are shown in Figure 3.11. For the same hyperfine component blending reasons discussed above, we used only the red-shifted velocities for CN $2_{33} \rightarrow 1_{22}$ and the blue-shifted velocities for CN $2_{32} \rightarrow 1_{21}$ to investigate the kinematics. As compared to the CN $1 \rightarrow 0$ emission, the CN $2 \rightarrow 1$ line would be expected to probe warmer and denser regions of the disk. The velocity gradient derived from the CN $2 \rightarrow 1$ data is shown in Figure 3.11.

At first glance, the CN abundance pattern seems counterintuitive. As a product of photochemistry, the production rate of CN would be expected to *decrease* with increasing distance from the central star. CN $1 \rightarrow 0$, which probes the colder and outer regions of the disk, might be more affected by external UV radiation, perhaps leading to velocity gradients more indicative of disk wind driven by photoevaporation (Johnstone 2000). Are similar patterns observed in the other objects? Figure 3.12, Figure 3.13, Figure 3.14, Figure 3.15 and Figure 3.4.3 summarize the HCN/CN and $^{13}CO/HCO^+$ observations of HD 163296, MWC 480, and GM Aur. Table 3.5 provides a quantitative listing of the integrated line intensities for all local oscillator settings used, and tabulates the estimated beam averaged column densities calculated assuming local thermodynamic equilibrium (LTE) and optically thin line emission. No HCN is detected directly toward HD 163296, the most luminous star in our sample (see Table 3.1), but the CN emission is very strong and elongated compared to the ^{13}CO image acquired simultaneously. The HD 163296 velocity maps in Figure 3.17 all show gradients along the disk major axis (PA$\sim$126°). In contrast, GM Aur shows detectable emission from HCN but none from CN. Like LkCa 15, disk around the Herbig Ae star MWC 480 has strong emission from all four molecules. No obvious extensions are seen for either CN or HCN, and the velocity patterns for all species (Figure 3.18) are consistent with the disk Keplerian rotation pattern derived from CO $2 \rightarrow 1$ images (Mannings et al. 1997).

HCO^+, like ^{13}CO, is readily observed toward all of the disks, and provides observational lower bounds to the fractional ionization at large radii. The CN/HCN ratio changes dramatically, however, and the high ratio observed in LkCa 15 reveals that stellar luminosity alone is not the deciding factor. Dust settling may also play a role, but further studies that

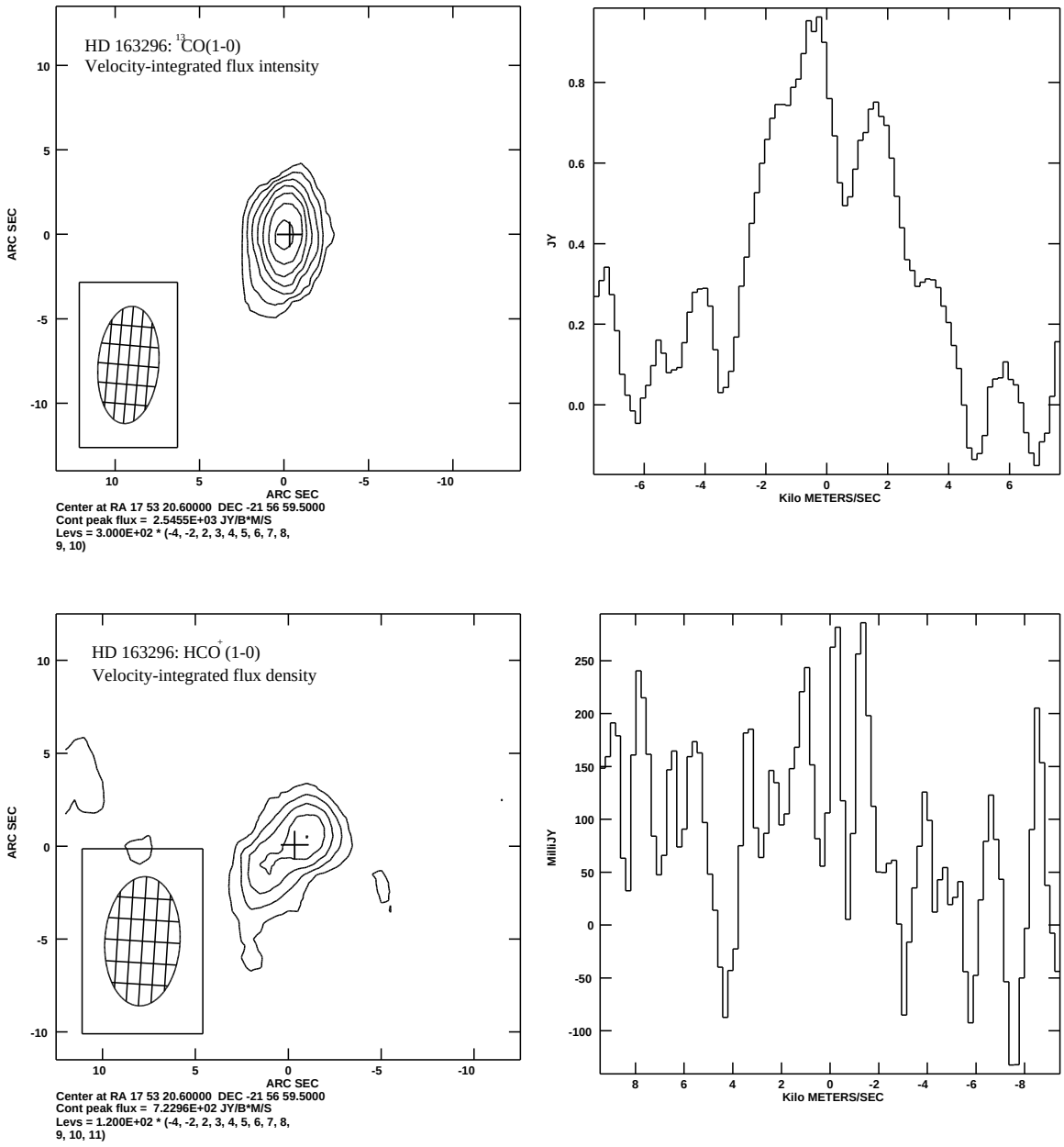

Figure 3.12: OVRO observations of the ^{13}CO and HCO$^+$ $1 \rightarrow 0$ emission from HD 163296. As before, the integrated intensity, or moment zero, maps are shown at left and the spectra averaged over the disk area are shown at right.

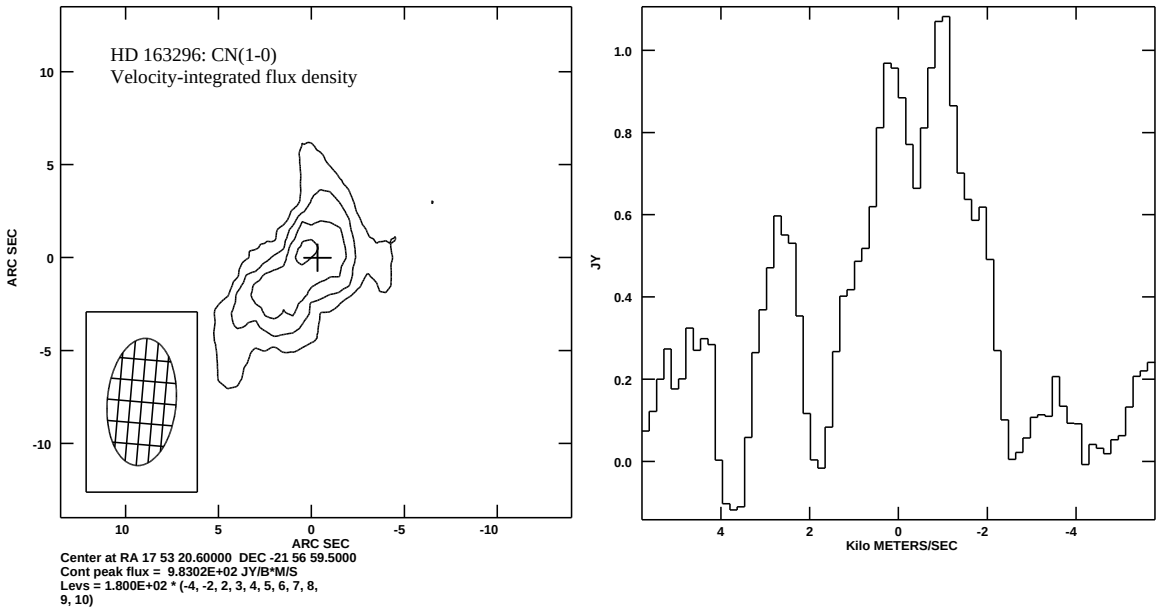

Figure 3.13: OVRO observations of the CN $1 \rightarrow 0$ emission from HD 163296. As before, the integrated intensity, or moment zero, maps are shown at left and the spectra averaged over the disk area are shown at right.

examine a variety of radiation fields and gas/dust ratios are needed to decide which is more important.

3.4.4 Other Species and Isotopomers Toward LkCa 15

It became clear early in the observing program that the molecular emission from the disk around LkCa 15 is particularly rich. A number of other species have therefore been imaged, and the results of the resulting spectral line survey are presented along with the HCN/HCO^+ and 13CO/CN compilation in Table 3.5. As a guide to the quality of these data for less abundant and more complex species such as sulfur-containing molecules and grain mantle products, Figure 3.19 and Figure 3.20 present the $C^{34}S$/CS and CH_3OH emission observed toward LkCa 15. Figure 3.21 even shows red- and blue-shifted HC_3N $24 \rightarrow 23$ emission whose pattern is consistent with the velocity gradient of Keplerian rotation in the disk. To place these observations in context, it is first necessary to examine the radiative transfer conditions under which the molecular emission emerges from the disk and the likely chemical gradients that exist in the outer regions of circumstellar disks, topics we turn to next.

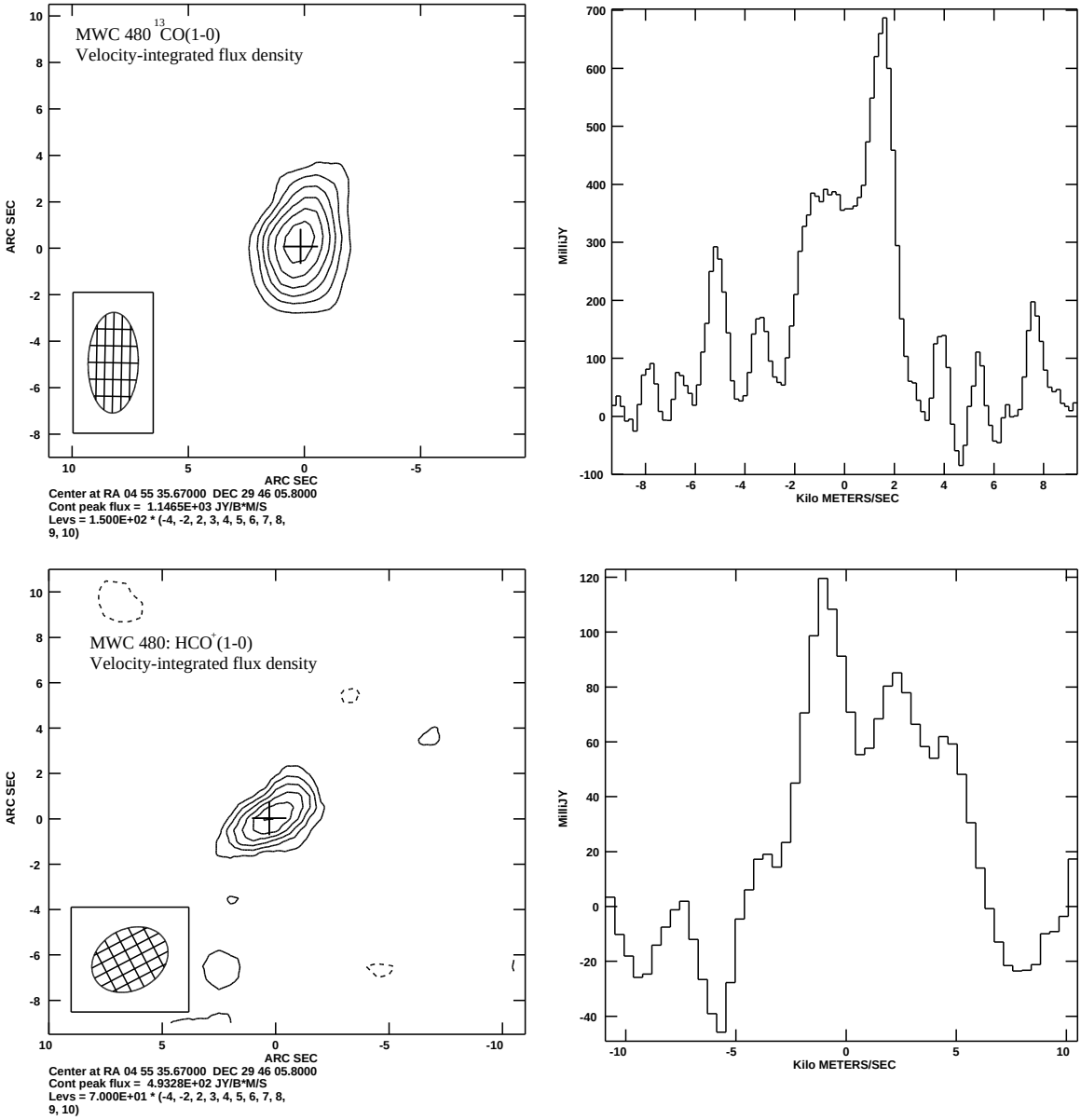

Figure 3.14: OVRO observations of the ^{13}CO and HCO^+ $1 \rightarrow 0$ emission from MWC 480. As before, the integrated intensity, or moment zero, maps are shown at left and the spectra averaged over the disk area are shown at right.

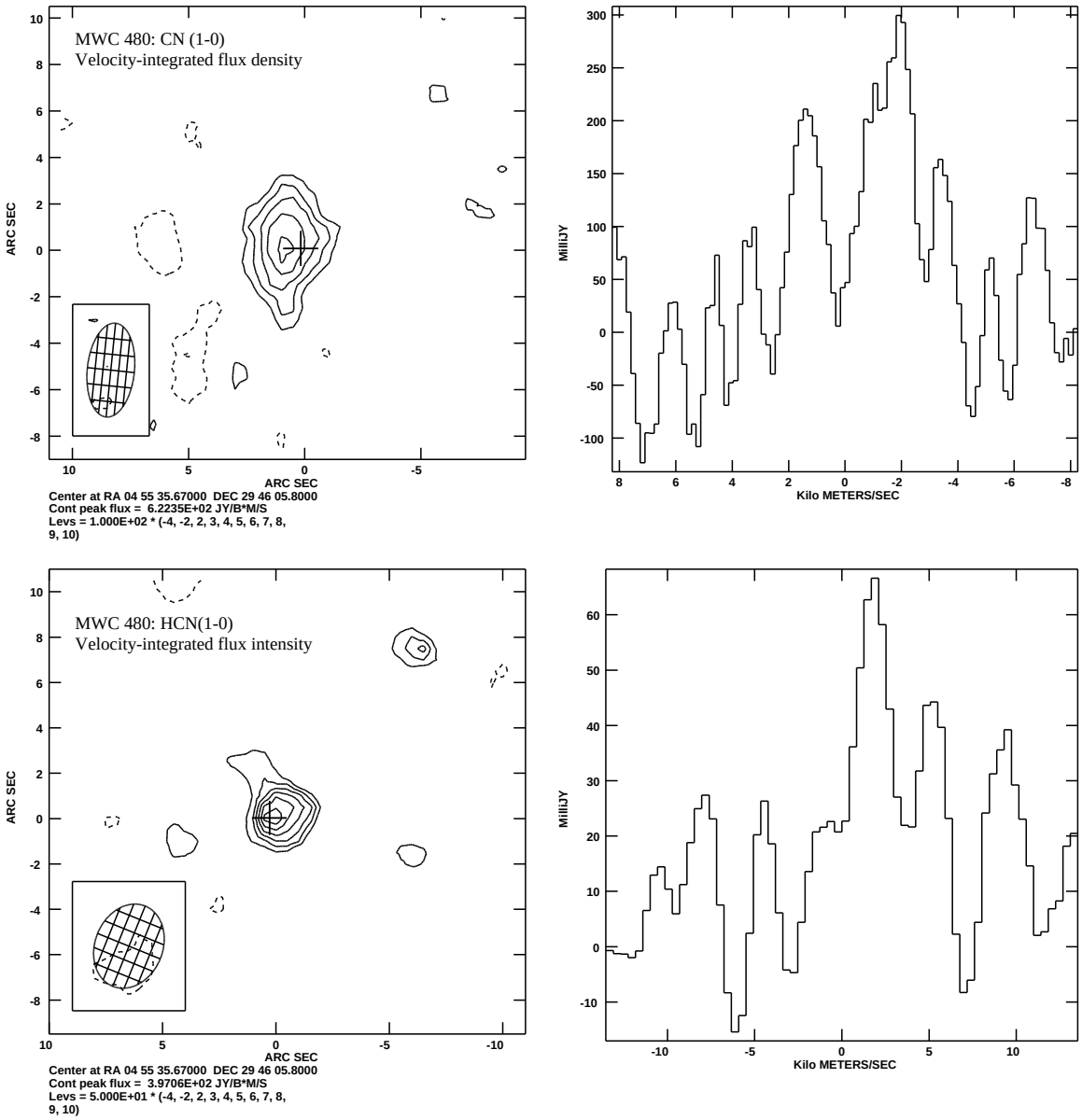

Figure 3.15: OVRO observations of the CN and HCN $1 \rightarrow 0$ emission from MWC 480. As before, the integrated intensity, or moment zero, maps are shown at left and the spectra averaged over the disk area are shown at right.

Table 3.5: Molecular Intensities and Column Densities in the LkCa 15 and GM Aur TTs Disks and the MWC 480 and HD 163296 HAe Disks

Source	Lines	Beam arcsec	Int.Inten (Jy/Beam m/s)	SNR	ΔV (km/s)	Int.Inten. (K km/s)	N(40K) (cm^{-2})
LkCa 15	HCO^+ 1 $\rightarrow$ 0	4.5–3.3	402.061	3.3	8.0	4.19	1.49(13)
	HCN $1_2 \rightarrow 0_1$	4.3–3.4	285.69	3.4	3.8	3.03	2.43(13)
	HNC 1 $\rightarrow$ 0	4.0–2.8	97.47	2.4	3.8	1.30	5.38(12) U
	N_2H^+ 1 $\rightarrow$ 0	3.7–2.7	70.921	2.9	3.4	0.99	5.65(12) U
	CN $1_{23} \rightarrow 0_{12}$ north	2.7–2.4	319.254	3.7	3.5	4.81	1.74(14)
	CN $1_{23} \rightarrow 0_{12}$ south	2.7–2.4	457.071	3.7	4.6	6.88	2.49(14)
	CN $1_{12} \rightarrow 0_{12}$	4.1–3.8	365.707	3.3	6.9	2.24	2.16(14)
	CN $1_{11} \rightarrow 0_{12}$	4.1–3.8	413.591	3.6	6.9	2.49	3.04(14)
	CN $1_{12} \rightarrow 0_{11}$	4.1–3.8	118.289	3.1	5.3	0.73	9.11(13)
	CN $2_3 \rightarrow 1_2$	1.3–1.3	944.48	4.9	5.8	6.51	9.67(13)
	^{13}CO 1 $\rightarrow$ 0	3.1–2.6	611.417	4.0	5.4	7.43	1.63(16)
	$C^{18}O$ 1 $\rightarrow$ 0	4.3–4.0	251.113	3.8	6.8	1.47	3.25(15)
	$H^{13}CN$ $1_2 \rightarrow 0_1$	5.8–4.6	361.142	2.6	6.1	2.25	1.92(13) U
	$H^{13}CN$ 3 $\rightarrow$ 2	0.9–0.6	105.291	3.5	2.0	1.49	3.07(12) U
	HC_3N 24 $\rightarrow$ 23	1.4–0.9	195.248	3.0	2.8	3.91	4.36(13)
	$H^{13}CO^+$ 1 $\rightarrow$ 0	9.6–6.5	304.163	2.8	1.73	0.80	3.04(12)
	CS 2 $\rightarrow$ 1	4.2–3.5	245.474	4.0	7.2	2.14	1.93(13)
	CS 5 $\rightarrow$ 4	1.2–1.0	421.078	3.1	4.9	7.08	2.08(13)
	$C^{34}S$ 5 $\rightarrow$ 4	1.4–1.3	292.244	3.2	5.5	3.31	9.88(12)
	OCS 8 $\rightarrow$ 7	4.2–3.3	31.814	2.8	5.0	0.30	2.88(13) U
	CH_3OH $5_{14} \rightarrow 4_{14}$	2.1–0.8	513.760	2.6	5.3	6.15	9.68(14)
	CH_3OH $5_{14} \rightarrow 4_{14}$	2.5–1.2	656.292	3.4	6.2	4.65	7.32(14)
	CH_3OH $4_{23} \rightarrow 3_{13}$	1.4–0.9	439.772	3.0	3.6	8.71	1.81(15)
	DCN 3 $\rightarrow$ 2	1.7–0.7	385.836	2.5	1.0	3.81	1.0(13)
	HDO $2_{11} \rightarrow 2_{12}$	1.7–1.4	155.451	4.7	2.8	1.44	2.27(14)
	HDO $3_{12} \rightarrow 2_{21}$	1.6–1.5	128.473	3.0	1.4	1.27	6.80(14)
MWC 480	HCN $1_2 \rightarrow 0_1$	3.8–3.0	370.186	3.6	8.5	5.06	4.07(13)
	HCO^+ 1 $\rightarrow$ 0	3.5–2.7	354.646	3.4	8.8	5.75	2.04(13)
	$H^{13}CN$ $1_2 \rightarrow 0_1$	4.4–3.4	310.605	2.7	6.5	3.41	2.90(13) U
	^{13}CO 1 $\rightarrow$ 0	4.3–2.2	984.123	4.2	5.6	10.6	2.32(16)
	CN 1 $\rightarrow$ 0	4.1–2.0	399.447	3.4	6.3	4.60	1.66(14)
	SO $2_2 \rightarrow 1_1$ North	4.3–3.2	361.088	2.8	3.5	4.29	3.70(14) U
HD 163296	HCO^+ 1 $\rightarrow$ 0	7.0–4.0	673.715	3.9	6.7	3.67	1.31(13)
	^{13}CO 1 $\rightarrow$ 0	6.1–3.1	2016.20	4.7	6.3	10.32	2.26(16)
	CN 1 $\rightarrow$ 0	6.0–3.1	1274.33	3.4	6.6	6.56	2.37(14)
GM Aur	HCO^+ 1 $\rightarrow$ 0 North	5.5–3.8	164.464	2.8	3.4	1.23	4.39(12)
	HCN $1_2 \rightarrow 0_1$	4.3–3.3	232.601	2.2	4.4	2.52	2.03(13)
	$H^{13}CN$ $1_2 \rightarrow 0_1$	5.1–3.7	307.88	4.2	4.8	2.66	2.27(13) U
	^{13}CO 1 $\rightarrow$ 0	3.8–2.1	179.535	3.6	4.6	2.28	4.99(15)

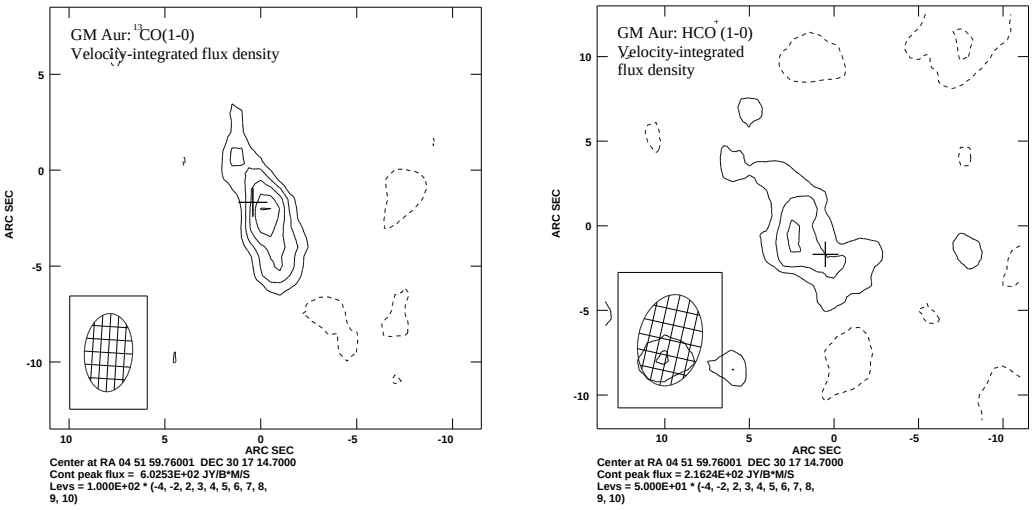

Figure 3.16: OVRO observations of the ^{13}CO and HCO$^+$ $1 \rightarrow 0$ emission from GM Aur.

3.4.5 Line Ratios and Molecular Abundances in Disks

As outlined in Chapter 2, for standard dark cloud abundances, the emission lines from parent isotopomers of common species such as CO, HCO$^+$, HCN, etc., would be expected to be optically thick. Depletion onto grain mantles in the cold midplane region of the disk is likely to substantially reduce the *gas phase* column density of many molecules, however. Thus, for robust estimates of the abundances and excitation of various molecules it is necessary to derive observational estimates of line opacities by examining a range of transitions and isotopomers. If thermal sublimation is the main desorption mechanism, the depletion patterns in disks would be strongly correlated with volatility. The observation of strong emission from non-volatile species such as HCN and HDO, however, reveals that additional mechanisms must also be operating to maintain an observable gas phase.

It is therefore hoped that CO behaves "normally" in the disk since its sublimation temperature is low. If CO remains primarily in the gas phase, it is sufficiently chemically stable that its abundance will be little altered from dark cloud values and can therefore be used as a tracer of the disk gas mass. In the models of Aikawa and co-workers (Aikawa et al. 1996, 1999), CO depletes onto grains at radii greater than 200-300 AU. Inside this radius, the temperature warms to the sublimation temperature of CO (T $\sim$ 20 K) and the gas phase column density rises substantially. The calculated radial distribution of HCO$^+$ is similar to that of CO since it is formed directly from CO via the reaction with H_3^+ formed

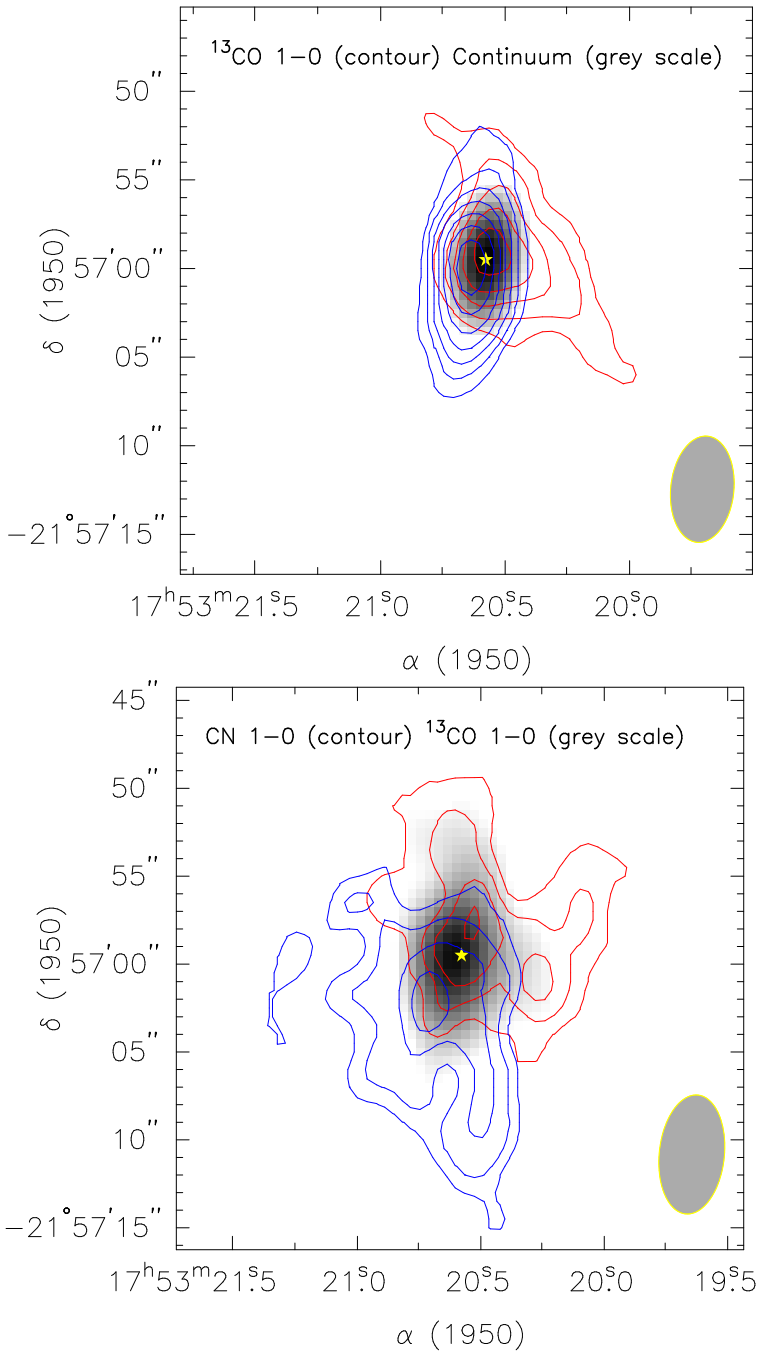

Figure 3.17: OVRO observations of the ^{13}CO and CN $1 \rightarrow 0$ emission from HD 163296. Intensities are integrated over the blue-shifted and red-shifted line components, respectively (also indicated by color).

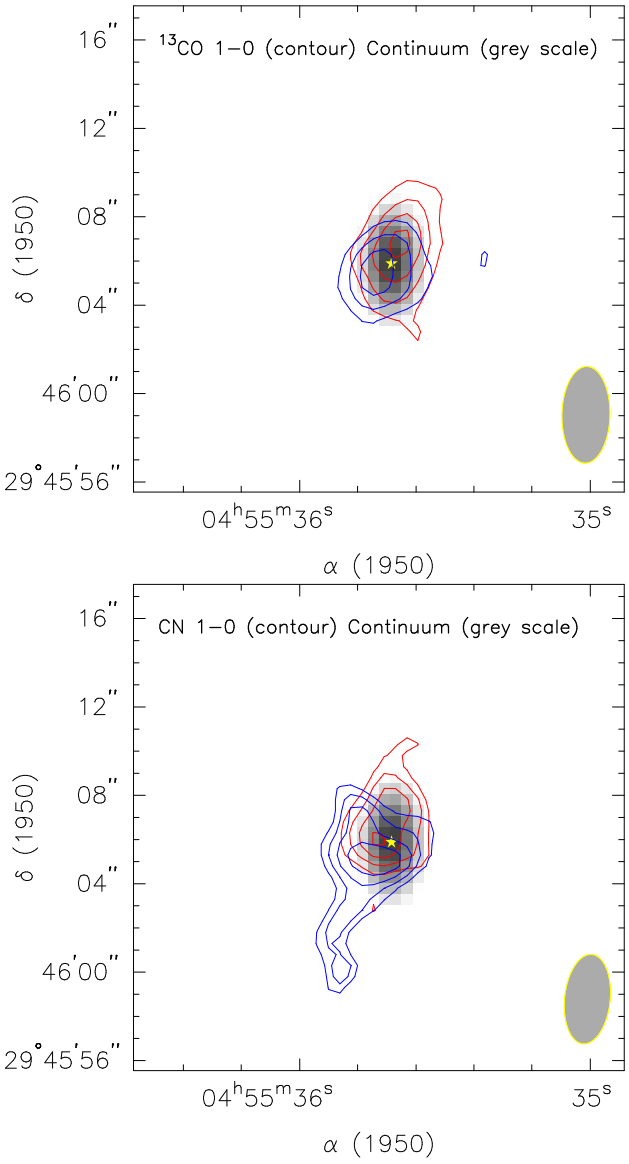

Figure 3.18: OVRO observations of the ^{13}CO and CN $1 \rightarrow 0$ emission from MWC 480. Intensities are integrated over the blue-shifted and red-shifted line components, respectively (also indicated by color).

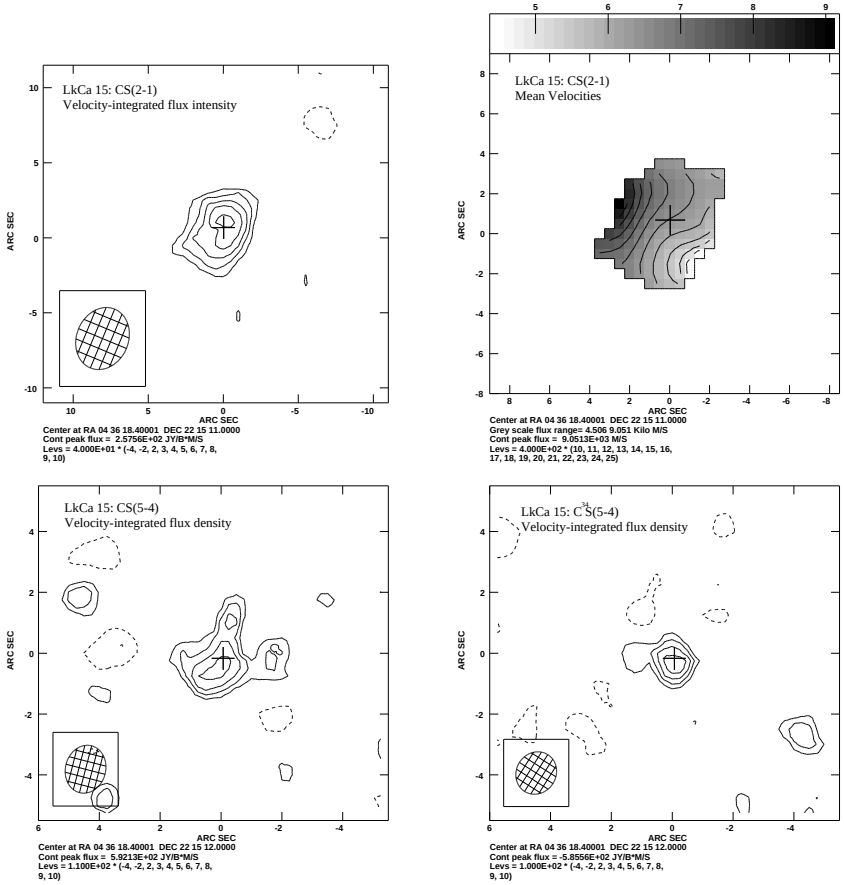

Figure 3.19: OVRO observations of the CS $2 \rightarrow 1$, $5 \rightarrow 4$ and $C^{34}S$ $5 \rightarrow 4$ emission from LkCa 15.

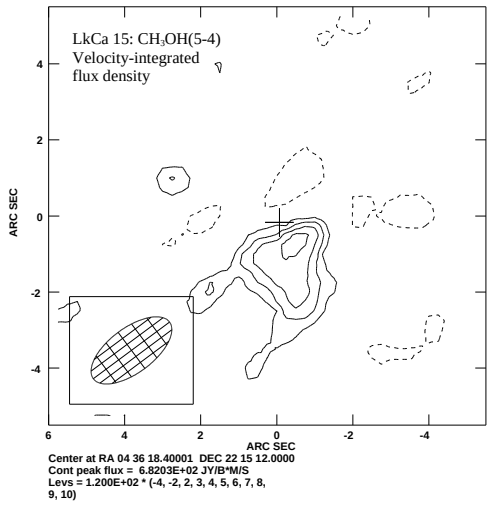

Figure 3.20: OVRO observation of CH_3OH $5 \rightarrow 4$ emission toward LkCa 15.

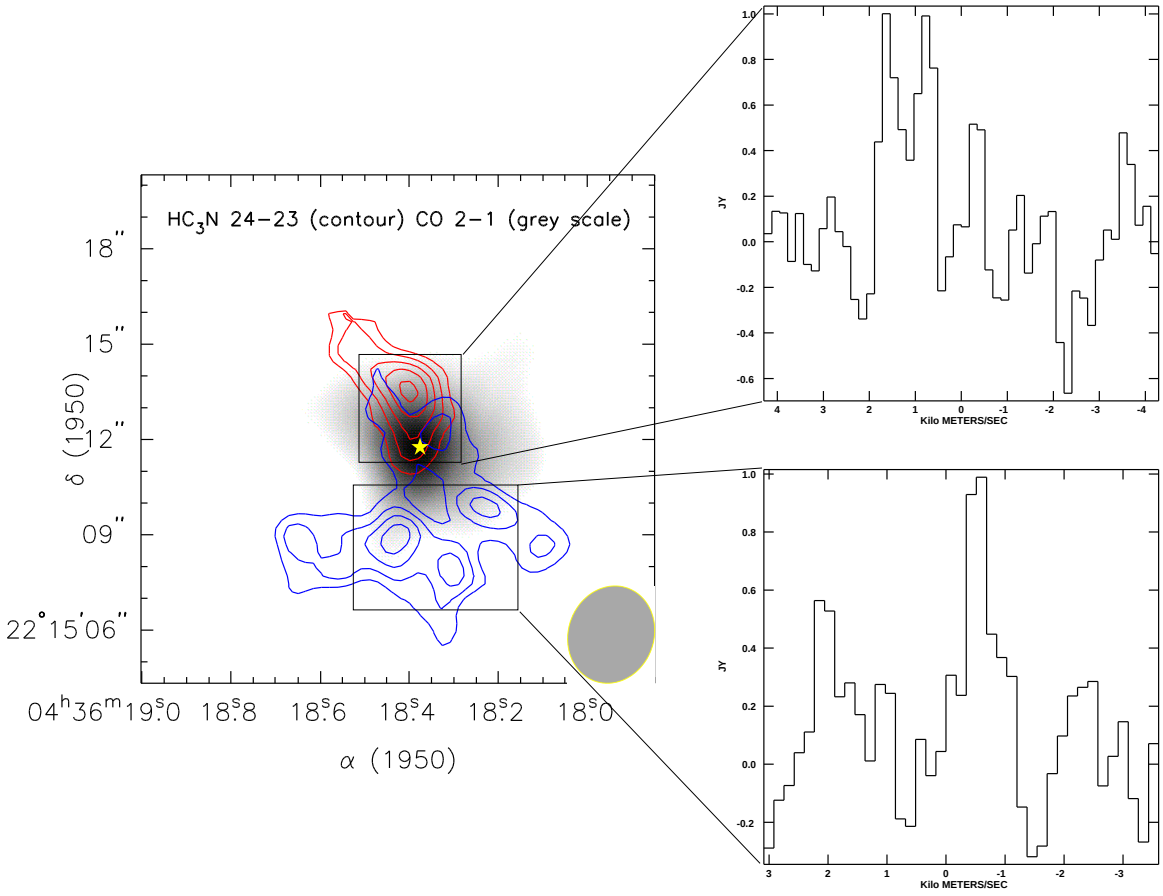

Figure 3.21: OVRO observation of HC_3N 24 $\rightarrow$ 23 emission toward LkCa 15.

by cosmic rays.

The observed ratios of $^{12}CO/^{13}CO$ emission reveal that ^{12}CO is optically thick, but say little about ^{13}CO. Several LkCa 15 transits were therefore devoted to a local oscillator setting containing the $C^{18}O$ J=1 $\rightarrow$ 0 transition, the results of which are presented in Figure 3.22. The observed beam-matched flux density ratio is 5, only somewhat lower than the isotope ratio $[^{13}C]/[^{18}O]$ of 8.3. The ^{13}CO J=1 $\rightarrow$ 0 transition is therefore only somewhat optically thick, and that of $C^{18}O$ is optically thin, and should therefore provide a more reliable estimate of the disk mass, *provided* it remains in the gas phase. From the column density estimates in Table 3.5, disk gas masses of only $\sim 10^{-3}$ $M_\odot$ are derived, values in agreement with those derived from single dish observations of ^{13}CO higher J transitions (Thi & et al. 2000) using the JCMT and CSO. These are nearly two orders of magnitude less than the masses derived from dust emission, far more than can be accounted for by errors either in the dust mass opacity coefficient or in the spectral line radiative transfer. Thus, while CO and its isotopomers are excellent tracers of the disk velocity field, they are not reliable tracers of the disk mass.

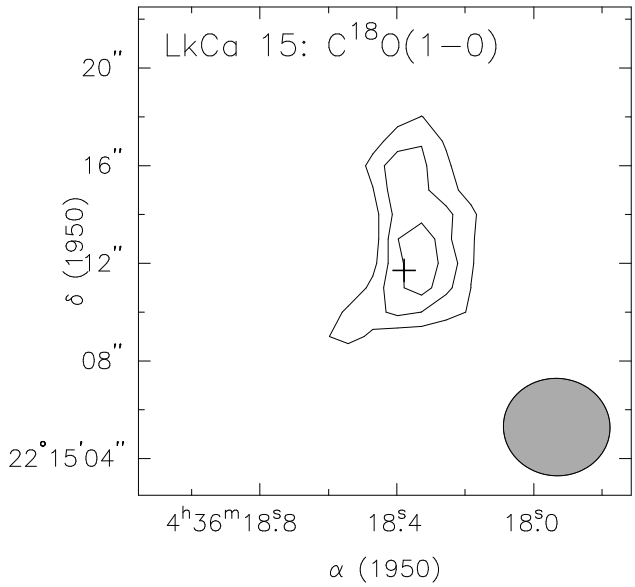

Figure 3.22: $C^{18}O$ emission from LkCa 15. Dust continuum fluxes are close to that observed here, but are not subtracted from the image.

The measured $HCO^+/H^{13}CO^+$ 1 $\rightarrow$ 0, $HCN/H^{13}CN$ 1 $\rightarrow$ 0, and $CS/C^{34}S$ 5 $\rightarrow$ 4 ratios of 2.6, 1.3, and 1.6 toward LkCa 15 indicate that the parent isotopomeric lines are optically

thick. Given the decreased volatility of these species, however, and the $C^{18}O$ results outlined above, it is likely that the isotopically substituted species are optically thin or at most marginally optically thick. Whenever possible, it is these isotopically rarer species that are used to construct the abundance ratios to be compared with the chemical models outlined in the next section. The detections of DCN and HDO in LkCa 15 are particularly exciting (see Figure 3.23), in that they should allow us to directly constrain the (D/H) fractionation in the outer regions of circumstellar accretion disks. The measured (D/H) ratios can then be compared to those measured in comets such as Hale-Bopp (Blake et al. 1999) in order to investigate the origin of primitive solar system bodies. The measured intensities ratios of the (DCN/HCN) transitions lead to (D/H) ratios of <0.5, but are clearly influenced by opacity in the HCN $1 \rightarrow 0$ transition. The DCN/$H^{13}CN$ ratio yields an estimated (D/H) ratio of 0.01, close to that observed in dark molecular clouds. Due to the high atmospheric opacity induced by water, measurements of the (D/H) ratio in water must await the completion of the SOFIA and FIRST heterodyne instruments, but the extension of the DCN emission along the PA seen in the CN $1 \rightarrow 0$ maps clearly indicates the importance of non-thermal desorption mechanisms at large disk radii.

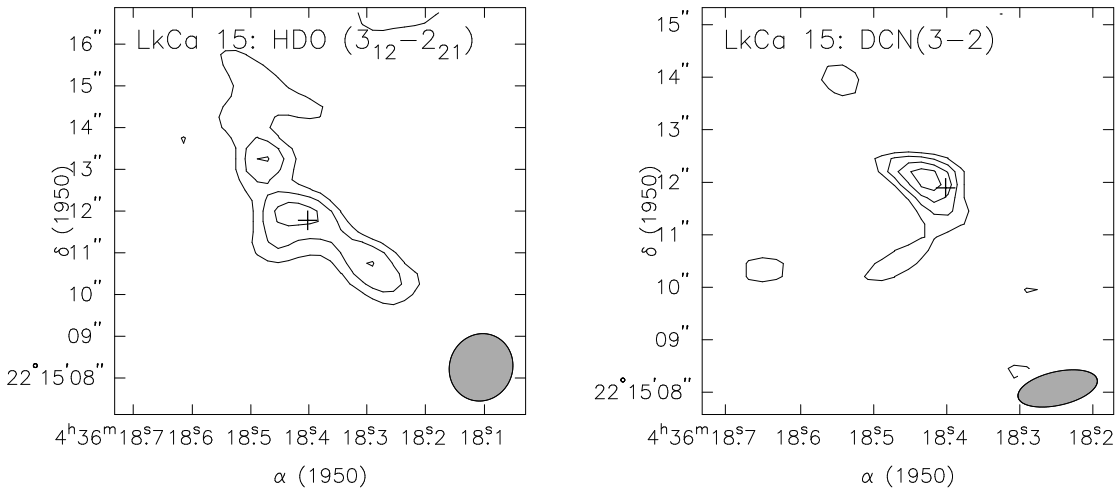

Figure 3.23: OVRO observations of the 1.3 mm HDO and DCN $3 \rightarrow 2$ emission from LkCa 15.

Isotopomeric transitions probe considerably closer to the mid-plane that is inaccessible to the optically thick tracers used to date, and so provide a measure of the depletion provided their absolute abundances can be measured. Chemical abundances are often tied

to an *assumed* CO abundance (typically $\sim 10^{-4}$ that of H_2), however. The best way to analyze the chemical structure of protoplanetary disks would be to carry out Monte Carlo simulations using the predictions of chemical models to compare directly to the observed *flux densities* (Hogerheijde & van der Tak 2000), but that is beyond the scope of this thesis. Here, we compare the ratio of those species and isotopomers with relatively similar optical depths (gauged from the intrinsic line strengths and the measured flux density) to estimate the abundance ratios. Comparing these ratios with chemical models can then provide additional information about the chemical structure of protoplanetary disks.

3.4.6 Comparisons to Chemical Models

It is surprising that so many "early-type" molecules like CN, HCN and CS, whose production is linked to the carbon network (Langer et al. 2000), have been observed in the 'old' LkCa 15 disk, while NH_3, N_2H^+ and SO, which are independent of or destructively linked to the carbon chemistry, are rarely seen. Of the chemical models of protoplanetary disks under development (e.g., Willacy et al. 1998; Aikawa et al. 1996, 1998; Finocchi et al. 1997; Finocchi & Gail 1997), a number deal primarily with the chemistry in the mid-plane of the disk where the cold temperatures and high densities ensure that most molecules are accreted rapidly onto grains at R > 100 AU. As Chapter 2 shows, however, the high optical depth of many millimeter-wave transitions and the temperature gradients set up by the interaction of the disk with radiation from the central stars ensures that it is the *upper regions* of disk that are traced. Here, photons from the central star and the ambient interstellar radiation field can penetrate, and models must explicitly account for the photochemistry that results (Willacy & Langer 2000).

At the surface of the disk, molecules are dissociated by UV radiation, or ionized by UV photons, X-rays and cosmic rays. The X-ray luminosity of T Tauri stars lies in the range 10^{29}-10^{30} erg s^{-1}(Glassgold et al. 1997), while the standard ionization rate by cosmic rays is 1.3×10^{-17} s^{-1}. The protoplanetary disk is irradiated by UV photons from both the interstellar field and the central star. The UV flux from the central star and nearby stars can drive G_0 to values as high as 10^4-10^6 (where G_0 is in units the of "Habing" flux, the estimated average flux in the local interstellar medium, taken to be 1.6×10^{-3} ergs cm^{-2} s^{-1}) (Herbig & Goodrich 1986; Imhoff & Appenzeller 1987; Montmerle 1992; Tielens & Hollenbach 1985; Johnstone et al. 1998). Chemistry in the near-surface regions of disks

therefore shows similarities to both ion-molecule chemistry (Millar et al. 1991) and that in photon-dominated regions (PDRs) (Fuente et al. 1993; Sternberg & Dalgarno 1995; Jansen et al. 1995). Thus, to compare the observed emission with that predicted by models of the outer regions of circumstellar accretion disks, models which consider the vertical structure of the disk and which can predict the spectral line intensities or column densities of observable molecules are needed.

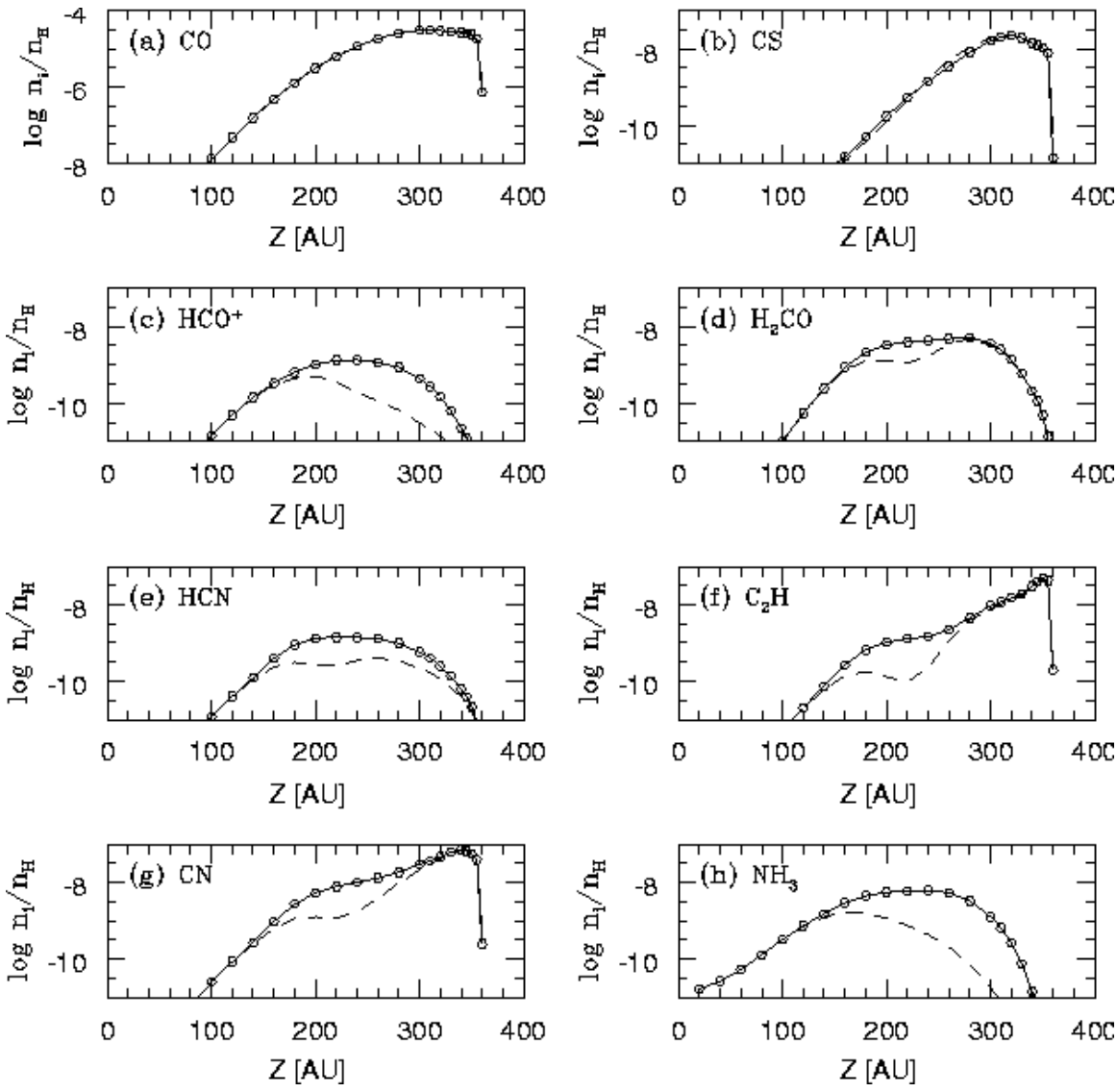

Figure 3.24: Vertical distribution of molecules at R=700 AU and t=3×10^5 yr, see Aikawa & Herbst (1999) for details.

Two recent models, those by Aikawa & Herbst (1999) and Willacy & Langer (2000)

, have begun to examine the vertical chemical distributions in disks. Aikawa & Herbst (1999) have simulated the effects of desorption by using a reduced sticking coefficient to lower the freezeout rate, by starting with molecules in the gas phase, and by assuming the temperature to be isothermal with height. They examined all radii outside of 0.5 AU and a vertical region extending from the mid-plane to a height with a UV flux of $\sim$1 G_0 (the UV radiation field will be larger if there are additional nearby stars). Figure 3.24 shows the vertical distributions of various molecules at R=700 AU and at t=3×10^5 yr in the Aikawa & Herbst (1999) model. The solid lines are for the case in which X-rays are included. At the midplane, most of the molecules are adsorbed onto grains due to the low temperature and the high density. At or near the surface, molecules tend to be dissociated by UV radiation. As a result, CN and C_2H have their peak abundances at larger heights compared with more stable species such as HCN and NH_3.

The model of Willacy & Langer (2000) includes non-thermal desorption mechanisms, drawing upon recent laboratory work by Westley et al. (1995) which has found that photodesorption may be considerably more efficient than previously thought. The Willacy & Langer (2000) model also considers for the first time the chemical effects of the layer of warm gas and dust at the surface of the disk predicted by two-layer radiative transfer models (Chiang & Goldreich 1997). Molecules are assumed to be depleted onto grains before they enter the disk. Interestingly, photodesorption from the *interstellar* radiation field is found to dominate at large disk radii due to the very different slant angles experienced by the stellar and external radiation fields. The general consequence is that the abundances of many molecules, including high sublimation temperature volatiles such as HDO as well as photodissociation products such as CN, increase with radius.

External radiation fields may play an especially important role in explaining the observed molecular emission from the disk surrounding LkCa 15, for which the K5 star HD 284589 lies only 30″ away in the plane of the sky. If HD 284589 lies at the same distance as LkCa 15, the resulting G_0 values can be as large as 10^2, values easily high enough to affect the physical and chemical conditions in the LkCa 15 disk. For example, photoevaporation via ultraviolet photon heating has been proposed as an efficient disk dissipation mechanism (Johnstone 2000). Photoevaporation can proceed either via the central star or external sources. For external photoevaporation, Johnstone et al. (1998) showed in general that far ultraviolet photons (FUV), which heat the molecular and neutral gas to $\sim 10^3$ K, are most

efficient at liberating material from young, extended disks in slow (3−10 km s^{-1}) thermal disk winds. An evaporative flow can only exist if the thermal pressure exceeds the local gravity, so an evaporative disk wind can exist only beyond a critical radius $r_g = GM_*/a^2$ (where a is the sound speed of the gas). In neutral, FUV dominated flows, a $\sim$ 3 km s^{-1}. For LkCa 15 ($M_* = 0.81\ M_\odot$), the gravitational radius is $r_g \sim$ 80-180 AU, which could explain the outward gradients needed to explain the CN maps shown in Figure 3.4 and Figure 3.9. Photochemistry and photoevaporation in LkCa 15 may be further enhanced by the dust settling inferred from the small H/h value needed to fit the disk SED.

To compare the observed abundances with those of the chemical models, it is better to use ratios such as CN/HCN. Provided the optical depths and excitation requirements are similar, ratios should cancel out some of the uncertainties in source size, disk inclination, etc. The large CN/HCN ($\sim$10) abundance ratio seen toward LkCa 15 is characteristic of the chemistry in PDRs. In PDR models (Fuente et al. 1993; Sternberg & Dalgarno 1995; Jansen et al. 1995), several regions can be identified, each characterized by a different chemistry and by different dominant constituents. CN/HCN abundance ratios of $\sim$10, for example, occur at depths for which $\tau_\nu \sim 2$ (Dutrey et al. 1997).

The general dependence of various species on A_V in PDRs is as follows (Jansen et al. 1995): The $C^+ \rightarrow C$ conversion zone occurs in the outer part where UV radiation penetrates, up to $A_V \approx 1.5$ mag. Most elements are still in atomic form in this zone, with the exception of hydrogen, which is already molecular. Near A_V=2 mag the "radical region" occurs. In the radical region the chemistry is dominated by simple, mostly diatomic, species such as CH, CH_2, CN and OH. Like H_2, CO is self-shielding against photodissociation (though not as effectively as H_2), so its abundance rises rapidly in this region. From $A_V \approx 3$ to $A_V \approx 5$ mag the conversion to more complex molecules takes place. Photodissociation and photoionization are no longer important chemical reactions; their role as dominant destruction processes is taken over by oxygen, which is still primarily in atomic form. This region will therefore be denoted as the "atomic O" region. Finally, for $A_V \geq 5$ mag, oxygen is converted into O_2 and H_2O, and dark cloud chemistry has been reached.

The Ionization Balance in Circumstellar Disks

Photoionization and cosmic ray ionization of H_2 rapidly leads to the formation of H_3^+, the pivotal species in ion-molecule models of molecular cloud chemistry. The low proton

affinity of H_2 ensures that H_3^+, which has no rotational spectrum, will undergo proton transfer reactions with abundant neutral species such as CO and N_2. In disks, gaseous CO and N_2 exists in regions well removed from the midplane, where the temperature warms to the sublimation point for CO and N_2 (T $\approx$ 20-30 K). As a homonuclear diatomic molecule, N_2 has no electric dipole allowed rotational transitions. The isoelectronic ions HCO^+ and N_2H^+ are both observable, however, and can be used to estimate the fractional ionization in the disk. For large visual extinctions, the main formation paths for HCO^+ and N_2H^+ are $CO + H_3^+ \rightarrow HCO^+ + H_2$ and $N_2 + H_3^+ \rightarrow N_2H^+ + H_2$, respectively. The main destruction path for HCO^+ is dissociative recombination with electrons; for N_2H^+ it is proton transfer to CO at dark cloud CO abundances, or dissociative recombination if the CO is heavily depleted onto grains. With proper modeling, the N_2H^+/HCO^+ ratio can therefore be used to estimate the N_2/CO ratio. At low visual extinction, PDR models (Fuente et al. 1993; Jansen et al. 1995) show that HCO^+ and N_2H^+ abundances are strongly suppressed, with HCO^+ formed mainly by the reactions

$$CH_2^+ + O \rightarrow HCO^+ + H$$
$$C^+ + H_2O \rightarrow HCO^+ + H$$
$$CO^+ + H_2 \rightarrow HCO^+ + H$$

and N_2H^+ by

$$N_2^+ + H_2 \rightarrow N_2H^+ + H$$

Therefore, the N_2H^+/HCO^+ ratio is not a good proxy for the N_2/CO ratio in PDRs, but the HCO^+ abundance still provides a rigorous lower bound to the fractional ionization.

N_2H^+ can be destroyed by proton transfer to CO and H_2O where these molecules are not significantly condensed onto grains (Bergin & Langer 1997), which might explain the negative result of the N_2H^+ observations.

Due to the large opacity of HCO^+, the less optically-thick ^{13}CO and $H^{13}CO^+$ lines should be used to (roughly) estimate the electron abundance. From Table 3.5 we find the ratio of ^{13}CO $1 \rightarrow 0$ over $H^{13}CO^+$ $1 \rightarrow 0$ to be $\sim 10^5$. Since ^{13}CO is still moderately thick and $H^{13}CO^+$ $1 \rightarrow 0$ is near the sensitivity limit of the array, the actual ratio could be as

high as 10^6. Adopting a maximum fractional abundance of CO near 10^{-4} thus results in an upper limit to the abundance of HCO^+ of 10^{-10}, which also sets a minimum floor for the electron fractional abundance.

In the outer disk, transport likely depends critically on the degree of ionization. At the surface of the disk, both photons and cosmic rays may be an important source of ionization, but the photon penetration depth is very short compared to the disk thickness. Even cosmic rays are exponentially attenuated for columns >100 g cm^{-2}, thus suggesting the possibility of layered accretion (Gammie 1996) with a turbulent surface layer. The transport or mixing process might be important to bring freshly made early-type molecules like CN, HCN or even deuterated species back to the interior of the disk which, in the long run, can affect the composition of early solar system objects such as comets. More analyses of the chemical composition of comet Hale-Bopp may be found in Chapter 4.

Nitrogen-Bearing Molecules in Disks

The most easily observed nitrogen-bearing molecules in disks are CN, HCN, and HNC. Even the HC_3N 24 $\rightarrow$ 23 transition has been detected toward LkCa 15. Figure 3.9 and Figure 3.21 reveal some unique features of the nitrogen-bearing molecules in the protoplanetary disks. HCN and HC_3N show a velocity gradient along the disk major axis, but the seperation of the red- and blue-shifted emission are much larger than those of CO/HCO^+, indicating their existence at the outer part of the disk. The velocity gradient of CN toward LkCa 15 shows a tendency that is approximately perpendicular to the disk major axis, as might be expected for an outflow or disk wind. Toward HD 163296, the CN velocity gradient is along the disk major axis (Figure 3.13). Detailed comparisons of channel maps of CN 1 $\rightarrow$ 0 with those of CO 2 $\rightarrow$ 1 or ^{13}CO 1 $\rightarrow$ 0 are shown in Figure 3.25, Figure 3.26 (for LkCa 15) and Figure 3.27, Figure 3.28 (toward HD 163296). To improve the S/N, an eight channel channel Hanning taper has been applied to the data. The CN 1 $\rightarrow$ 0 emission toward LkCa 15 appears to follow the edge of the CO 2 $\rightarrow$ 1 features. In particular, the red-shifted CN 1 $\rightarrow$ 0 emission does not exhibit a Keplerian rotation pattern and extends markedly to the southeast at a position angle nearly orthogonal to the disk major axis.

Similar, though less obvious, kinematic patterns are observed for HD 163296. While the ^{13}CO 1 $\rightarrow$ 0 emission closely that expected for Keplerian rotation , the CN 1 $\rightarrow$ 0 emission also shows a blue-shifted extension to the south and a red-shifted extension to the

north. The overall PA and velocity pattern of CN extension is in good agreement with the STIS coronagraphic imaging of HD 163296 (Grady et al. 2000) which shows that the disk is accompanied by a chain of nebulosities at PA $\sim 42.5°$, compatible with the detection of a Herbig-Haro Flow; and with the spectral imaging of the disk in Lyα (Devine et al. 2000), which indicates that the HH objects to the SW of the star are part of an approaching jet while those to the NE are receding. So, the CN emission from both of these sources shows deviations from Keplerian rotation that may somehow be related to processes at the surface of the disks. The further investigation of these interesting facets of nitrogen-bearing molecules in disks awaits the development of more powerful imaging instrumentation at millimeter- and submillimeter-wave frequencies.

The predicted CN/HCN abundance ratio shows large variations with A_V, with the CN abundance peaking around $A_V \approx 2$ mag in the "radical region." CN and HCN are formed primarily through neutral-neutral reactions in PDRs:

$$N + CH_2 \rightarrow HCN + C$$
$$N + CH \rightarrow CN + H$$

and to a lesser extent

$$C + NH \rightarrow CN + H$$

At high A_V, CN and HCN, and HNC can all be formed from the dissociative recombination of the $HCNH^+$ ion:

$$\begin{aligned} HCNH^+ + e \rightarrow\ & CN + H + H \\ & \rightarrow HCN + H \\ & \rightarrow HNC + H \end{aligned}$$

CN, however, is destroyed by atomic oxygen, whereas HCN is not. Therefore, the CN abundance becomes lower than that of HCN in the "atomic oxygen region." HCN can be ionized by the fast reaction $HCN + H^+ \rightarrow HCN^+ + H$, and so the CN/HCN ratio increases by a factor 15 (Fuente et al. 1993) from A_V=10 mag (CN/HCN $\sim$ 1) to A_V=6 mag (CN/HCN $\sim$ 15). The increase in the CN/HCN ratio is driven primarily by the

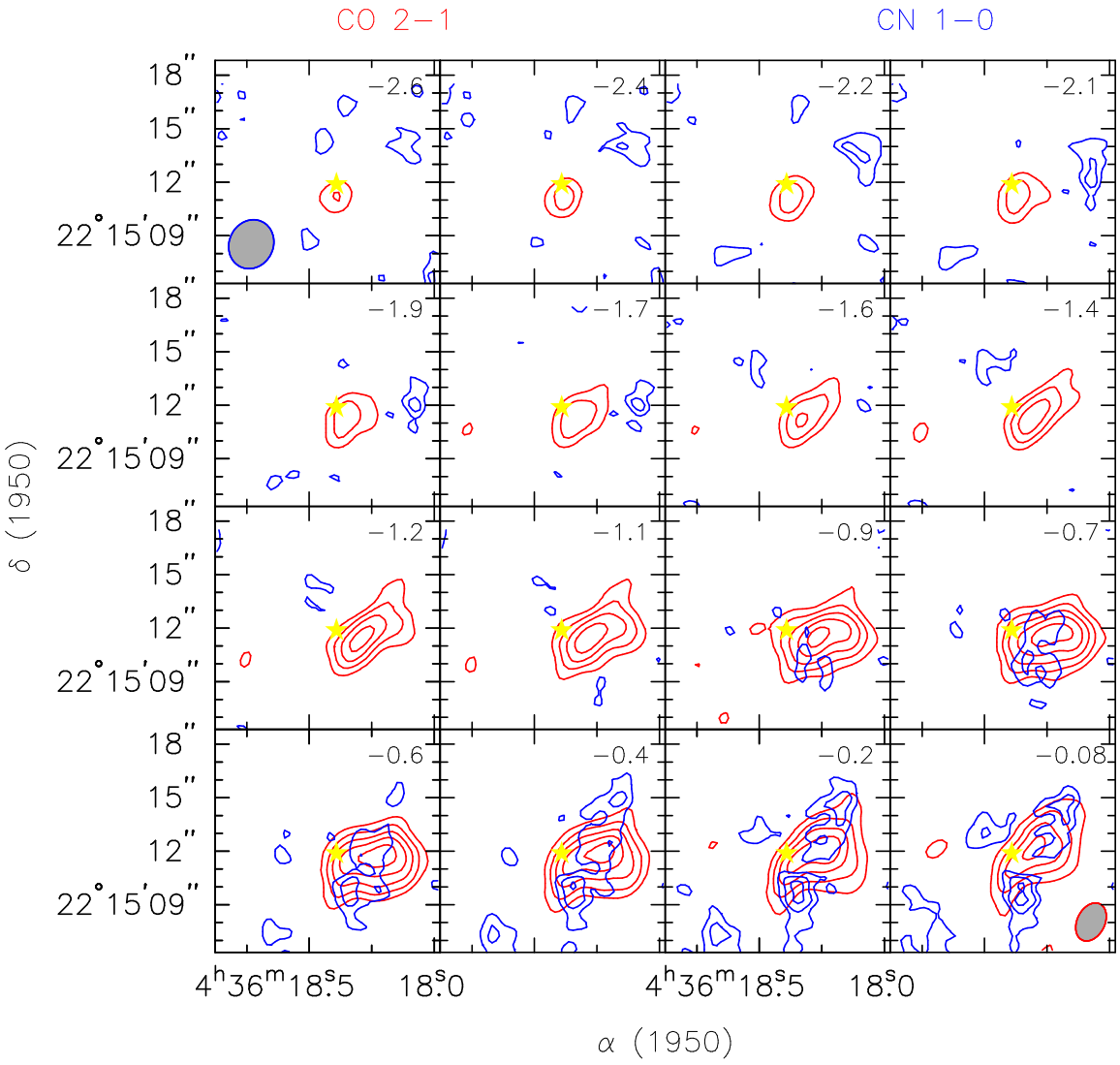

Figure 3.25: Channel maps of the blue-shifted CO 2 → 1 and CN 1 → 0 emission toward LkCa 15.

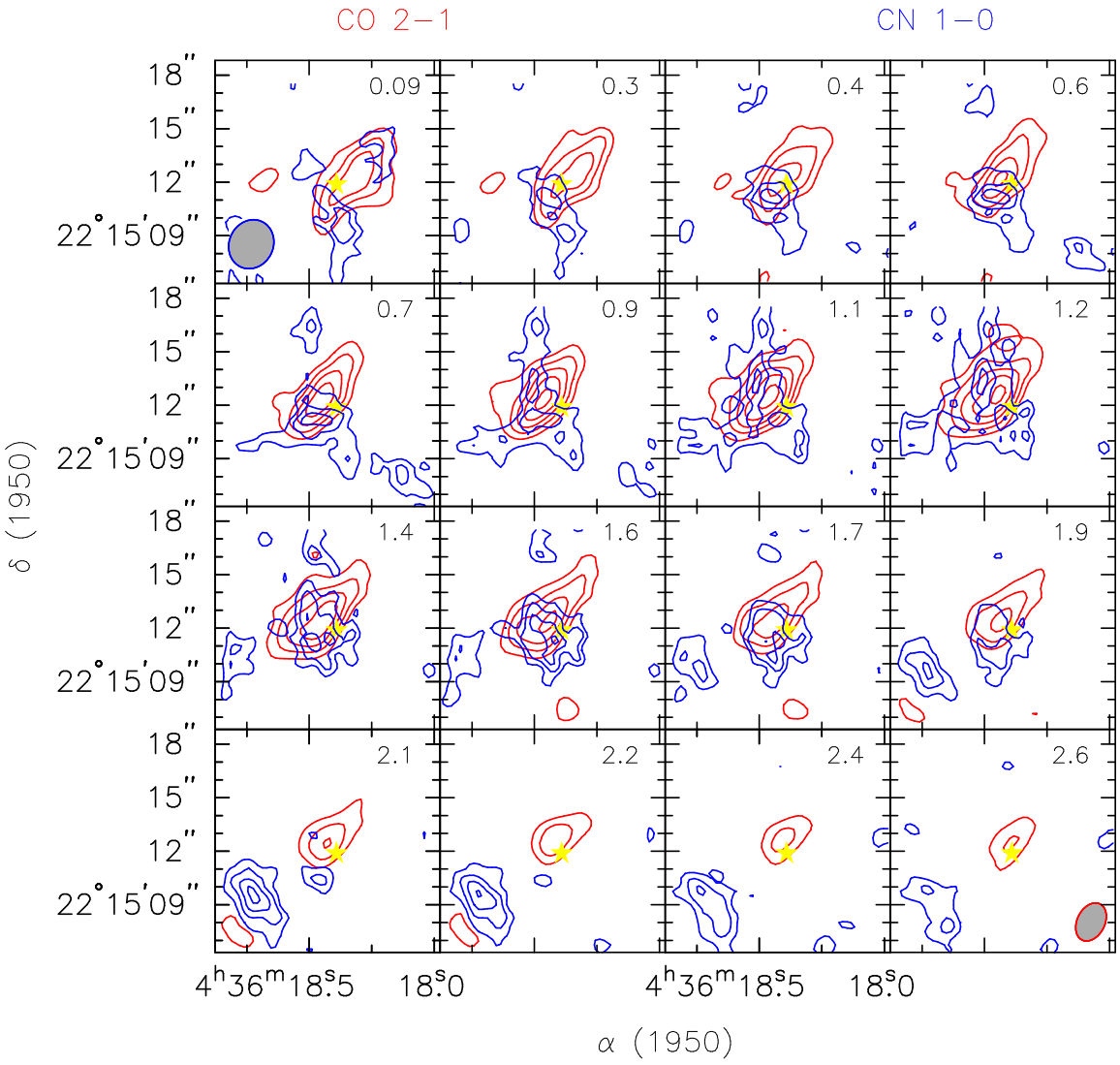

Figure 3.26: Channel maps of the red-shifted CO 2 → 1 and CN 1 → 0 emission toward LkCa 15.

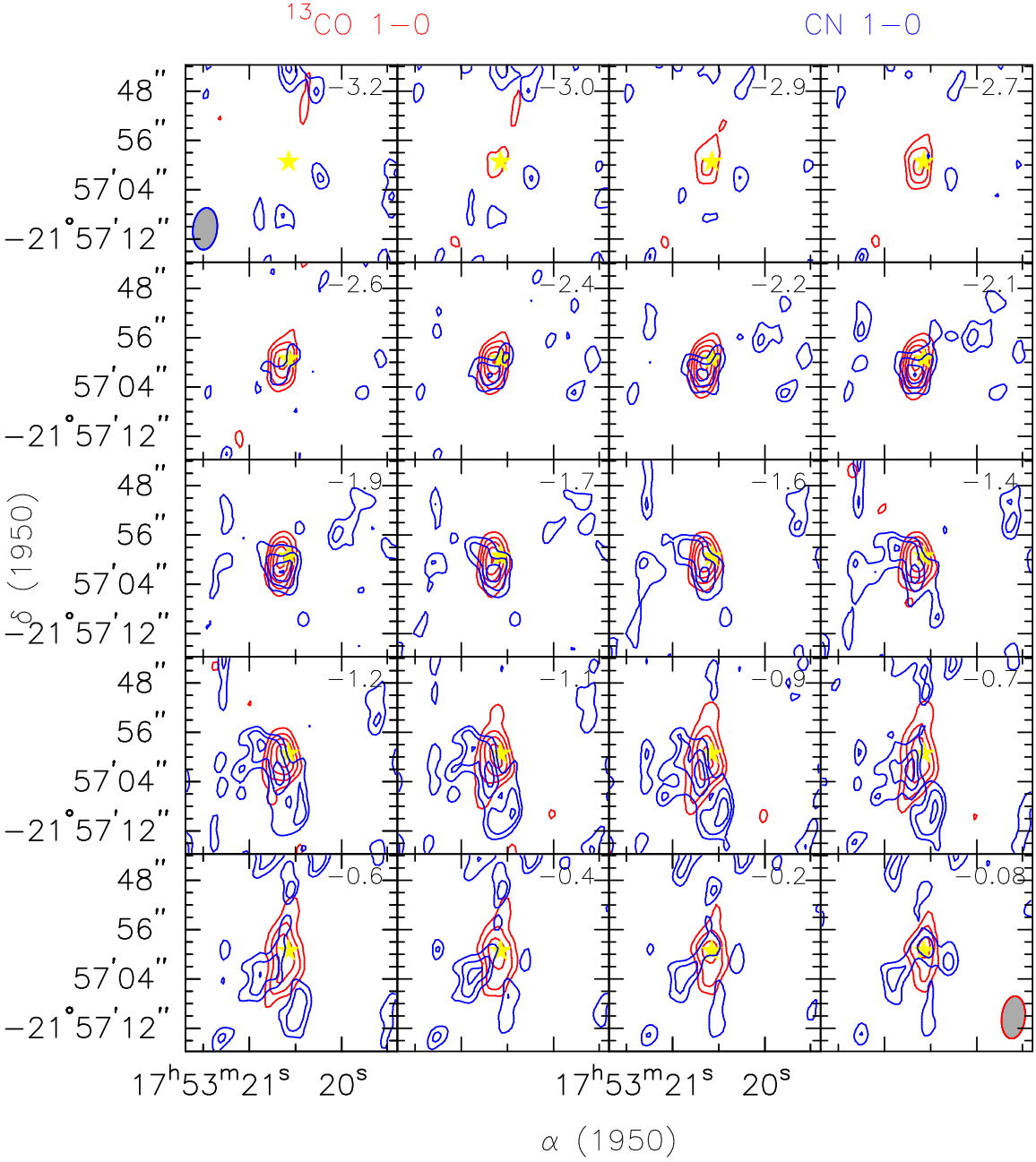

Figure 3.27: Channel maps of the blue-shifted CO 2 → 1 and CN 1 → 0 emission toward HD 163296.

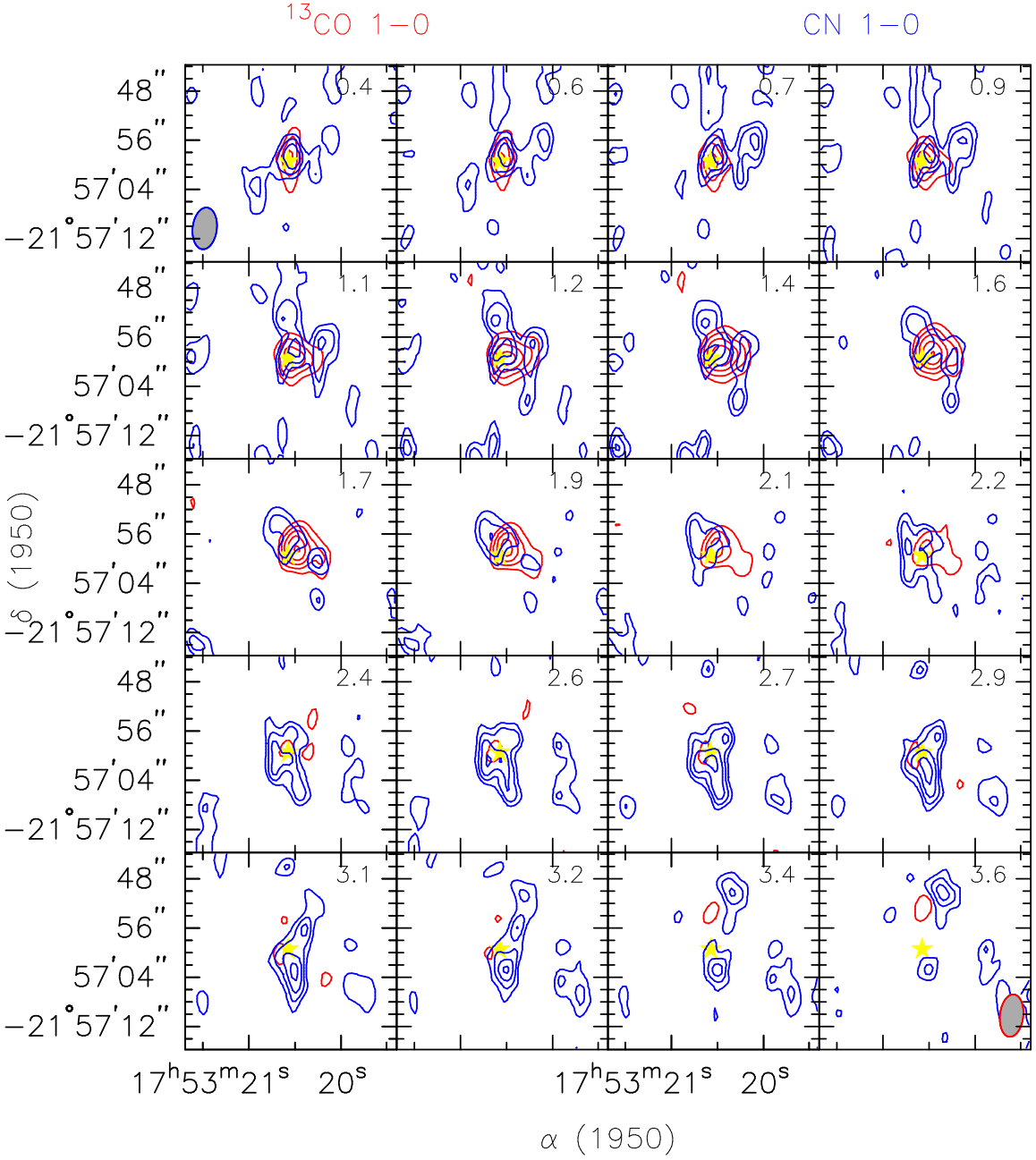

Figure 3.28: Channel maps of the red-shifted CO 2 → 1 and CN 1 → 0 emission toward HD 163296.

decrease in the abundance of HCN, and so the CN/HCN ratio has been suggested as a tracer of enhanced UV fields (Fuente et al. 1993).

Differences in the HCN and HNC abundances can be caused by a variety of processes, several of which appear to be temperature sensitive (Jansen et al. 1995). Indeed, the HCN/HNC ratio in warm cloud cores is observed to be $\gtrsim 100$, while in cold clouds the ratio is $\sim$1 (see Irvine et al. 1985 and references therein, Jansen et al. 1995). HNC may be converted to the more stable form HCN by temperature-dependent auto-isomerization (this could conceivably occur either in the gas phase or in grain mantles), or the formation mechanism itself may be temperature dependent: Ion-molecule reactions to produce $HCNH^+$ should equally favor HCN and HNC, but the neutral chemistry may be quite different. HCN can be formed from $N+CH_2$, whereas HNC is synthesized via a $C+NH_2$ channel. Models (Fuente et al. 1993) predict that the HNC/HCN ratio decreases by a factor 5 from 10 mag to 6 mag for a constant kinetic temperature of 30 K, and decreases by the same factor if the visual extinction is held constant but the kinetic temperature increased from 15 to 50 K. HNC/HCN will thus decrease with higher temperatures and stronger UV fields.

In summary, very different behavior is expected for the molecular abundance ratios when the chemistry is dominated by a gradient in the UV field. Fuente et al. (1993) shows that for a constant kinetic temperature and varying UV field, the abundance of most molecular species decreases with increasing UV radiation. Some species, however, increase at moderate UV fields (CH, CH^+, CH_2, $CH_2{}^+$, $CH_3{}^+$, C_2, C_2H and CN). Because of this behavior, CN and C_2H turn out to be very sensitive to the presence of UV radiation. Thus, the luminosity of the central star is expected to affect the abundance ratios of CN and other molecules. Since UV radiation is attenuated mainly by grains, UV photons will penetrate more deeply into the disk as grain sedimentation and growth proceed and photochemistry will become more important. Table 3.6 summarizes the effects of stellar luminosity and dust settling in the four sources studied at OVRO. ^{13}CO is used as a reference to normalize optical depth variations. As can be seen, the observed CN/HCN ratio varies tremendously. The large CN/HCN and low HNC/HCN ratios observed toward LkCa 15 and HD 163296 indicate that there are strong UV fields at the surfaces of these disks. For HD 163296 the radiation field likely arises from the central star, while in LkCa 15 a combination of dust settling (from the fitted H/h value) and the nearby presence of HD 284589 are likely to be responsible. GM Aur lies at the other extreme: It has a low UV luminosity and from SED fits the dust and

gas are thought to be well mixed, and so would be predicted to have a low CN/HCN ratio, as observed. MWC 480 lies between these extremes, and has a moderate CN/HCN ratio of 4. The observed patterns can therefore be rationalized based on what is known about the disk physical state and central star, but a more extensive sample will be needed to truly disentangle these effects.

Table 3.6: Effects of Luminosity and Dust Settling on the CN/HCN Ratio in Disks

Source	Luminosity($L_\odot$)	CN/^{13}CO	CN/HCN	H/h
LkCa 15	0.72	~ 0.01	~ 10	1.0
GM Aur	0.8	~ 0.004	$\ll 1$	4.0
MWC 480	32.4	~ 0.007	~ 4	1.7
HD 163296	30.2	~ 0.01	$\gg 50$	2.0

[2]Note. HCN/^{13}CO is used for GM Aur instead of CN/^{13}CO.

Sulfur-bearing Molecules in Disks

The most abundant sulfur-bearing molecules CS and SO can exhibit significant differences in their evolutionary history because SO is produced mainly through a reaction of S with OH and O_2 and is destroyed by atomic carbon to produce CS. The chemistry of CS is therefore linked to the carbon network , while SO has large concentrations in equilibrium (Langer et al. 2000). Most previous calculations (e.g., Prasad & Huntress 1982; Sternberg & Dalgarno 1995) predicted that in the center of dark clouds, most of the sulfur is converted into SO_2 and to a lesser extent SO. Models of circumstellar disks by Willacy et al. (1998) also predict that SO_2 should contain most ($\sim$ 90%) of the available sulfur. The high abundance of SO_2 results from the reaction between oxygen atoms and SO on the surfaces of dust grains in the cold outer parts of the disk. As the grains move inwards the temperature increases, with the SO_2 being desorbed at $T > 70$K. These predictions are not in accord with PDR observations (Jansen et al. 1995), and with our observations in which CS has been detected in two transitions (the J=2 $\rightarrow$ 1 and 5 $\rightarrow$ 4 lines, respectively) but SO and SO_2 have not yet been seen (see Figure 3.19).

Simple hydrocarbons are important in initiating CS-chemistry:

$$CH + S^+ \rightarrow CS^+ + H$$
$$CS^+ + H_2 \rightarrow HCS^+ + H$$
$$HCS^+ + e \rightarrow CS + H$$

while SO and SO_2 are formed mainly by neutral-neutral reactions:

$$S + O_2 \rightarrow SO + O$$
$$S + OH \rightarrow SO + H$$
$$HS + O \rightarrow SO + H$$

The most important cation in the sulfur chemistry is HCS^+, but is present at such a low abundance that it is difficult to observe with current arrays. Figure 3.29 therefore presents the channel maps of CS $2 \rightarrow 1$ emission with that from the HCO^+ molecular ion. As the figure shows, the correlation of CS with this HCS^+ proxy is very good. Several attempts to observe SO and SO_2 have resulted in upper limits only. The low abundances of SO and SO_2 could be caused by the lack of efficient low temperature gas phase formation channels and the high photodissociation rates near disk surfaces (Hasegawa et al. 2000). In disk interiors, depletion of sulfur species onto grain mantles should be rapid at the large distances observable with the OVRO Millimeter Array.

Complex Molecules in Disks

A wide variety of complex species are observed in molecular cloud cores and in comets (see Chapter 4). Many, such as CH_3OH, are thought be formed on grain mantles in dense clouds. Models of disk chemistry also predict that methanol should have a high abundance as a result of chemical processing on grains (Willacy et al. 1998). We indeed detect CH_3OH toward LkCa 15, as Figure 3.20 shows. Once in the gas phase, methanol and other complex molecules can drive a rich chemistry that has been widely observed in sources known as hot cores – warm, dense regions of gas and dust near young, massive protostars (van Dishoeck & Blake 1998). Similar regions may also exist in circumstellar disks, especially in the warmer, potentially planet-forming region inside of 20-30 AU. Present instrumental sensitivity is not sufficient to study this inner region, however, nor to detect the lines from more complex

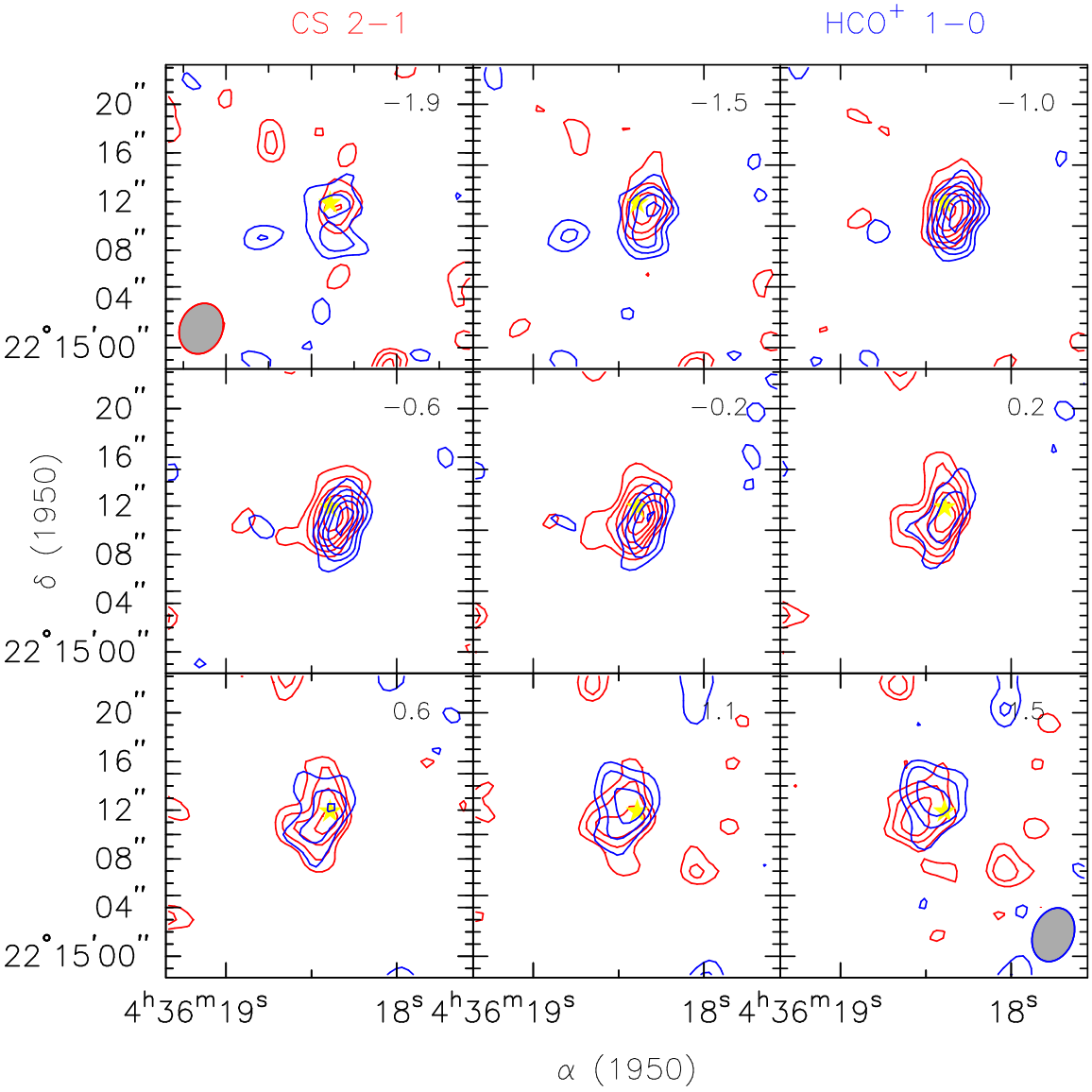

Figure 3.29: Channel maps of the HCO^+ $1 \rightarrow 0$ and CS $2 \rightarrow 1$ emission toward LkCa 15. The velocities listed in the upper right of each panel denote the offset from the systemic velocity of 6.0 km/s.

molecules whose rotational emission is spread over a plethora of transitions.

Deuterium Fractionation in Disks

Studies of the deuterium fractionation in protoplanetary disks and a comparison with (D/H) values for molecules in comets and molecular clouds should provide clues as to the physical parameters and time scales in disks. In dense clouds, most of the deuterium is in HD. The reaction

$$HD + H_3D^+ \rightleftharpoons H_2 + H_2D^+ + \triangle E$$

is strongly driven to the right since the reactants are of lower energy (by $\triangle$E/k=273 K), the energy difference $\triangle$E being the difference between the zero-point energies relative to the minimum of the molecular potential energy curve. Such energy differences also exist for other molecules; for example, $\triangle$E(HCN-DCN)=312 cm^{-1}. Observations of interstellar molecules containing the D isotope in general show large enhancements of molecular abundances compared with the D/H ratio.

Our measurement of high D/H ratios is consistent with those seen in comet Hale-Bopp. This does not necessarily mean that the high D/H ratio can be taken as evidence for unprocessed interstellar matter in comets, however. Aikawa & Herbst (1999) have investigated the evolution of abundance ratios between singly deuterated isotopomers and normal species for molecules in protoplanetary disks. Although they found that the molecules in the disk have D/H ratios similar to those found in dense clouds, they show that the deuterium fraction is acquired while matter is collapsing to form protoplanetary disks and within the disk itself. Both the absolute chemical abundances and the D/H ratios among various species therefore reflect a continuous evolutionary process, and cannot be described as solely "interstellar" or "nebular". As noted above, the OVRO map of DCN emission from LkCa 15 (cf. Figure 3.23) shows the same morphology observed in CN, which traces enhanced UV fields on the surface of the disk. Willacy & Langer (2000) predict an increase in H_2O with radius due to the photodesorption by external UV photons. D/H fractionation to produce the observed DCN and HDO can occur either on the grains or in the gas phase, but just as for CN the models and observations suggest that the highly deuteriated species such as those found in comets can be actively produced in disks.

3.5 Conclusion

The observations presented in this chapter concentrate on $\lambda \sim 3$ mm transitions of HCN/HCO^+ and ^{13}CO/CN in LkCa 15, GM Aur, MWC 480, and HD 163296. These disks were chosen based on their large spatial extent, Keplerian kinematic patterns, and strong CO emission. Two surround classical T Tauri stars and two encircle Herbig Ae stars, enabling the influence of the central stellar luminosity on the chemical composition of the disk to be investigated. All are well isolated from dense molecular clouds.

Even at a resolution of $2''$ (or a linear scale of $\sim$300 AU at the distance of Taurus and Ophiuchus), the OVRO observations show that the chemistry in circumstellar disks is sensitive to both the central stellar luminosity and the degree of dust settling toward the disk midplane. Abundance ratios such as CN/HCN and HCO^+/CO serve as unique probes of pivotal processes such as photoevaporation or cosmic ray induced ionization. The observed lower limit to the fractional ionization of 10^{-10} is sufficient to support instabilities that are likely to dominate the transport mechanisms in the outer reaches of protoplanetary disks. CN/HCN gradients in the T Tauri and Herbig Ae star disks appear to be correlated with the local UV radiation field and with the degree of dust settling as judged by recent fits to their spectral energy distributions, illustrating the important role of photochemistry at large disk radii.

The disk emission toward LkCa 15 is particularly intense, with many molecules being detected, including HCN/HCO^+ and their ^{13}C-isotopomers, DCN, CN, CH_3OH, CS, SO, ^{13}CO, and $C^{18}O$. The overall abundance patterns are consistent with recent models of photon-dominated chemistry in the near surface regions of flaring circumstellar disks that also provide a natural explanation for the mid- and far-infrared properties of the disk SED. The strength of the CO emission and the double peaked nature of the CN and HCN distribution, however, is most naturally explained by a cold disk interior underlying the chemically active disk surface(s). Substantial volatile depletion onto grain mantles occurs in the interior, and as a result the emission from molecular lines is a more robust tracer of the disk velocity field than its mass. Finally, the detection of DCN has made possible the first determination of the critical D/H ratio in protoplanetary gas. At present, the data provides an approximate value of 0.01 for the DCN/HCN ratio, a value close to that found in the dark molecular clouds, but one that clearly arises from *in situ* disk chemistry.

Chapter 4 OVRO Observations of Comet Hale-Bopp

4.1 Introduction

Information about the planetesimal-building stage of the outer pre-solar nebula is contained in the chemical and physical properties of comets and other icy bodies such as Kuiper Belt Objects. Comets may well yield the least altered material due to their small size, and may preserve both the matter of the early solar system as well as presolar material inherited from the parent interstellar cloud which collapsed to form the Sun. It is therefore hoped that the observations of comets, especially studies of their volatile and isotopic composition, will provide clues concerning the origin of comets, the physical conditions of the lowest-temperature region of the solar nebula, and the coupled evolution of ices, solids, and gases along the entire path from the interstellar medium to mature planetary systems.

Since the first spectroscopic observations of comets made by Giovanni Donati in 1864 and the first detection of cometary molecules by Schwarzschild and Kron in 1911 (see the review by Festou et al. 1993), 38 molecules, including isotopomers, have been detected in comets, most at (sub)millimeter wavelengths (Biver et al. 1997a,b). It is important to stress that the molecular abundances measured in the coma need not directly reflect the composition of the nucleus itself. First, some molecules are known to be formed in the coma, either by solar photolysis of parent molecules sublimated from the nucleus (CS, for example, Jackson et al. 1982) or via chemical reactions in the coma (HNC, Biver et al. 1997a; Irvine et al. 1998b; Rodgers & Charnley 1998; Hirota et al. 1999). Second, some molecules might be sublimated from ice- or dust-rich grains in the coma (CO, Eberhardt et al. 1987) rather than sublimating directly from the nucleus. Third, it is not yet known with what fidelity the inferred "parental" initiators of coma chemistry, whose abundances change rapidly with heliocentric distance and which are often averaged over large spatial scales, reflects the actual composition of the comet nucleus, that may itself be heterogeneous and highly structured (Bockelée-Morvan & Rickman 1997; Flammer et al. 1998). Finally,

previous millimeter observations consist mostly of single-dish studies that lack the resolution needed to map molecular emission close to the nucleus, e.g., the jet features detected by optical and near-infrared observations (see Chapter 2).

The close approach to Earth of comet C/1995 O1 (Hale-Bopp) in March and April 1997 led to major advances in our knowledge of the near nucleus molecular emissions of comets, not only due to the recently upgraded interferometric facilities at millimeter wavelengths (BIMA, Nobeyama, OVRO, Plateau de Bure) and the advent of large submillimeter telescopes equipped with sensitive heterodyne receivers and bolometer cameras (CSO, JCMT, SMT), but also the exceptionally high production rates of Hale-Bopp. The resulting intense dust and molecular line emission enabled a wide variety of high resolution imaging techniques to be brought to bear on this remarkable object.

Comet Hale-Bopp was discovered some 7.15 AU from the Sun on July 23, 1995. On March 23, 1997, the comet made its closest approach to the Earth (1.3 AU), and reached perihelion (0.91 AU) on April 1, 1997. Hale-Bopp is a very large comet, with radius estimates of order 20-25 km (see the continuum discussion in Chapter 2, and Weaver & Larmy 1997 for a review of various estimates of the size of comet Hale-Bopp, along with de Pater et al. 1998; Altenhoff et al. 1999 for an analysis of the available long wavelength thermal emission data), and is thus the most productive and dustiest comet observed to date (Schleicher et al. 1997). Many molecules have been detected in Hale-Bopp for the first time, and excellent reviews of the outgassing behavior of Hale-Bopp over the entire course of its inner orbit as determined by a combination of optical, infrared, (sub)millimeter-wave, and radio observations may be found in the Proceedings of the First International Conference on Comet Hale-Bopp (c.f. Biver et al. 1997b; Bockelée-Morvan & Rickman 1997; Weaver & Larmy 1997; Weaver et al. 1997).

Many of these observations were acquired with fairly coarse spatial or spectral resolution, and hence are incapable of examining the three-dimensional dynamics of outgassing behavior close to the nucleus. In order to test the capabilities of aperture synthesis studies of comets, $1''$-$3''$ molecular line and dust continuum observations of Hale-Bopp were carried out with the Millimeter Array of the Owens Valley Radio Observatory (OVRO) close to perihelion. An overview of the observational methods is presented in Section 2, while studies of the continuum emission are presented in Chapter 2.

High spatial and moderate spectral resolution images of 12 molecules are generated from

molecular line data acquired simultaneously with the continuum observations. In Section 3 we present and analyze the molecular observations, which often reveal arc-like structures that are offset from the nucleus (see also Blake et al. 1999). We propose that sublimation from millimeter-sized icy grains lifted by jets is responsible for the extended emission, and that the observed molecular jets may provide access to volatiles that reside deep within the nucleus. The resulting deviations from the classical Haser model are accentuated by the interferometer, and so to examine the sampling bias a Monte Carlo radiative transfer code is used to estimate the uncertainty in the production rates derived from observations that necessarily sample a limited range of angular scales compared to the full extent of cometary comae. In closing, we examine the composition of Hale-Bopp as determined by these and other millimeter-wave and infrared observations and speculate on relative roles of interstellar versus nebular processes to the chemistry of icy planetesimals in the outer solar system.

4.2 Observations

The OVRO Millimeter Array consists of six 10.4 m antennas, which for the Hale-Bopp observations were placed in a configuration containing the then maximum North-South and East-West baselines of 200 m, resulting in spatial resolutions of $1''$ at 1.3 mm and $2''$-$3''$ at 2.6-3.3 mm. Cryogenically-cooled SIS receivers on each telescope produced overall system temperatures of 500-1500 K. The digital correlator was configured to have several bands of uniform smoothed channels in a variety of spectral line setups. The spectrometer bands were centered at $V_{pla} = 0$, as defined by available ephemeri at the time of the observations (specifically, JPL orbital solution #55, D.K. Yeomans, priv. commun.). At all frequencies, simultaneous dust continuum measurements were made using an analog correlator of 1 GHz bandwidth. Dust production rates from the continuum measurements are in good agreement with those derived in the larger beams of single dish telescopes (Blake et al. 1999), which demonstrates that most of the available flux is recovered by the array on 1-$3''$ scales. The spectral resolution for the observations are typically 0.3-0.4 km/s except for CH_3CN, whose resolution is 1.6 km/s; chosen to balance the competing interests of resolving the line profiles for dynamical studies and examining the largest number of species possible during the perihelion passage of Hale-Bopp.

Calibration of visibility phases and amplitudes was achieved with snapshots of the quasars 0133+476 (for 1997 March 29-31 and 1997 April 1-2) and 0923+392 (for 1997 March 30), typically at intervals of 20 minutes. Measurements of Uranus, Neptune and 3C273 provided an absolute scale for calibration of the flux densities. The derived fluxes of 3C273 at the time of the observations were 27 Jy at 3 mm and 20 Jy at 1.3 mm. All data were phase- and amplitude-calibrated using the MMA software developed specifically for OVRO (Scoville et al. 1993). Continuum and spectral line maps were then generated and CLEANed using the NRAO AIPS package. Uncertainties in fluxes and source positions are estimated to be 20% and $0.''5$, respectively.

4.3 Molecular Line Emission

The spectral line correlator at OVRO consists of four independently addressable modules. For a given local oscillator setting, several molecules can be studied at either 3 mm or 1.3 mm, or both. In total, some 18 millimeter-wave transitions of HCN, DCN, HDO, HC_3N, HNC, HNCO, CS, H_2S, SO, OCS, CO, CH_3OH and CH_3OCH_3 in comet Hale-Bopp were detected, with upper limits available for a number of additional species. The transitions detected are presented in Table 4.1. The integrated intensities have been calculated over the velocity range for which 2σ emission is present. The dynamical and jetting activity of the comet is readily apparent in the strong spectral line emission of HCN and CS. The millimeter-wave spectral lineshapes and emission morphologies are consistent with the known rotational and jetting properties of the nucleus, and when imaged over temporal periods short compared to the rotation period provide three-dimensional snapshots of the dynamic nature of cometary activity free from the effects of scattering and obscuration commonly encountered at optical and infrared wavelengths. In the next few sections we present the molecular line data grouped into various chemical families before concluding with a discussion of the implications of the observed production rates on the origin and evolution of comets.

4.3.1 Nitrile and Isonitrile Species

Due to their strong dipole moments and simple structures, nitriles and isonitriles are among the strongest millimeter-wave emitters in the interstellar medium and comets. HCN was

Table 4.1: OVRO Molecular Lines Observations of Comet Hale-Bopp

species	trans.	freq	date,phase	Res($''$)	pk offset($''$)	vel.shift(m/s)	FWHM
HC_3N, jet	10-9	90.979	31/03/97, 0.6	2.5	7	690	2.3
HNCO, jet	4 0 4-3 0 3	87.925	31/03/97, 0.85	2.5	5-7	-340	2.1
H_2S, nuc.	2 2 0-2 1 1	216.710	30/03/97, 0.25-0.5	1-2	< 1	<300	1.6-2.3
H_2S, jet					3-5	-1300, -240	1.0,2.0
SO, jet	5 6 - 4 5	219.950	30/03/97,0.44-0.54	1-2	4-6	-500, -1000	0.8,1.0
OCS, jet	8-7	97.301	30/03/97, 0.55	5	7	-1300	1.0
CS, nuc	2-1	97.981	30/03/97, 0.3-0.9	3	< 0.5	270	1.6
	5-4	244.936	1,2/04/97, 0.6-0.9	1-2	2-3	<100	1.9
CO, nuc.	1-0	115.3	01/04/97, 0.86	2	< 0.5	530	1.5
CO, jet					6-7	540	0.8
CH_3OH, nuc.	5-4	241.767	29/03/97 &	1-2	< 2	<100	2.3
		241.791	01/04/97				
CH_3OCH_3, nuc.	7 0 6 - 6 1 6	111.783	01/04/97, 0.6-1.0	2	<2	300	1.5

first detected in comet Kohoutek (Huebner et al. 1974), and has been seen in a variety of long period comets since. HNC is a metastable isomer of HCN, and is found in negligible amounts in equilibrium models of the solar nebula. Its detection in comets is thus an important indicator of kinetically-controlled processes, that is chemistry which is driven by the rates of various reactions and not by thermodynamics. Ion-molecule networks in dense molecular clouds (Schilke et al. 1992; van Dishoeck & Blake 1995; Irvine et al. 2000) lead to (HNC/HCN) ratios of $\sim$0.2-1, while in T Tauri star accretion disk analogs of the solar nebula values near 0.4 are seen (Dutrey et al. 1997). In certain chemical kinetic models of these disks, the high HNC abundances are produced by photochemistry, while in others they arise from surviving molecular cloud material (Willacy et al. 1998). HNC can also be synthesized within the coma (Rodgers & Charnley 1998), and the radial dependence of the (HNC/HCN) ratio in comets should be a sensitive function of direct HNC outgassing versus *in situ* production (Irvine et al. 1998a).

The J = 1 $\rightarrow$ 0 rotational transition of HCN at 88.6 GHz was detected on 1997 March 29 and 31. At the time of these near-perihelion observations, the heliocentric and geocentric distances of Hale-Bopp were 0.915/0.914 and 1.338/1.334 astronomical units (AU), respectively. HCN was observed from UT 00:16:30 to UT 01:03:48 on March 29 and from UT 00:17:14 to UT 01:01:00 on March 31. Due to the favorable northern declination of comet Hale-Bopp, good synthesized beams with minimal sidelobes could be obtained over averaging times of only 2-3 hours. HCN results are presented in Figures 4.1 and 4.2, where the images from March 29 and 31 are ordered according to the rotational phase of the

nucleus, as adopted from Licandro et al. (1998), hereafter JL98. It is computed as the fractional part of the time, in hours, since or before 1997 April 1.0 UT, divided by 11.35, the rotational period of Hale-Bopp fitted by these authors. The JL98 results are for several days after the HCN OVRO observations, but it is safe to infer the phases in this manner for previous days since the rotation period is found to be very stable near perihelion. The line flux is integrated over the velocity range for which HCN emission appeared above the 2σ level of $\sim$80 mJy beam^{-1} in channel maps with a velocity width of 0.42 km/s. Intense HCN emission centered on the nucleus, whose position is determined by the dust continuum observations acquired at the same time, is observed; as are two jet-like structures (which, like JL98, we label A and B on the maps) that are clearly visible to the southwest around phase 0.5-0.7 and to the southeast around phase 0.24-0.5 and 0.7-0.96.

We consider first the observations of March 29 (Figure 4.1) since these have the longest observed time range. The OVRO observations begin at a rotational phase of 0.24, where, from the JL98 near-infrared observations, jet A is well evolved and jet B just begins to appear. In the HCN images, a molecular counterpart to jet B grows in intensity from phase 0.24 to phase 0.33, and jet A has rotated toward the southwest side of the nucleus from phase 0.41 to 0.59. From JL98, jet A reappears to the southeast around phase 0.7. From phase 0.68 to 0.96, a weak HCN feature does in fact appear in the March 29 HCN maps. The same two jet features are seen again in the 1997 March 31 images presented in Figure 4.2 for which the signal-to-noise is improved but the time range is more restrictive than that on March 29.

The kinematic and morphological patterns in the HCN images are consistent with optical and near-infrared observations of the jetting behavior of Comet Hale-Bopp during perihelion. In particular, the counterclockwise rotation of the jets indicates that the north pole of the nucleus was oriented toward the Earth in 1997 April. The pole position reported by JL98 is R.A.=275° and DEC.=-50°, which results in an aspect angle (defined as the angle subtended by the comet spin axis to the line of sight) near 45 degrees and a position angle of the spin axis on the sky (measured counterclockwise from north) of approximately 240 degrees, both of which are largely invariant during March/April 1997. The images of jets A and B in Figure 4.2 clearly showed the main emission to the position angle of southeast and southwest, which are consistent with spin position angles of 180 - 270 degrees and a significant aspect angle, in accord with JL98.

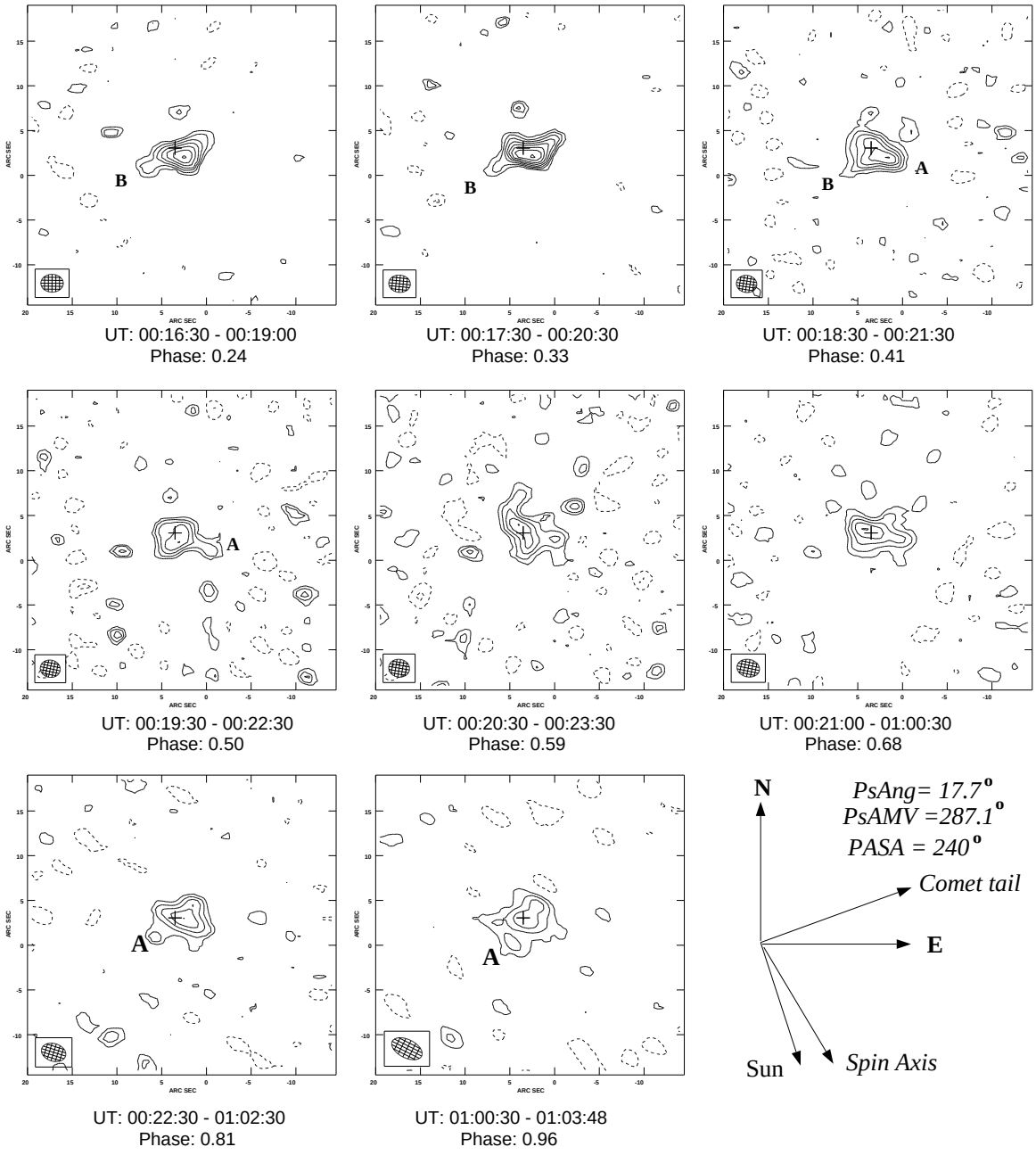

Figure 4.1: HCN emission from comet Hale-Bopp on 1997 March 29. Time intervals between the three hour averaged panels are one hour.

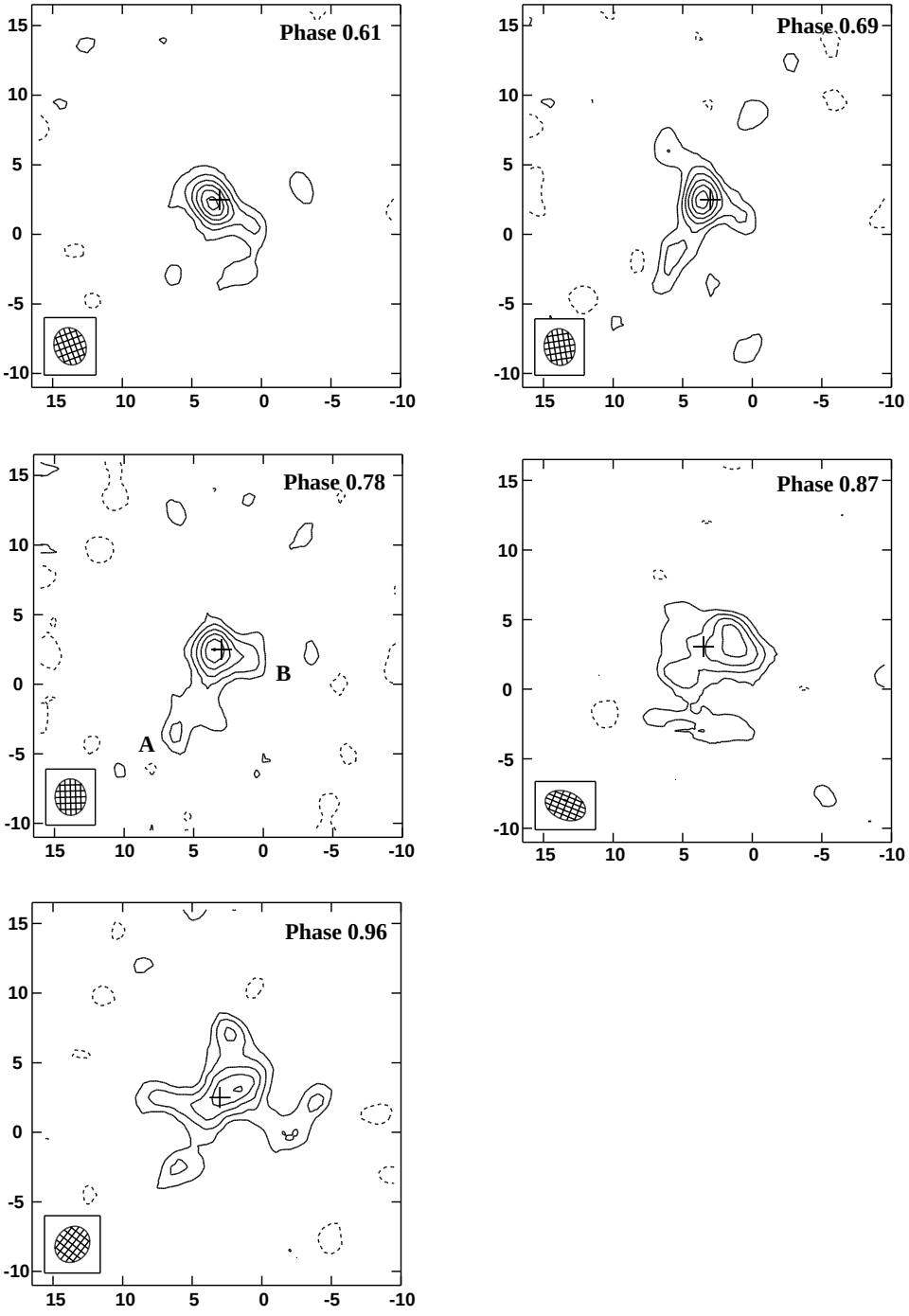

Figure 4.2: HCN emission from comet Hale-Bopp on 1997 March 31.

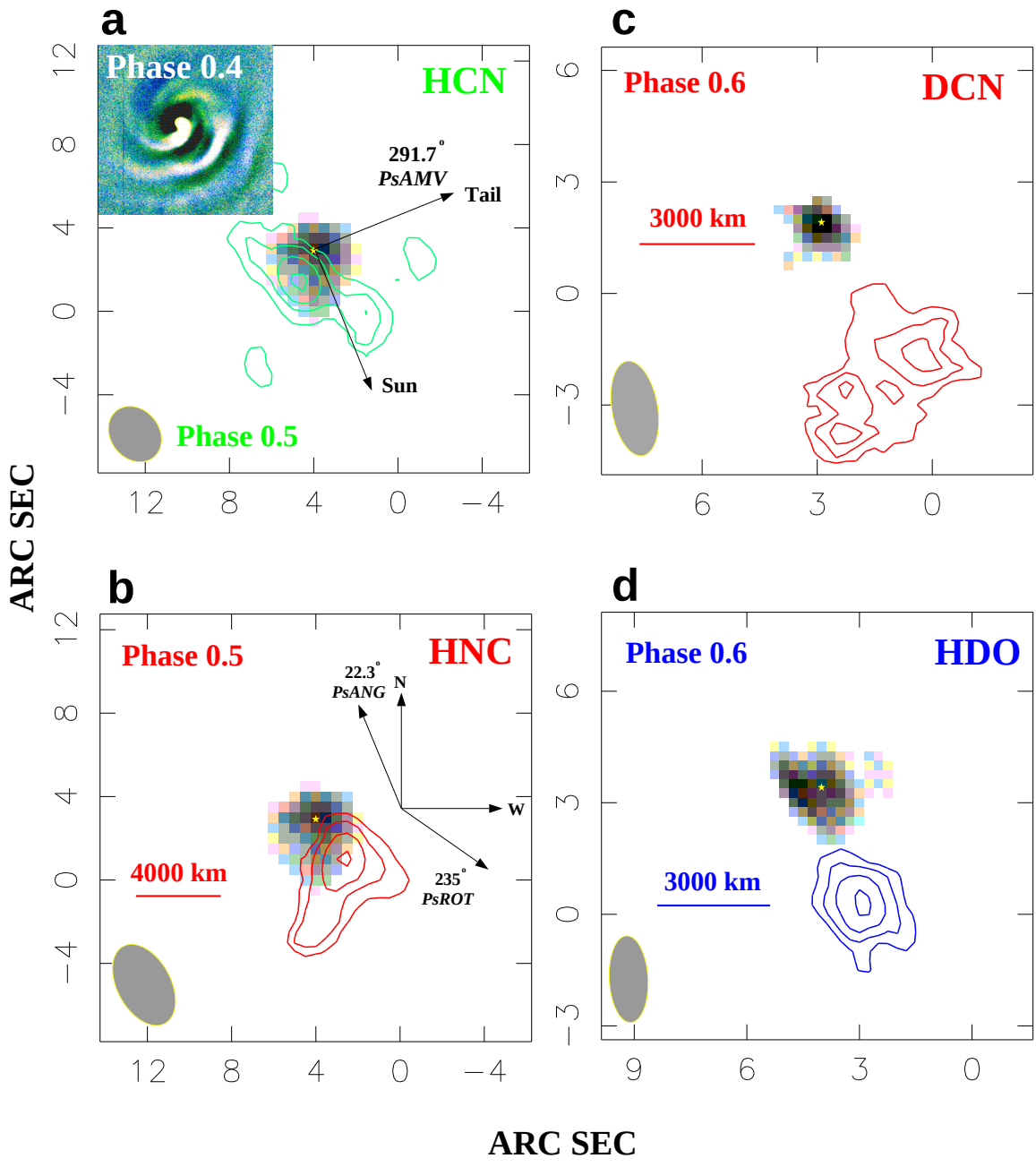

Figure 4.3: Contour maps of millimeter-wave rotational line emission from HCN, HNC, DCN and HDO in the coma of comet Hale-Bopp. The grey scale presents simultaneous continuum images, the peak of which is marked by the star.

Analogous features are observed in HNC, which was observed simultaneously with HCN on March 31. As panels **a** and **b** of Figure 4.3 show, however, while extended HCN and HNC features are detected at position angles similar to those of the dust jets (PA$\sim$230° in Figure 4.3), over certain time ranges they are strongly anti-correlated in a radial sense. Clearly, production rate estimates for species such as these must consider outgassing both from the nucleus and from more extended sources such as jets. For molecules such as HCN and HNC whose collisional cross sections are known, we use both LTE, with T_{ROT}=115 K (Biver et al. 1997a), and statistical equilibrium (SE) Monte Carlo codes to examine nucleus versus extended source sublimation. For collisional rates in the SE model, the "interstellar" cross sections for collisions with H_2 molecules (Green et al. 1993) are scaled to reproduce the total "cometary" cross sections recommended by Crovisier (1987) and Meier et al. (1998a). Use of the H_2 cross sections themselves (which are roughly an order of magnitude smaller) only changes the production rates by $\lesssim$ 10% since the levels observed are nearly in LTE.

Beam averaged column densities are calculated from the measured line intensities, and are summarized for all the transitions observed at OVRO in Table 4.2. In the SE model, a Monte Carlo approach is used to solve the line radiative transfer (Hogerheijde & van der Tak 2000) within a one-dimensional Haser coma model at a total water production rate of 10^{31} mol s^{-1}. The model is sampled at the observational (u, v)-spacings, and the abundances varied until agreement with the interferometric data is obtained. Accordingly, the effects of the varying spatial resolutions at λ=3.3 and 1.4 mm and the finite array sampling of extended structures are rigorously accounted for. Densities in the inner coma are sufficiently high that departures from LTE are found to be small (Biver et al. 1997a; Meier et al. 1998b), while the SE models show that all of the transitions studied here are optically thin.

For HCN, the observed hyperfine ratios of the $1 \rightarrow 0$ transition are also consistent with low optical depths, as is true in larger beams (Irvine et al. 1998a). Due to the large size of the coma and the coarse (u, v)-sampling of the present data sets, only 15-20% of the total flux within 45-60″ beams is detected. Haser model fits with a single HCN production rate do reproduce the OVRO $1 \rightarrow 0$, Quabbin $1 \rightarrow 0$, and JCMT $4 \rightarrow 3$ intensities near perihelion (Irvine et al. 1998a,b), however, and demonstrate that *the appropriate fluxes are recovered by the array even for sources which extend well beyond the primary beam of the six 10.4 m antennae*. From images such as those in Figure 4.3a, we estimate that at most 20-25% of

Table 4.2: Comet Hale-Bopp: LTE Molecular Column Densities from OVRO Data

species	beam	I (K km/s)	N_{LTE} mol(cm^{-3})	Q_{LTE}
HCN, nuc.(29)	2.5x2.0	21.5	4.15(14)	9.93(27)
HCN, jet (29)		5.68	1.08(14)	2.58(27)
HCN, nuc.(31)	2.7x2.3	16.4	3.17(14)	8.65(27)
HCN, jet (31)		7.07	1.37(14)	9.80(26)
HNC, nuc	2.5x2.4	10.3	1.02(14)	2.73(27)
HNC, jet		8.22	8.17(13)	2.19(27)
HNCO, (nuc.)	2.3x1.2	<4.2	<4.6(14)	<8.5(27)
HNCO, jet		16.9	1.88(15)	3.44(28)
HC_3N, (nuc.)	2.6x2.3	<2.7	<2.2(13)	<5.8(26)
HC_3N, jet		10.4	8.25(13)	2.21(27)
DCN, (nuc.)	2.3x1.2	<3.8	<8.2(12)	<1.5(25)
DCN, jet		12.8	2.71(13)	4.87(26)
HDO, (nuc.)	2.1x1.0	<1.7	<2.4(14)	<3.7(27)
HDO, jet		7.77	1.23(15)	1.0(28)
CS, nuc.(30)	2.7x2.1	21.6	4.53(14)	1.10(28)
CS, nuc.(01)	2.7x1.0	20.4	9.01(13)	1.65(27)
CS, nuc.(02)	2.1x1.0	22.9	1.01(14)	1.64(27)
H_2S, nuc.	2.6x1.1	7.3-16.8	0.7-1.5(15)	1.2-2.2(28)
H_2S, jet		5.6-13.2	0.5-1.2(15)	0.9-2.2(28)
SO, (nuc.)	2.5x1.1	<3.1	<6.5(13)	<1.2(27)
SO, jet		11.04	2.31(14)	2.70(27)
OCS, (nuc.)	5.1x1.9	<0.7	<1.2(14)	<4.2(27)
OCS, jet		2.32	4.26(14)	1.03(28)
CO, nuc.	2.1x1.7	31.94	1.53(17)	3.18(30)
CO, jet		10.94	5.23(16)	3.52(29)
CH_3OH,nuc.(29)	2.4x1.0	15.54	5.51(15)	9.30(28)
CH_3OH,nuc.(01)	2.6x1.2	16.64	5.30(15)	1.03(29)
CH_3CH_3, nuc.	2.3x1.8	9.72	9.40(15)	2.0(29)

the total HCN 1→0 emission within 5″ of the nucleus arises in jet-like structures. When the extended coma emission and finite array (u, v)-sampling is accounted for theoretically this fraction drops to ∼15%, and so the Haser model is indeed a good first approximation.

For the other species, the observed anisotropy (Figure 4.3b,c,d) renders spherically symmetric derivations of the production rates inappropriate. To account for this anisotropy, estimates of the jet solid angle filling factors are needed. Here, the column densities in Table 4.2 have been scaled according to $Q_{jet}(X) = Q_{Haser} \times \Delta v_X / \Delta v_{nucleus}$, where Δv_X is the measured velocity width of species X at the jet position, and $\Delta v_{nucleus}$ is the measured velocity width of HCN emission at the nucleus; an admittedly simplistic approach, but one which should result in upper bounds to the jet production rates.

Numerically, on March 29 the HCN production rate from the nucleus is estimated to be 1×10^{28} mol s^{-1} using the LTE model, and 2×10^{28} mol s^{-1} with the SE model that explicitly accounts for the array sampling bias. Jet production rates are found to be 2.6×10^{27} mol s^{-1} (LTE) and 3.5×10^{27} mol s^{-1} (SE). The total production rate is thus 2.4×10^{28} mol s^{-1}, in excellent agreement with that measured with single dishes (Biver et al. 1997b) and with a 10″ beam using the BIMA array (Wright et al. 1998). In contrast, the calculated HNC abundances with the LTE model are 2.7×10^{27} mol s^{-1} and and (nucleus) and 2.2×10^{27} mol s^{-1} (jet), whose sum matches well that derived from large beam observations. The factor of three radial variation seen in the (HNC/HCN) column density ratios over a few thousand km within the HNC arc and the HNC production rates in small beams are difficult to reconcile with purely coma chemistry synthesis (Irvine et al. 1998a,b; Rodgers & Charnley 1998), and suggest that some HNC is intrinsic to cometary ices.

The $4_{04} \rightarrow 3_{03}$ and $10 \rightarrow 9$ transitions of the more complex HNCO and HC_3N (iso)nitriles were also observed on 1997 March 31 using the same HCN/HNC local oscillator setting. Figure 4.4 shows the maps of HCN, HNC and HC_3N observed between 17:00-22:00 UT (that is, a rotational phase of ∼0.6). The jet features extend to 7″ (7000 km) away from the nucleus. The HC_3N emission is detected at position angles similar to those of the extended HCN and HNC features in the 2.″55 × 2.″3 beam. Interestingly, the HNC and HNCO spectra are red-shifted, and the velocities shifted increase with the distance from the nucleus: HNC lies 1-5″ away from the continuum source with a 170 m/s red-shift, and HC_3N is 7″ offset with a 700 m/s Doppler red-shift. The HCN spectrum from a box centered on the jet has almost no velocity shift. The full width half maximum (FWHM) of the HNC

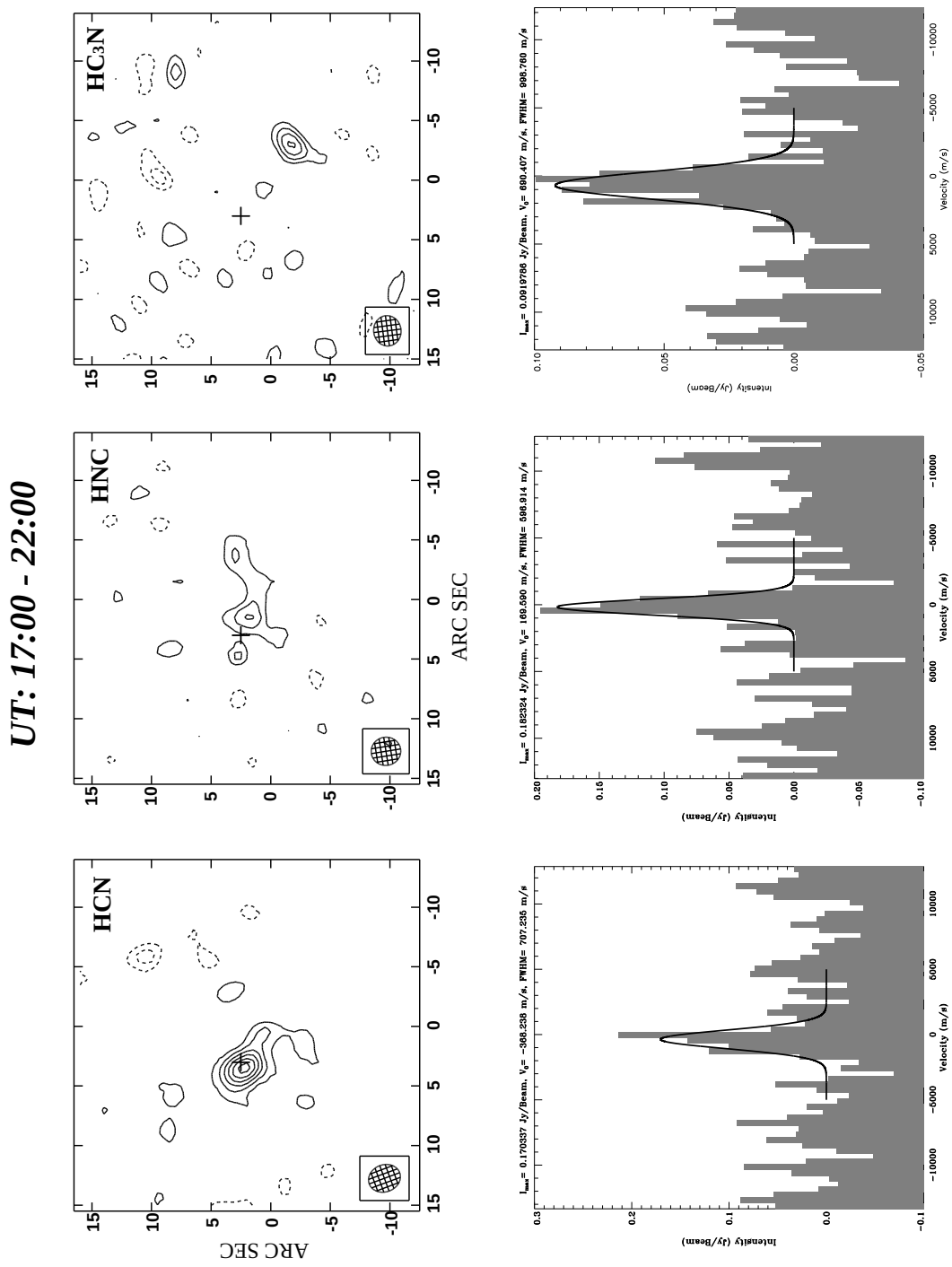

Figure 4.4: OVRO maps of the emission from HCN, HNC, and HC_3N on 1997 March 31. In this figure and those which follow, the spectra beneath the maps are averaged over a box the size of the synthesized beam at the peak of the observed emission. See Blake et al. 1999 for details.

$1 \rightarrow 0$ spectrum is about half of those for HCN and HC_3N. The HC_3N $10 \rightarrow 9$ transition has three hyperfine components centered at 90.979 GHz, but we have insufficient spectral resolution to differentiate them. The entire emission profile is therefore integrated across the velocity range from -0.5 to 2 km/s in which emission is detected at the 2σ level. The integrated intensity is 7.0 K km/s, resulting in an LTE column density of 5.72×10^{13} cm^{-2} for a rotational temperature of 104 K (Bird et al. 1997). The production rate is 2.2×10^{27} s^{-1}, which is in good agreement with the single-dish measurement of 2×10^{27} s^{-1}.

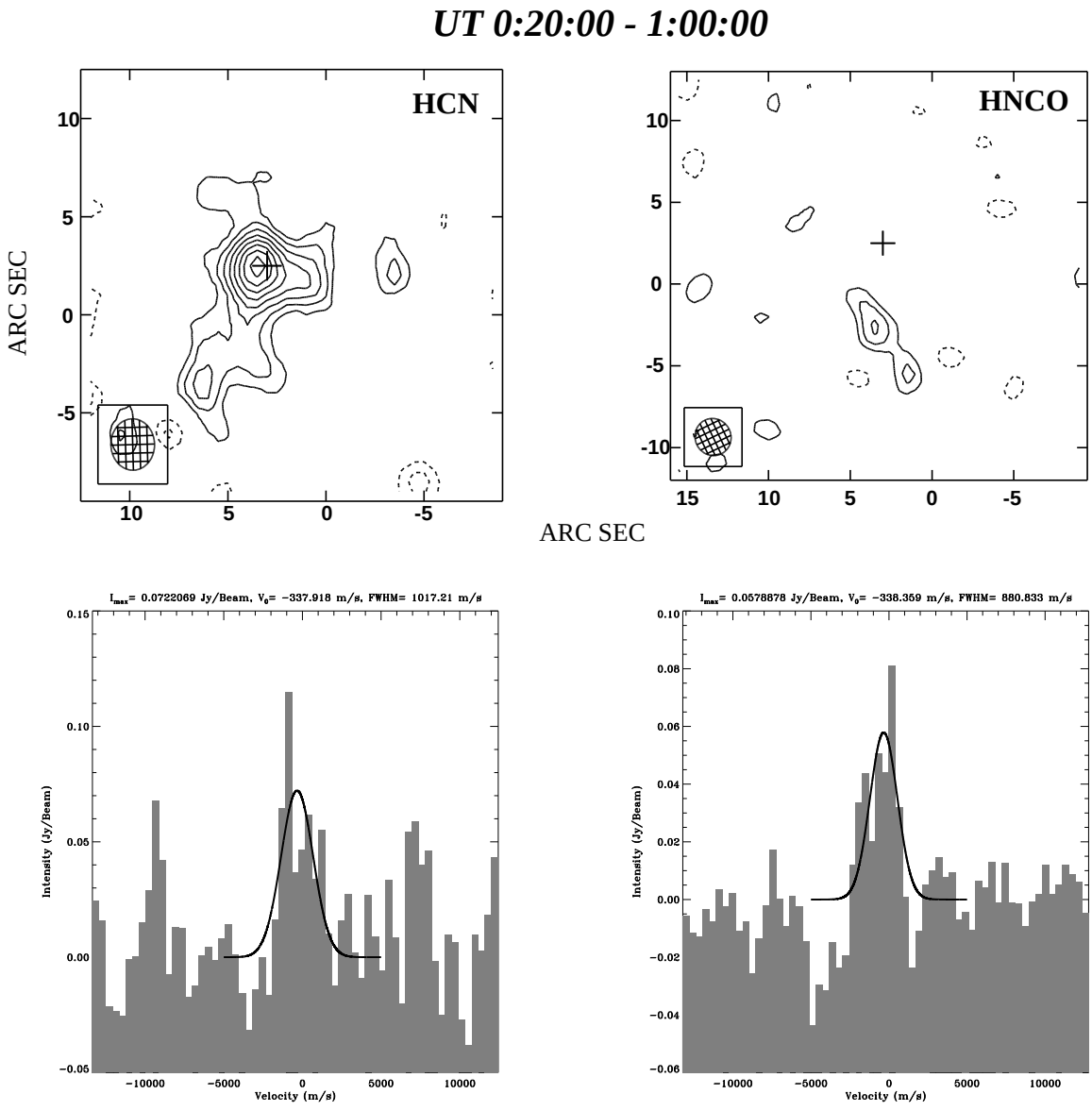

Figure 4.5: Maps of the emission from HCN and HNCO on 1997 March 31.

The strongest emission from the HNCO $4_{04} \rightarrow 3_{03}$ transition is seen between 19:00-23:00 UT opn March 31. The synthesized beam size is $2.''3 \times 2.''2$. Again, the HNCO emission is detected some 5-7$''$ away from the millimeter-wave continuum source. The offset is consistent with the HCN weak arc features observed during the same period (see Figure 4.5). Both lines show the velocity blue-shifts of up to 340 m/s, with FWHM around 2.2 km/s. The three main hyperfine components of the 87.9253 GHz 4_{04}-3_{03} transition and the integrated intensity of 3.94 K km/s correspond to a production rate of 3.4×10^{28} s^{-1}, rather larger than the single-dish measurement of $7 - 9 \times 10^{27}$ s^{-1}. The larger HNCO production rates derived by OVRO may be associated with the small source size observed, which would lead to an underestimate of the true brightness temperature in single dish studies due to beam dilution.

Only upper limits have been obtained for the production rates of CH_3CN and C_2H_5CN. The CH_3CN 5_K-4_K stack was observed on 1997 March 29, reaching a noise level of 52 mJy/beam in 1.6 km/s velocity channels. Weak detections in the single dish observing campaigns lead to an estimated CH_3CN production rate of 2×10^{27} s^{-1}, roughly a factor of three below our upper limit of 5.5×10^{27} s^{-1}. Limits to the C_2H_5CN $10_{0,10} \rightarrow 9_{0,9}$ emission on 1997 March 31 reached a noise level of 93 mJy/beam in 0.4 km/s velocity channels, resulting in an upper limit to the C_2H_5CN production rate of $1.2 \times 10^{28} s^{-1}$. To the best of our knowledge, there has been no detection of C_2H_5CN reported from single-dish measurements.

4.3.2 D/H Ratios in Hale-Bopp

(D/H) ratios are thought to provide among the most sensitive diagnostics of cometary origins. In dense clouds, trace species exhibit orders of magnitude and highly variable (D/H) enrichments that are both molecule specific and temperature sensitive. The typical interstellar values are much larger than those expected for volatiles synthesized in protoplanetary regions of the solar nebula, but comparable to those found in the outermost regions of circumstellar accretion disks. For example, (D/H) ratios of 0.01-0.05 are common in molecular cloud organics (Wootten 1987), while values of up to 0.18 have been detected toward low-mass protostars (van Dishoeck et al. 1995). (HDO/H_2O) ratios are difficult to measure in cold regions, but lower bounds are provided by the values seen in hot cores (2-6 $\times$ 10^{-4}, Jacq et al. 1990). These minimum HDO enhancements are still ten times the estimated

protosolar deuterium fraction of $(D/H)_{proto} \sim 3 \times 10^{-5}$ (Gautier & Morel 1997), and are similar to the water (D/H) values measured in Halley, Hyakutake, and Hale-Bopp (3.1, 2.9, 3.3×10^{-4}; Eberhardt et al. 1995; Bockelée-Morvan et al. 1998; Meier et al. 1998b).

Studies of the molecular (D/H) variability may therefore provide clues as to the interstellar versus nebular contributions to cometary nuclei. Deuterated species are quite difficult to detect in the optical and infrared regions of the electromagnetic spectrum, and so (sub)millimeter-wave aperture synthesis images provide the best route to understanding the potential contributions of nucleus versus extended source sublimation and coma chemistry to the (D/H) ratios measured in large beams. In accord with measurements toward dark clouds and with that expected for the kinetically-controlled chemistry in the outer reaches of circumstellar accretion disks, the Hale-Bopp (D/H) value measured in organics such as HCN is nearly a factor of ten larger than that measured for water (Meier et al. 1998a,b). Both molecules are clearly dominated by sublimation from the nucleus, but, as panels *c* and *d* of Figure 4.3 reveal, the DCN and HDO emission detected by OVRO (DCN and HDO) is clearly offset from the millimeter-wave continuum position. These images were generated from visibilities collected on March 30 and 29 at the frequencies of the DCN $3 \rightarrow 2$ and HDO $2_{11} \rightarrow 2_{12}$ transitions at 217.2383 and 241.5615 GHz, respectively, and at rotational phases similar to those for HCN and HNC ($\sim$0.5-0.6). DCN $3 \rightarrow 2$ images and spectra at three different rotational phases on March 30 are presented in Figure 4.6. Maps in two rotational phases can be compared with the optical image of dust jets in the coma of Hale-Bopp (Figure 4.7, see Blake et al. 1999 for details). An examination of the available millimeter-wave spectral line databases reveals no other likely cometary molecule candidates that could contribute to line emission at the frequency of the DCN and HDO transitions.

The DCN and HDO position angles and the rotational sense and velocity trends of the DCN arcs are again consistent with the known jetting properties of Hale-Bopp. While we do not have simultaneous HCN and DCN observations, the HCN column densities on March 31 are in excellent agreement with Quabbin 1-0 single dish maps on March 30 (A.J. Lowell, private communication). Using the March 31 HCN fluxes at similar rotational phases, the (DCN/HCN) production rate ratios vary by factors of at least two but are always quite large, $(D/H)_{HCN,jet} \lesssim 0.025$, and are approximately a factor of ten higher than the value of 2.3×10^{-3} found by JCMT observations of the DCN 5-4 transition (Meier et al. 1998a).

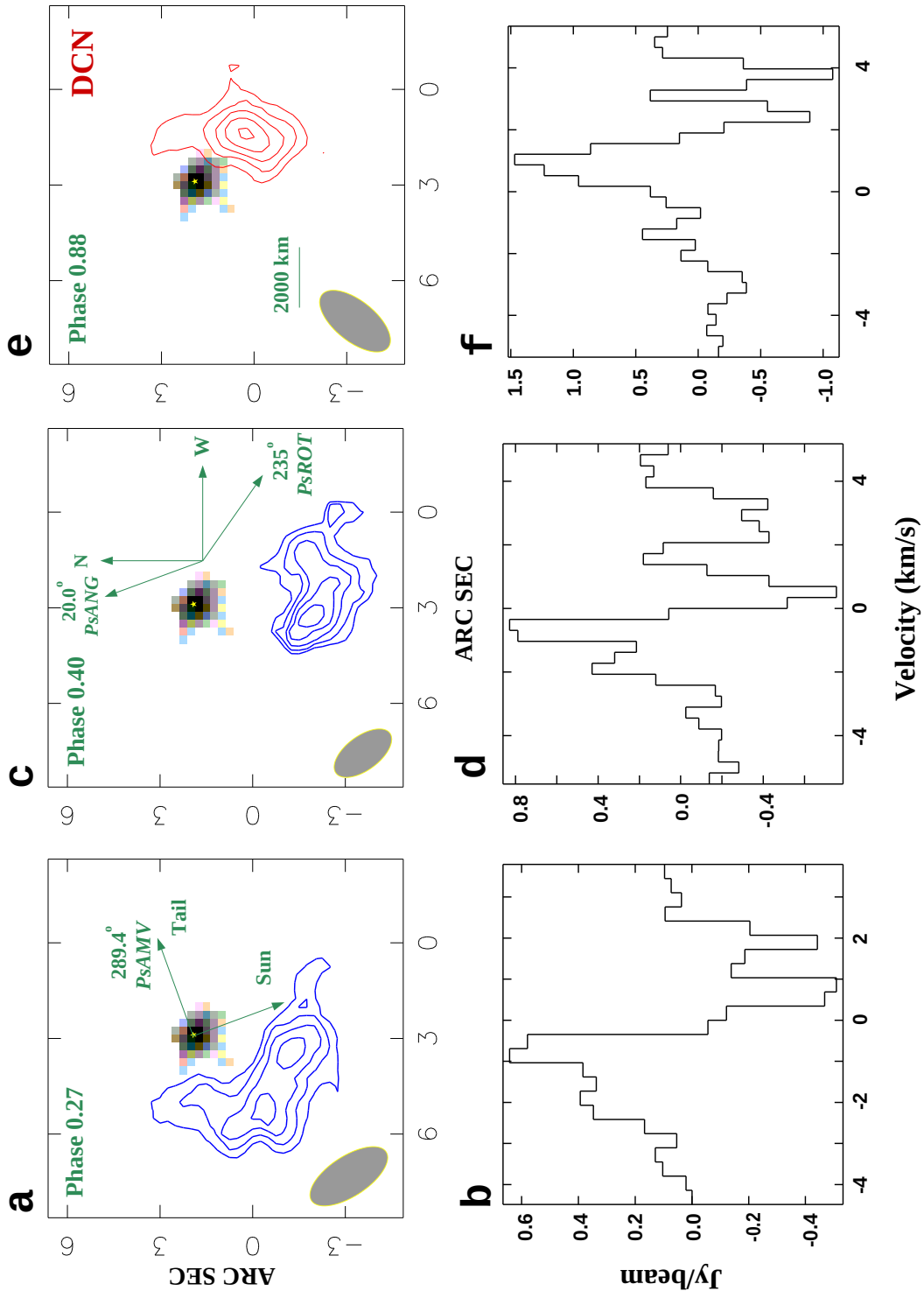

Figure 4.6: DCN maps and spectra from comet Hale-Bopp on 1997 March 30. The synthesized beam is depicted at the lower left of each image.

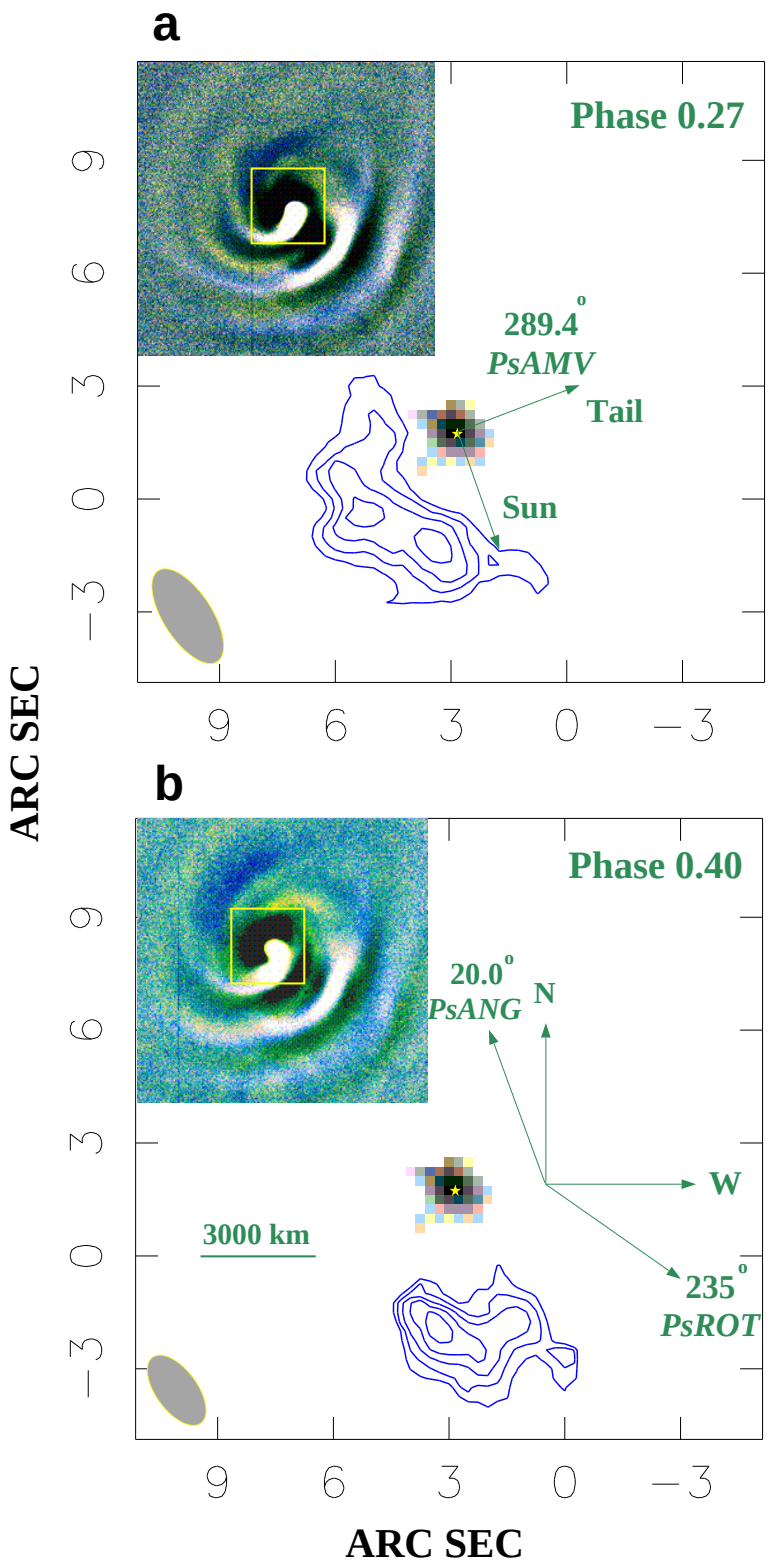

Figure 4.7: DCN maps from comet Hale-Bopp on 1997 March 30. The synthesized beam is depicted at the lower left of each image. The insert presents optical images of dust jets in the coma of Hale-Bopp taken around the same time. See Blake et al. 1999 for details.

Ratios with the March 29 HCN data are even larger, as are the direct ratios of the observed column densities.

Absorption by atmospheric water vapor makes direct measurements of the (HDO/H_2O) ratio impractical, but the OVRO fluxes and the large scale water outgassing (as traced by OH) of 10^{31} sec^{-1} yield a *lower bound* of $(D/H)_{H_2O,jet} \geq 7.5 \times 10^{-4}$. To estimate the jet (D/H) ratios we use the simultaneously observed HCN emission as a proxy. Provided the (HCN/H_2O) ratio in the jets is similar to the value of 0.002 observed in single dish beams (Biver et al. 1997a; Bockelée-Morvan & Rickman 1997), the observed interferometric (HDO/HCN) production rate ratios can be scaled to yield (HDO/H_2O) production rate ratios. The result is $(D/H)_{H_2O,jet}$ estimates of 1.5-2.5 $\times 10^{-3}$. This latter value is again nearly an order of magnitude larger than that found in the 10.″5 beam of the JCMT (Meier et al. 1998a), and over twenty times the (D/H) ratio of the earth's oceans. Clearly, contributions to the water production rate on scales large compared to those sampled interferometrically are not accounted for, and so this ratio should not be compared directly to those measured in larger beams.

4.3.3 Sulfur Species

All sulfur species were observed on 1997 March 30, except for the CS $5 \rightarrow 4$ transition that was observed on 1997 April 1-2. Velocity integrated H_2S 2_{20}-2_{11} and DCN 3-2 maps averaged every 3-4 hours between March 30 15:30-21:30 UT are shown in Figure 4.8. The maps of the H_2S $2_{20} \rightarrow 2_{11}$ line show both a peak near the nucleus as well as arcs that rotate about it, similar to features observed in both the HCN and DCN maps. The beams in the H_2S maps are 1.″3 $\times$ 0.″9, 2.″5 $\times$ 1.″0, and 2.″6 $\times$ 1.″1 respectively, while the integrated intensities are 14.8, 9.7, 7.9 K km/s at the nucleus and 3.7, 3.5, 2.8 K km/s on the jet. The FWHM of the H_2S spectra are 1.6 km/s for emission centered on the nucleus, and some 1.0-1.6 km/s for the extended features. The FWHM of DCN emission, obtained at the same time, is 0.7-1.0 km/s, and so it is unlikely that H_2S and DCN share the same origin.

The LTE production rates for nucleus sublimation are 1.2-2.2$\times 10^{28}$ s^{-1}, and 0.9-2.2$\times 10^{28}$ s^{-1} for the jet(s). The nucleus production rates are fairly consistent between the 3 plots, but those for the extended features change by a factor of 2. The sum of the production rates yield total values of 2.2-4$\times 10^{28}$ s^{-1}, nearly a factor of four smaller than the single dish value of 1.5$\times 10^{29}$ s^{-1} (Bockelée-Morvan et al. 2000). This large difference cannot be accounted

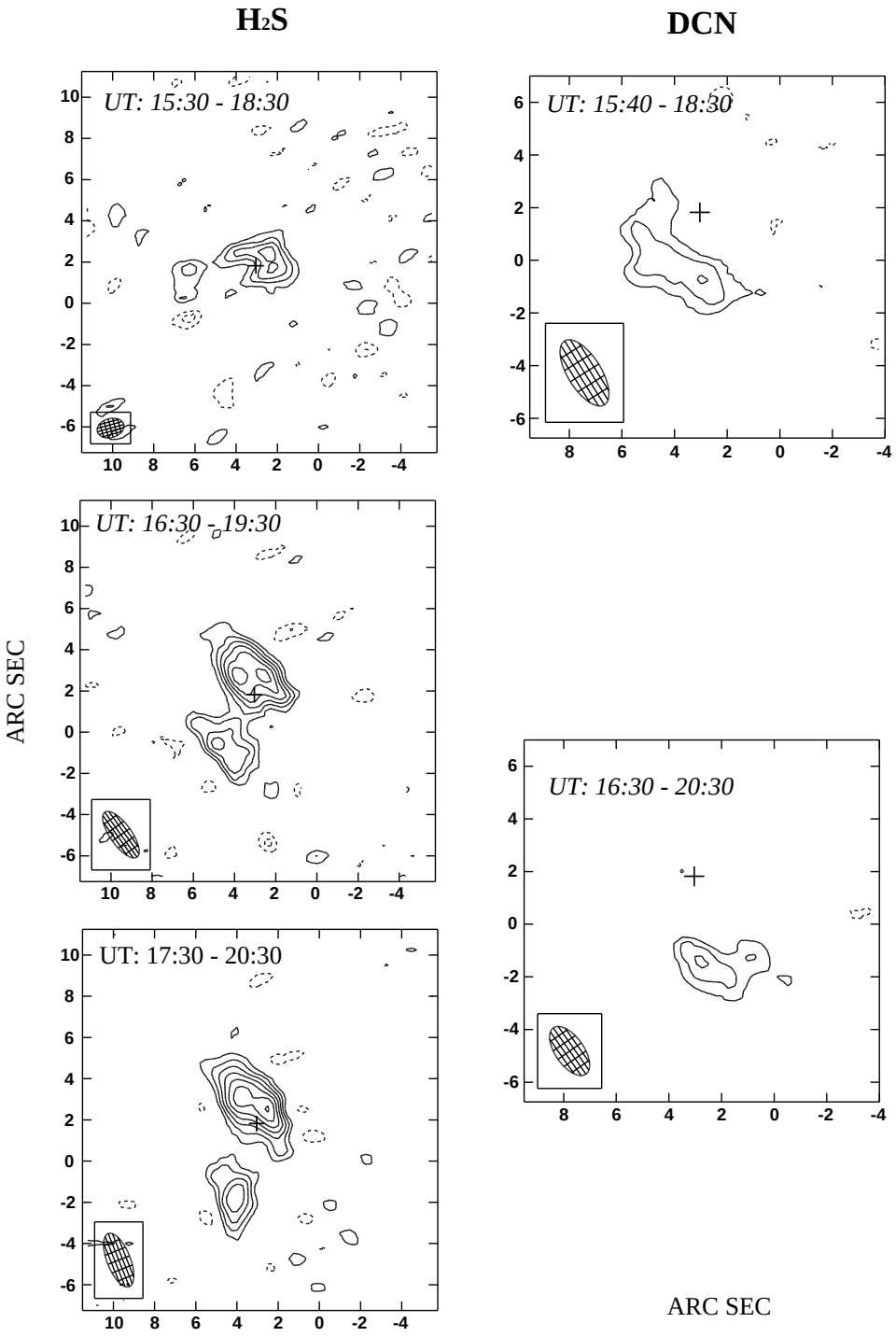

Figure 4.8: OVRO images of the H_2S emission from comet Hale-Bopp on 1997 March 30. DCN images from the same temporal interval are included to illustrate the location of the dust/gas jets.

for by simply invoking extended emission consistent with the Haser model, it is most likely due to an extended production source in the coma. H_2S is difficult to synthesize by *in situ* chemistry but is quite volatile even when mixed with water, and so likely arises from an extended dust source to which the interferometry is insensitive.

Five hour averaged maps of SO $5_6 \rightarrow 4_5$ data taken between 16:30-22:30 UT on 1997 March 30 with beam sizes of $2.''4 \times 1.''1$ and $2.''5 \times 1.''1$, are shown with the maps of H_2S obtained over the same interval in Figure 4.9. The SO emission is quite intense, well offset from the nucleus, and red-shifted by ~0.5-1 km/s over this interval (as is DCN). The integrated intensities are 3.38 and 7.26 K km/s, respectively, and change by factors similar to those observed for the extended H_2S features. The FWHM of SO is 0.8-1.0 km/s, and the corresponding production rates range from 1.4×10^{27} s^{-1} to 2.7×10^{27} s^{-1}. SO is thought to be the photolysis product of SO_2, which has a photodissociation rate of 2.1 -2.5×10^{-4} s^{-1} for a bare molecule a distance of 1 AU from the quiet Sun (Crovisier 1987). With a 1 km/s outflow velocity, this would place the inner edge of the SO emission at ~4000-5000 km distance from the continuum position, should the SO_2 be directly sublimated from the nucleus. The offset of SO detected here is quite consistent with this estimate. Interestingly, the SO emission is not concentrated along the anti-solar SW direction as is CS, another known photolysis product to be discussed at greater length below. The production rate of SO is also more than a factor of ten below that calculated from single dish measurements ($4.\times10^{28}$ s^{-1}). Like the H_2S measurements, this likely indicates that SO or its parent has a substantial extended dust or *in situ* chemistry source that is not detected at the 1-3$''$ resolution employed at OVRO.

The OCS $8 \rightarrow 7$ transition was marginally detected ($\sim3\sigma$) on March 30 between 17:30-21:30UT. The OCS emission peak lies some 7$''$ away from the continuum source and the velocity is blue-shifted to 1.33 km/s – similar to the weak jet features seen in H_2S and SO, but some 1-2$''$ further away from the nucleus (Figure 4.10). The FWHM of OCS line is also very narrow, only 420 m/s. For an LTE Haser model, the production rate of OCS is 1.1×10^{28} s^{-1}. If a solid angle correction is made based on the observed line widths, the production rate rises to ~$3.\times10^{28}$ s^{-1}, which is smaller than but comparable to that inferred by single dish measurements ($4.\times10^{28}$ s^{-1}). Detection of OCS by long-slit spectroscopy at the NASA InfraRed Telescope Facility (IRTF) on Mauna Kea, Hawaii, reveals a strong spatial correlation of OCS with dust, and suggests that the majority of OCS is released in

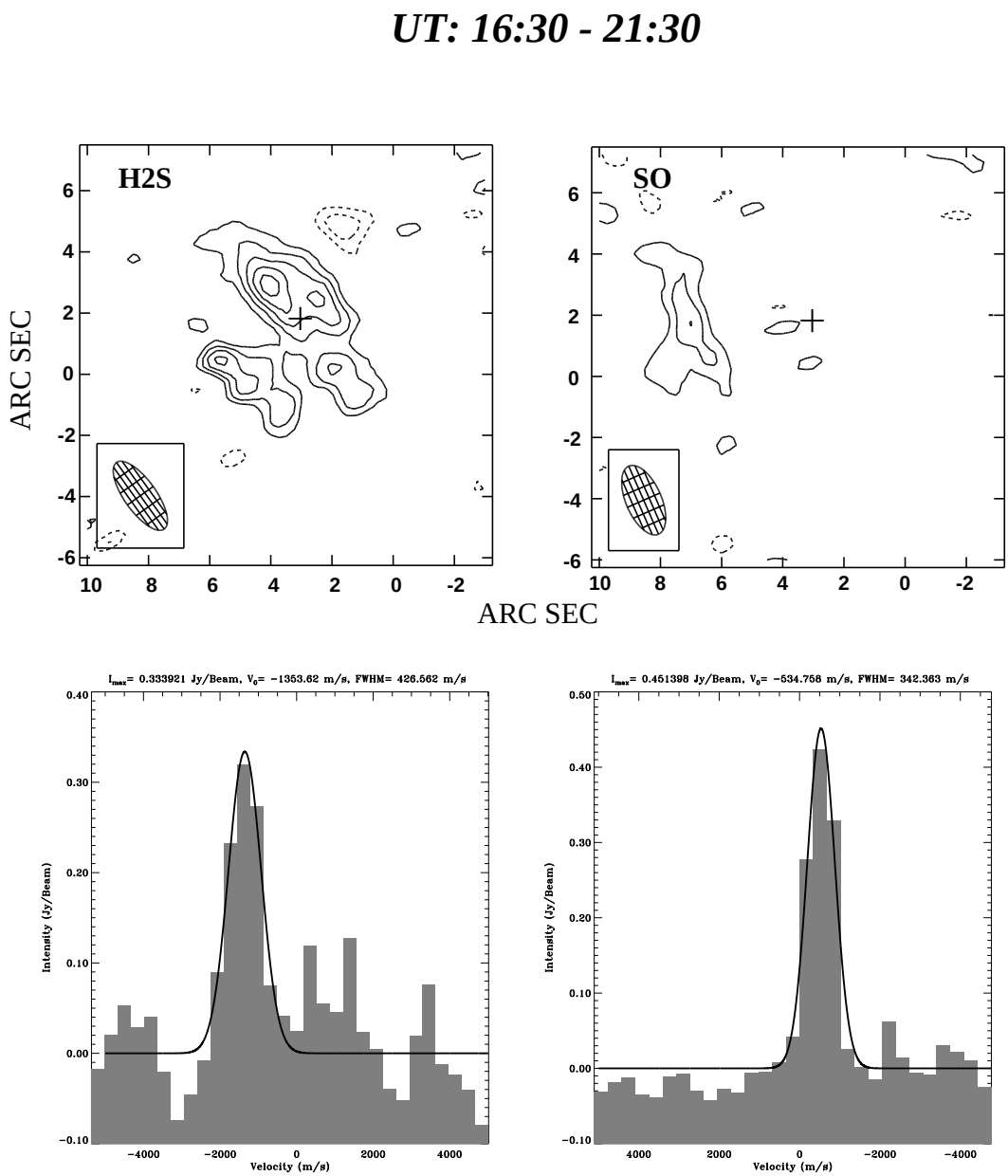

Figure 4.9: OVRO observations of sulfur-containing molecules in the coma of comet Hale-Bopp on 1997 March 30.

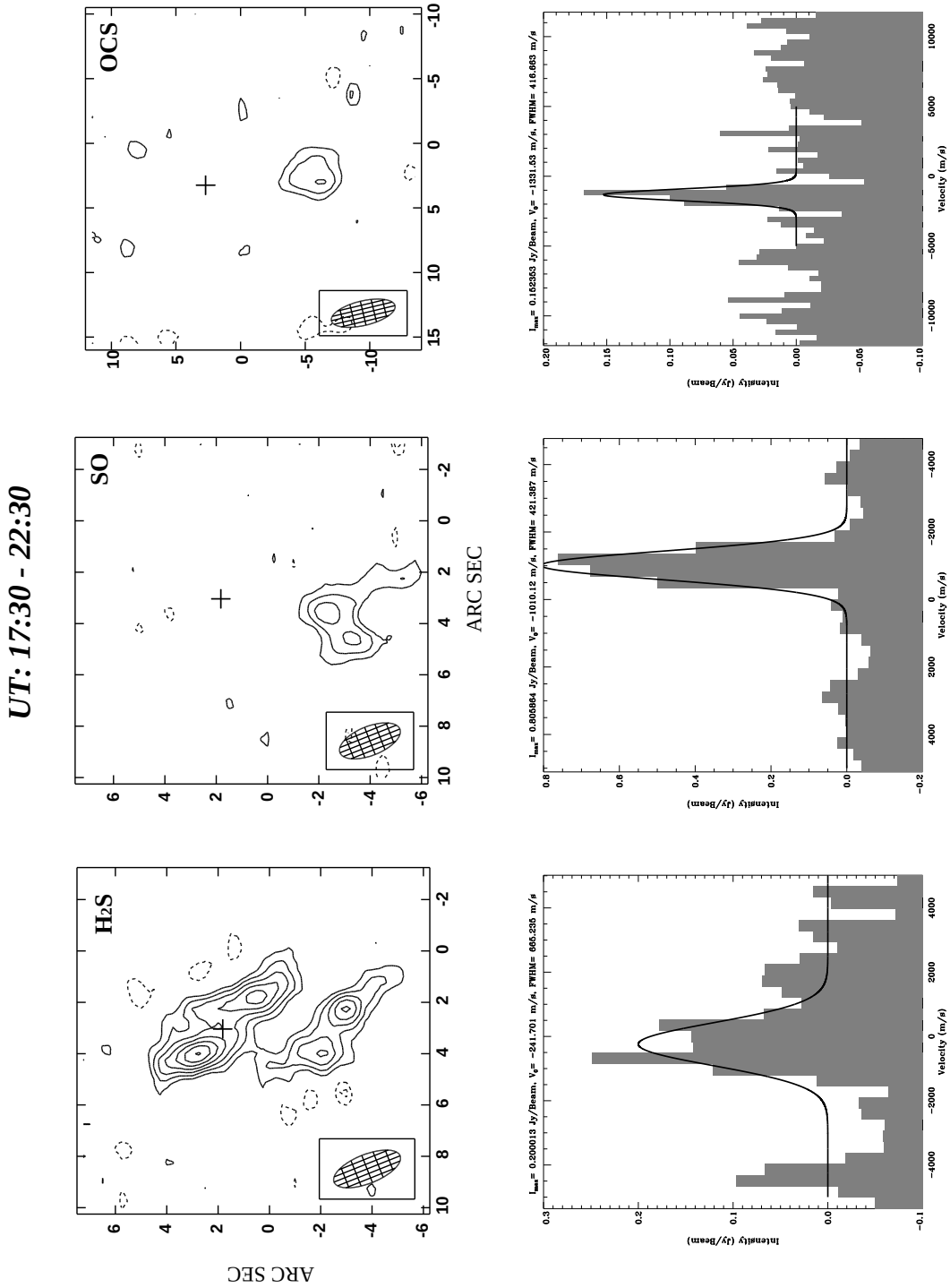

Figure 4.10: Additional sulfur-containing molecule observations from 1997 March 30 for an interval in which OCS emission is detected.

an extended fashion over a distance of nearly 10,000 km, or 10″.

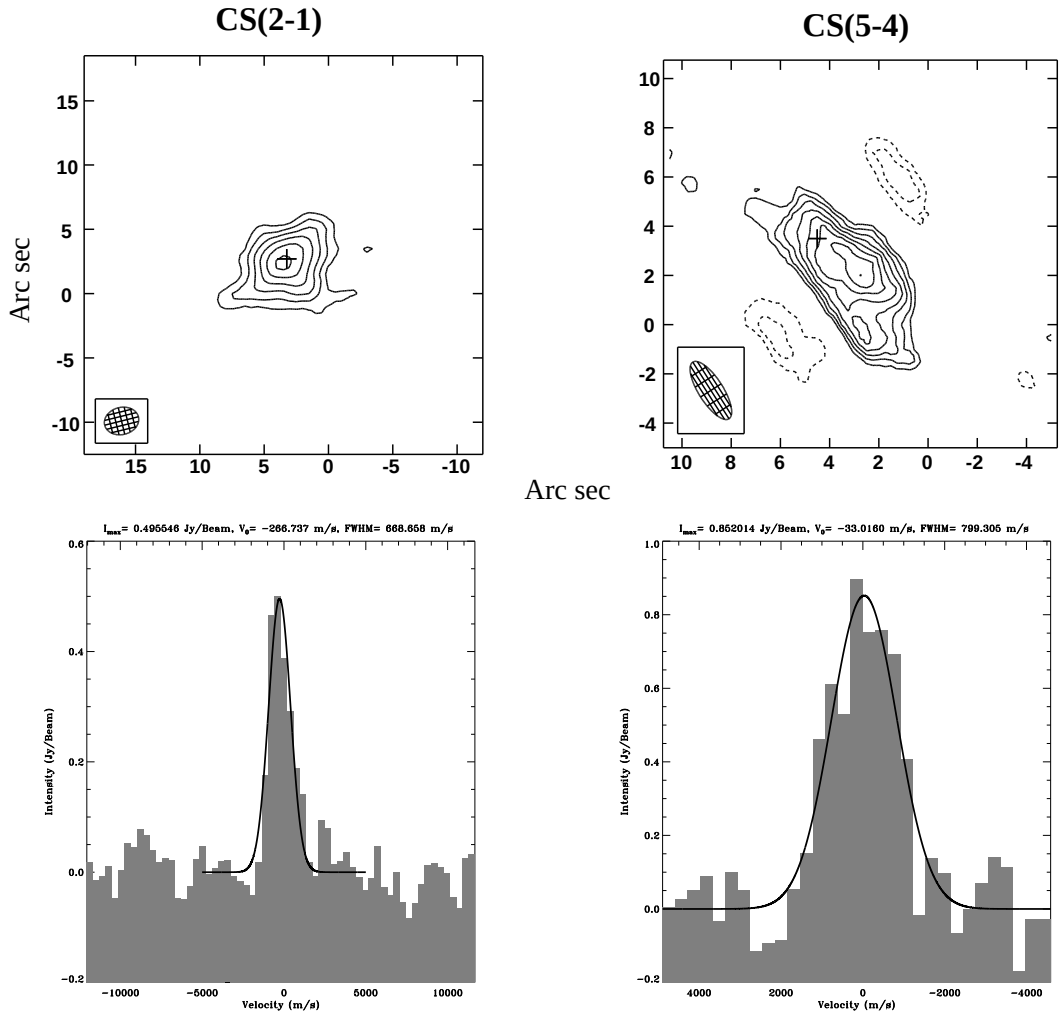

Figure 4.11: OVRO observations of the CS 2 → 1 (March 30) and 5 → 4 (April 02) transitions from the coma of comet Hale-Bopp.

CS emission is easily the most intense from the sulfur-containing molecules imaged at OVRO. J=2 →1 data were acquired from March 30 15:38 UT to March 31 2:32 UT. The resolution is 3″. From Figure 4.11, it is clear that the CS 2 → 1 emission is centered on the nucleus, with a FWHM of 1.6 km/s that is blue-shifted by 270 m/s. The LTE Haser production rate derived from the 2 → 1 line is 1.2×10^{28} s^{-1}, just over half of the value derived from single dish data (1.7×10^{28} s^{-1}). Sampling correction bias estimates with the SE model bring the interferometer and single dish production rates into good agreement. A CS 5→4 image, generated from data acquired on 1997 April 2 from UT 00:16:30 to UT

00:23:30, is also presented in Figure 4.11. The relatively strong negative sidelobes observed in this map are indicative of extended emission that is resolved out by the array, and so production rates would be suspect using these data.

A better use of the CS $5 \rightarrow 4$ data employs the high spatial resolution and sub-km/s spectral resolution afforded by the heterodyne observations to examine how the CS emission features change with time and position, a summary of which is presented in Figures 4.12 and 4.13. The observed changes in the velocity asymmetries (Figure 4.12) are modulated at the rotation rate of the nucleus, and can be only explained by relatively large aspect angles and gas jets that are located near the cometocentric equator. At 1-2″ resolution, the CS line shape is found to exhibit a number of components as the gas moves away from the nucleus, especially in the anti-solar direction. When imaged over a temporal range short compared to the rotation period, the most interesting aspect of the CS channel maps (see Figure 4.13) are the shell-like features extending in the sunward direction, which are coherent both in their kinematic and spatial properties.

As successively larger annuli centered on the nucleus are used to synthesize spectra, the CS abundance is found to rise dramatically over few arcsecond scales. This is direct evidence that CS is the daughter of another species with a short photochemical lifetime, typically assumed to be CS_2 (Jackson et al. 1982). CS observations at $8.''5 \times 6.''7$ with the BIMA array reveal a scale length of $10''$, or a CS lifetime of $\sim 10^4$ s (Snyder et al. 2001). This lifetime is much shorter than commonly assumed (Jackson et al. 1982), but still long enough that production rate estimates with the 1-3″ resolution employed at OVRO need not be extensively corrected. The inner edge of the CS shell is some 2″ to 3″ in extent, corresponding to diameters of ~2000 - 3000 km. For an expansion velocity of 1 km s^{-1}, approximately that derived from the spectral line widths of CS and HCN, the CS parent molecule lifetime is ~1000-1500 s. This is somewhat larger than that of CS_2 in the unattenuated solar radiation field at 1 AU ($\tau_{CS_2} \sim 400$ s at 1 AU, Crovisier 1994). Extinction in the high density regions of the coma near the nucleus may explain some of the difference between the estimated and predicted lifetimes of CS_2, or another sulfur species may be responsible for the CS production.

For example, H_2CS is another molecule that readily dissociates to yield CS, but there is presently insufficient laboratory data to enable the lifetime of H_2CS to be estimated under interplanetary conditions. The $7_{16} \rightarrow 6_{15}$ transition of H_2CS at 244.048 GHz was observed

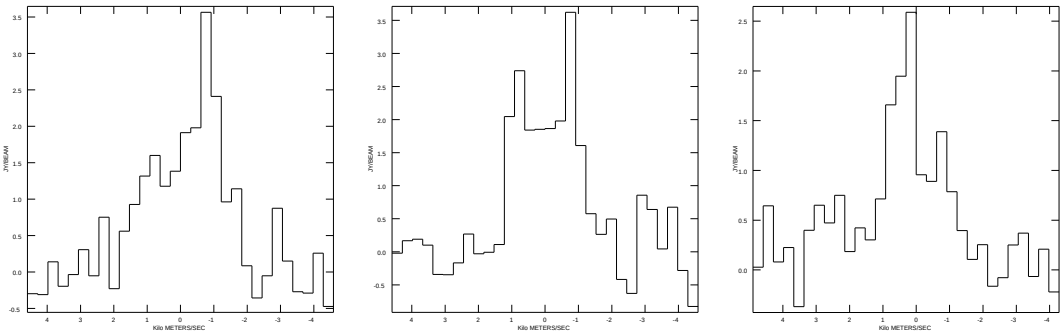

UT: 16:30 - 18:30 UT: 18:30 - 21:30 UT: 20:30 - 23:30

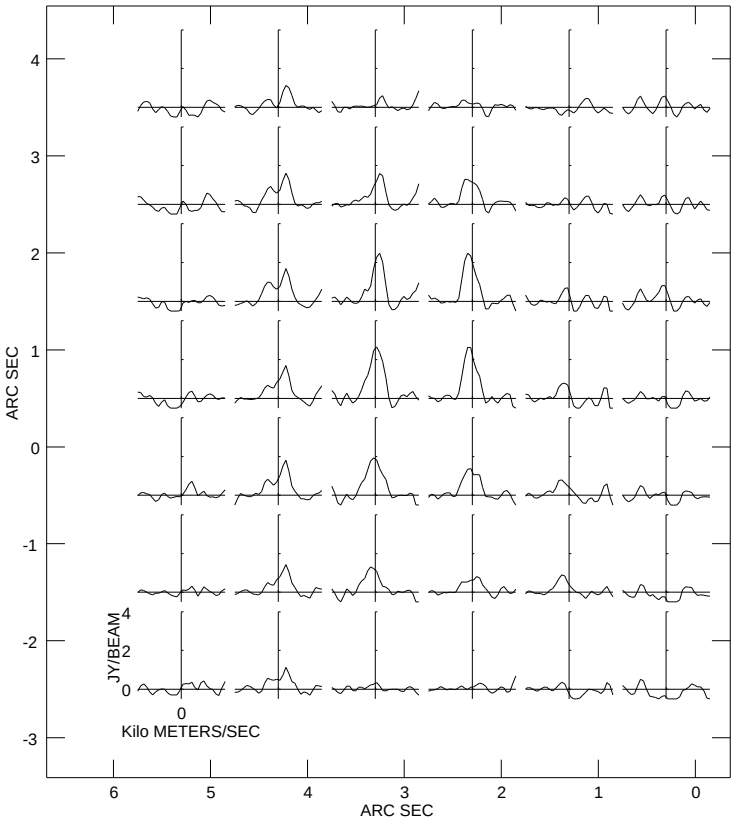

UT: 20:30 - 23:30

Figure 4.12: CS spectra for different time intervals illustrating the effect of the nucleus rotation on spectral line profiles.

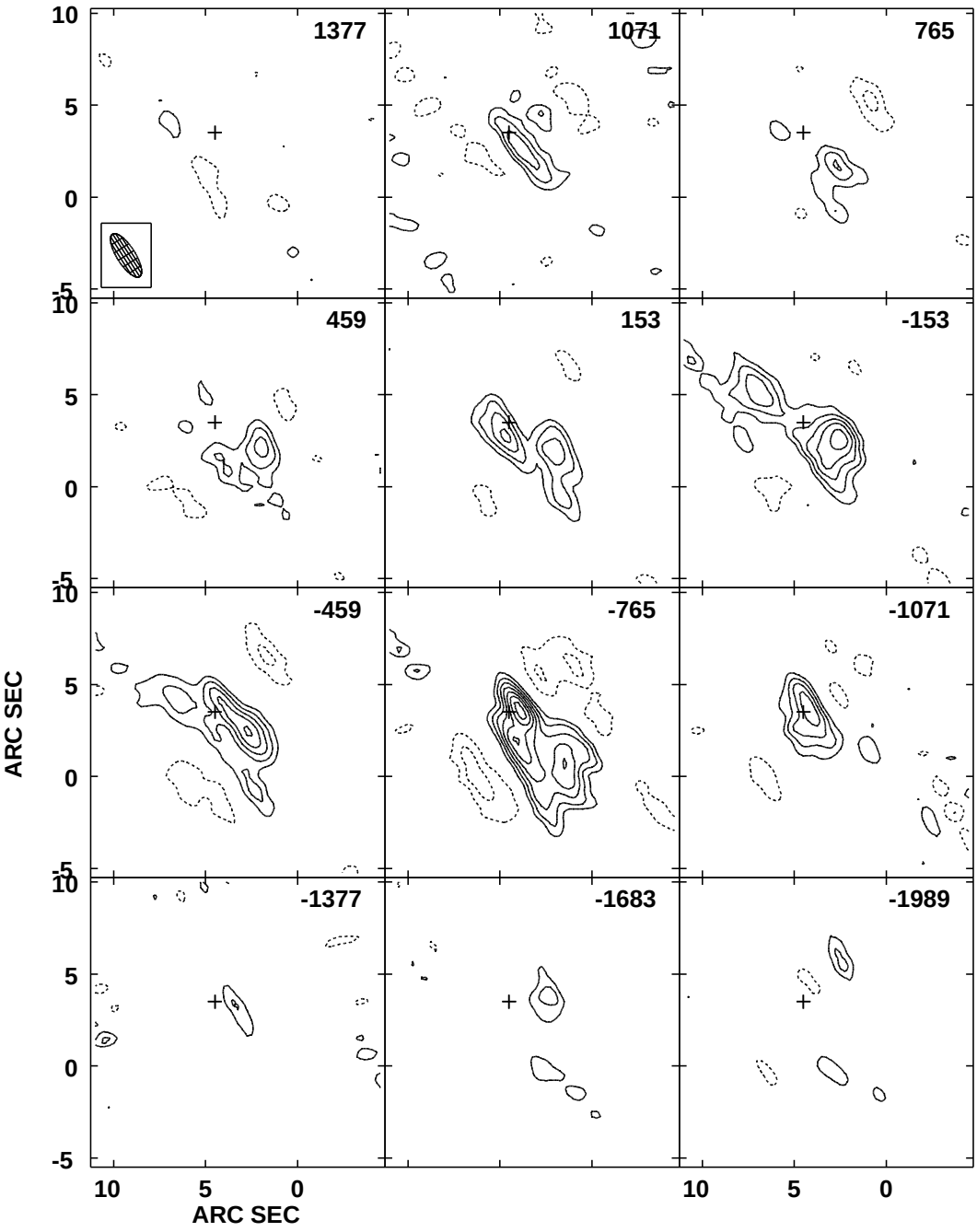

Figure 4.13: High resolution channel maps of the CS $5 \rightarrow 4$ emission from comet Hale-Bopp. The velocity offset from the calculated rest velocity frame is noted in m/s in the upper right corner of each panel.

on 1997 April 02, but not detected. From the rms of 46 mJy/bm in 0.4 km/s spectral channels, an upper limit to the H_2CS production rate of $2.\times10^{27}$ s^{-1} is derived, similar to that estimated from single dish observations (Woodney et al. 1999).

4.3.4 CO, CH_3OH, CH_3OCH_3 and HCOOH

The CO $2 \rightarrow 1$ transition was mapped on 1997 April 1 between 19:00-23:00 UT with a beam size of $2.''1 \times 1.''7$ (see Figure 4.14). Two CO peaks are seen, one centered on the continuum source and another some 5-6$''$ offset toward the south. The spectrum on the continuum source is red-shifted by 530 m/s with a FWHM of 1.5 km/s, while the spectrum on the jet is red-shifted to 540 m/s with FWHM of only 0.8 km/s. By modeling the emission centered on the nucleus with a Haser model and that for the offset emission as arising from a more collimated jet source, the derived production rates are 3.0×10^{30} s^{-1} and 1.1×10^{30} s^{-1} respectively. In this case, the total production rate of 4×10^{30} s^{-1} is larger than the single dish value of (2.3×10^{30} s^{-1}). CO is well known to have both an extended source from dust along with outgassing from the nucleus, but for Hale-Bopp the emission from each appears to be well recovered by the interferometric observations.

The CH_3OH $5_1 \rightarrow 4_1$ E^- and $5_0 \rightarrow 4_0$ A^+ lines at 241.767 and 241.791 GHz were studied on 1997 March 29 and April 1 with a single 64 $\times$ 0.5 MHz digital correlator set up with the LO set to 241.77 9GHz. The four lines are thus placed near the ends of the spectrum, as shown in Figure 4.15. The methanol emission peaks near the continuum source and changes very little during the observations (16:00-23:00 UT). The integrated intensity is 15.5 K km/s for the $5_1 \rightarrow 4_1$ E^- line and 11.9 K km/s for the $5_0 \rightarrow 4_0$ A^+ transition on March 29. The CH_3OH production rates derived from the $\lambda = 1.3$ mm lines are 9.3×10^{28} s^{-1} and 6.5×10^{28} s^{-1} respectively, or roughly a factor of 2-3 smaller than the single dish production rate of ($2.\times10^{29}$ s^{-1}).

Emission from the $CH_3OCH_3(7_{07} \rightarrow 6_{16})$ transition at 111.783 GHz was marginally detected between 16:15 UT April 1 and 3:12 UT April 2 (Figure 4.16). The line is very weak, and as a result short time-averaged maps tend to be very noisy. The peak of the emission lies near the continuum source for the full track 11 hour average, and the spectrum is quite symmetrically centered on the rest frequency. For short integration times this would suggest that CH_3OCH_3 arises primarily from the nucleus, but either a coma or jet source will also be averaged to the phase center for tracks taken over a full nucleus rotation period. Because

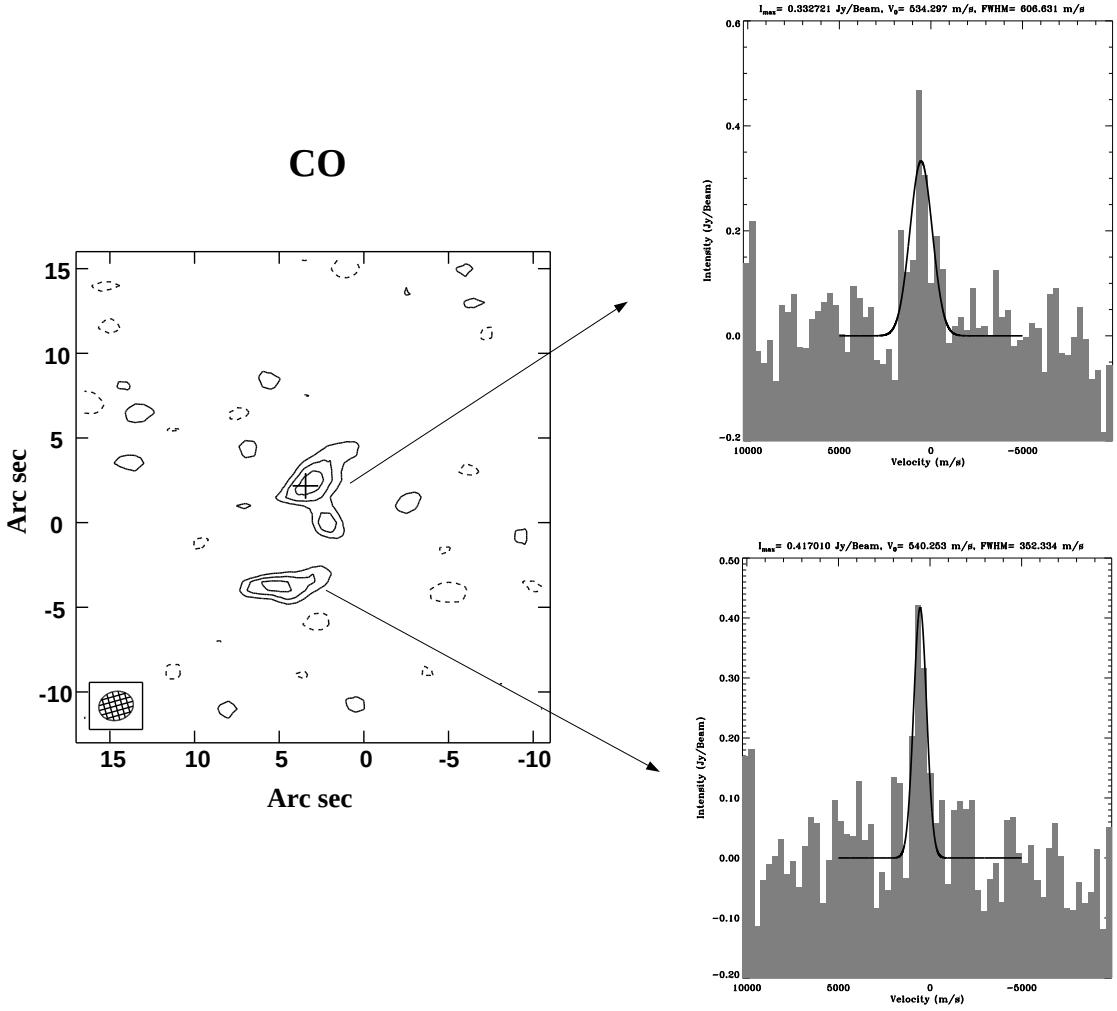

Figure 4.14: CO emission from comet Hale-Bopp. Spectra for the emission peaks on the nucleus and jet are shown at right.

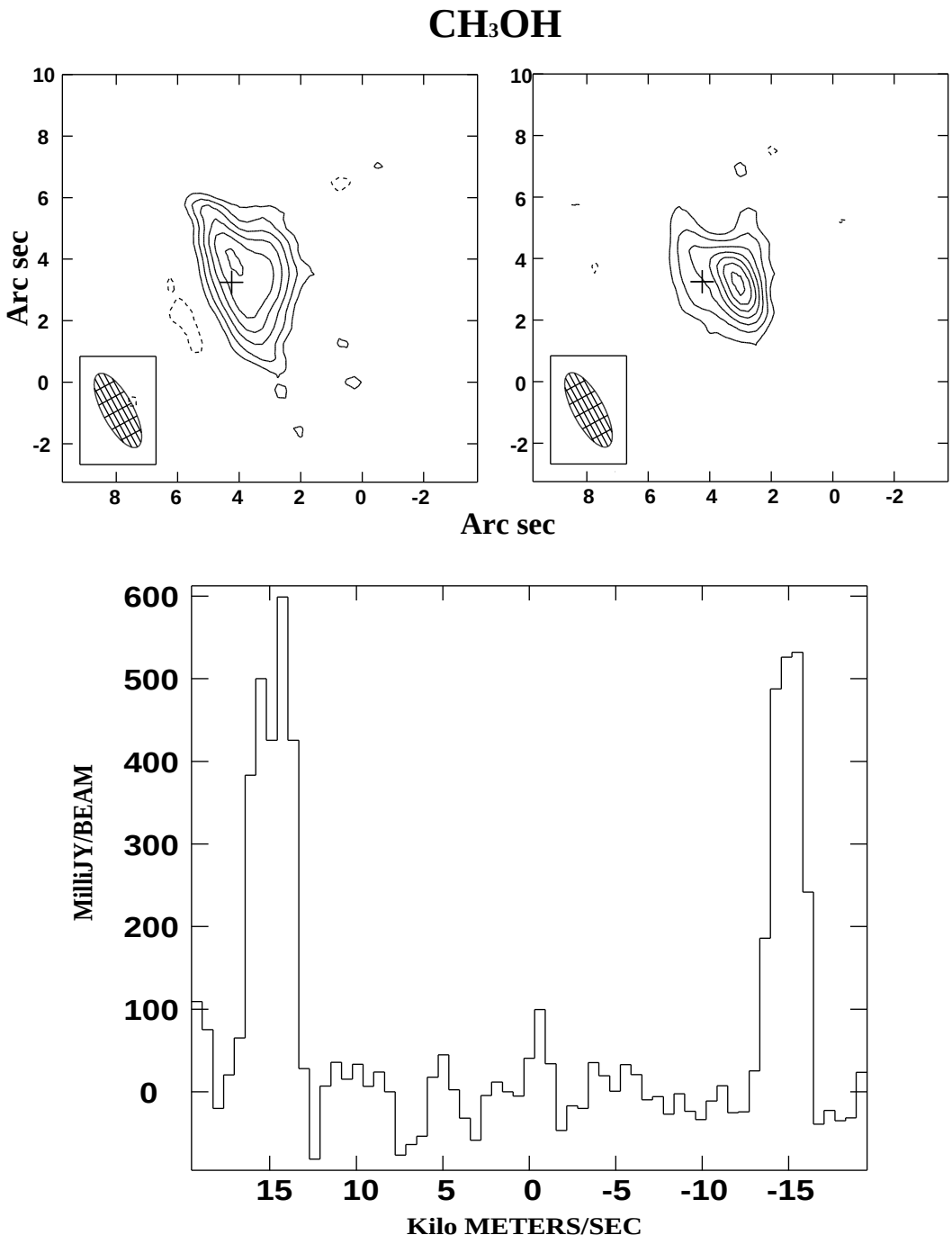

Figure 4.15: CH_3OH emission from comet Hale-Bopp on 1997 March 29. The two panels at top correspond to the E and A state lines visible in the spectrum below.

the line is so weak, we consider the derived CH_3OCH_3 production rate of 2.0×10^{29} s^{-1} as an upper limit. The four line $13_{1,13} \rightarrow 12_{0,12}$ multiplet at 241.946 GHz was observed but not detected, and yields upper limits to the CH_3OCH_3 production rate of 3×10^{29} s^{-1}. In both cases, checks of the available millimeter-wave spectral line databases yielded no likely contaminants in these frequency windows.

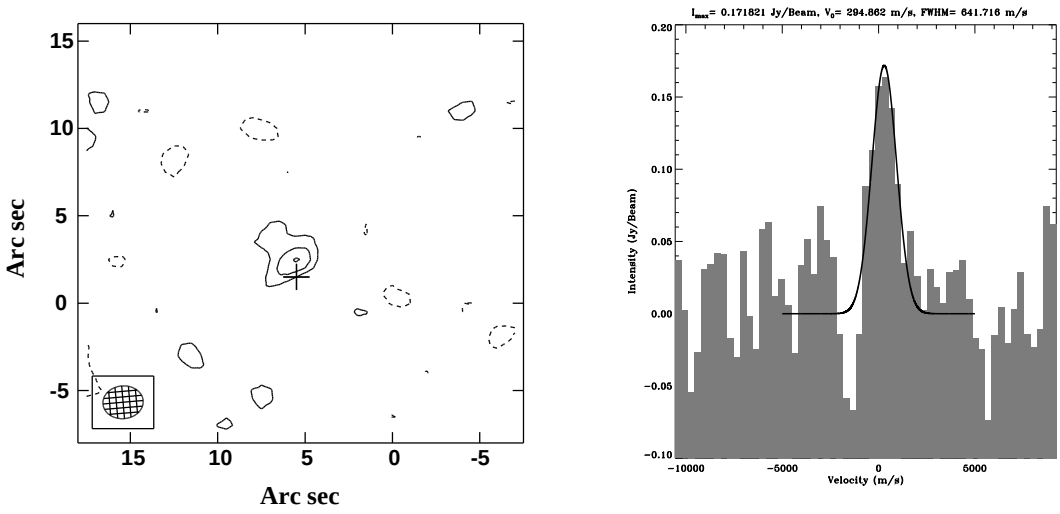

Figure 4.16: Emission from Hale-Bopp tentatively associated with CH_3OCH_3.

The HCOOH $5_{05} \rightarrow 4_{04}$ transition at 111.747 GHz was observed on April 1 with 0.3 km/s spectral line channels. The rms noise in map is 150 mJy/beam. These upper limits translate into an HCOOH production rate limit of 2.8×10^{28} s^{-1}, roughly a factor of 5-6 higher rate than the single dish detection that yields a production rate of 5×10^{27} s^{-1}.

4.3.5 Discussion

By comparing the volatile composition of comets with those of other solar system bodies and with the chemistry that occurs in the various stages of star formation, a better understanding of chemical evolution during the birth of solar systems can ultimately be achieved. Accurate determinations of the production rates of various atomic and molecular species in cometary comae are the first step in this process. From these primary data, constraints on the actual composition of the nucleus itself can then be obtained, provided a clear distinction

between the molecules produced by chemistry in the coma (daughters) from those which reside in the nucleus (parents) is possible. As noted above, single dish (sub)millimeter-wave spectra lack the spatial resolution to image the near-nucleus environment, but from the variations in production rates with distance clues as to whether the species in question is a parent or daughter can be ascertained (Biver et al. 1997a). More direct information about whether molecules indeed sublime directly from the nucleus or are produced by extended sources is, in principle, available from aperture synthesis imaging. The rapid temporal variability of comets and their extended, complex three-dimensional structure means that great care must be used in interpreting the poorly sampled data sets generated by the present generation of small millimeter-wave interferometers, however, especially when considering the many assumptions that must be made in order to derive production rates from the observed spectral line intensities. Indeed, given the very different observational selectivities, single dish and interferometer production rates need not be similar, but the differences are interesting in that they contain information about the spatial distribution and chemistries of the molecules detected.

Fortunately, both the images and the spectral line profiles can be used to examine the sources of gas phase species in comets. From the results presented above, we divide the molecules imaged at OVRO into two categories: Type I molecules are those for which emission peaks on the nucleus but for which weak arc features are seen that change with time in a manner consistent with jet features observed in the optical and infrared. Type II molecules peak on the jet with little emission centered on the nucleus. This simple categorization is provided only for convenience; the sources of individual molecules within the Type I or II classifications may in fact be quite distinct. For certain molecules that peak on the nucleus, in particular CH_3OH and CH_3OCH_3, long averaging times are needed, and so the sensitivity may not be sufficient to detect spatial variations in these species by interferometric imaging alone.

Comparisons with the fluxes and production rates derived from single-dish data can provide some of the necessary ancillary data, and so in Table 4.3 we present the relative production rates derived here with those compiled from a variety of publications. Since water is not directly observable from ground based telescopes, we first construct internally consistent production rate ratios based on the OVRO observations of HCN. The overall composition with respect to the major cometary volatile, water, is then constructed using

Table 4.3: Observed Interstellar and Cometary Ice Compositions

Species	Hale-Bopp (Interferometry)	Hale-Bopp (Single-dish)	NGC7538 IRS 9	W33A
H_2O	100	100	100	100
CO	64	23	10	8
CO_2		20		13
CH_3OH	2	2.4	9	18
HCN	0.25	0.25		
HNCO	0.5	0.1		3.5
HC_3N	0.03	0.03		
HNC	0.05	0.04		
H_2S	0.9	1.5		
CS	0.22	0.2		
OCS	0.21	0.5	0.1	0.2
SO	0.06	0.29		

[1] Single-dish data of comet Hale-Bopp from Irvine et al. (2000), interstellar ice composition of NGC7538 IRS9 from van Dishoeck & Tielens (2000), data of W33A from Gibb et al. 2000, in which the abundance of XCN is compared with HNCO in comets.

the literature values for HCN/H_2O as determined by simultaneous observations of HCN and OH throughout the perihelion passage of comet Hale-Bopp.

Further constraints on the nucleus versus extended source contributions to molecular production rates comes from the kinematic properties retrieved from the velocity-resolved spectral line profiles measured by the OVRO Millimeter Array. The simple Haser model predicts a sharp edged, double-peaked spectral lineshape, while smooth ones are observed. Hu et al. 1991 pointed out that three factors can generate smooth cometary lineshapes: the finite coma kinetic temperature, radial variations in the expansion velocity, and anisotropic flow patterns. The coma kinetic temperature affects the spectral linewidth by no more than 10%, while anisotropic outflows and expansion velocity fluctuations can be very important. Moreover, these two parameters affect the line shape in opposite ways: the width increases with the expansion velocity, but it decreases and shifts to the red or blue when the anisotropic outflow component is large. Thus, the most obvious signatures of anisotropic outflow are line shifts and reduced line widths compared to the dominant Haser flow.

In our observations, the typical FWHM of the molecular spectrum from nucleus is around 1.6-2.0 km/s, which corresponds to 0.8-1.0 km/s outflow velocity. Expansion velocities closer to 1.2-1.3 km/s are derived from large beam observations near perihelion (Biver et al. 1997b);

in agreement with the Monte Carlo simulations of Combi (1989), who finds that after an initially rapid gas acceleration zone some several tens of km in radius a more shallow growth in outflow velocity of some 20-30% over size scales of 1000-100,000 km (1-100″). The typical FWHM of the molecular spectra from jets is only 0.8-1.0 km/s, much narrower than those measured toward the nucleus. Certain molecules show an even wider velocity profile (>2.0 km/s) that may well be indicative of higher velocity wings caused by extended dust sources.

The type I molecules are HCN, CS, CO, H_2S, CH_3OH, and CH_3OCH_3, while the type II molecules include HC_3N, HNCO, SO, OCS, DCN, HDO and HNC. With the exception of CS, the production rates of all sulfur species derived in small beams are found to be roughly an order of magnitude lower than those found with single dishes. For CS, the 3 mm J=2 $\rightarrow$ 1 observations have poorer spatial resolution and yield a production rate similar to that in larger beams, but the $\sim$2″ J=5 $\rightarrow$ 4 visibilities yield only 1/10th the production rate measured on 10-30″ scales. CS has long been thought to be a photolysis product, and from our measurements the lifetime of the parent molecule is found to be only a few thousand seconds in the solar radiation field. SO is another daughter species whose parent is thought to be SO_2. Interestingly, the maps of SO are far more similar to DCN than CS in that they peak strongly on the jets, and suggests the rather different volatilities or nucleus versus extended sources for the respective parents.

For the other sulfur species, the smaller production rates derived by OVRO observations compared to those from larger beam measurements are most likely due to sources of extended emission above that predicted by the Haser+jet model implicit in our LTE and SE treatments of the OVRO data. Simple resolving out of extended coma structure consistent with the Haser model can be accounted for, but extra emission on size scales large compared to that sampled by the array cannot be recovered without additional single dish data or mosaicing of the array phase centers (Wright et al. 1998). The FWHM seen for H_2S, nearly 2.3 km/s at the nucleus, is much wider than those of HCN and CO, and is also consistent with a substantial contribution from an extended source. Sulfur in comets is likely to be stored largely in grains, for which the [S]/[Mg] is somewhat larger than solar (Schulze & Stoffler 1997), and so dust processing either by solar photons or sputtering forms a natural explanation for our observations.

For the remaining type I molecules, HCN and CO show clear signs of jet activity while none are seen for CH_3OH and CH_3OCH_3, most likely due to sensitivity limitations. For

HCN and CO, a larger jet (extended) source fraction is derived for CO, consistent with *in situ* measurements of comet Halley that revealed a significant dust source for this molecule (Fomenkova & Chang 1997). The production rate of CH_3OH, a grain mantle hydrogenation product of CO in dense molecular clouds, is one magnitude lower than that from single dish data, so this molecule is also likely to have a substantial dust component.

The deuterated species DCN and HDO arguably form the most interesting set of type II molecules. As indicated in Blake et al. (1999) and summarized above, the calculated production rates are nearly almost one magnitude larger than those from single-dish data which assume the molecular emission fills the main beam. If, however, species such as DCN and HDO have small sources that are spatially and spectrally associated with jets, clearly there is a beam filling factor which single dish analyses ignore. The resulting beam averaged column densities from interferometry are therefore larger, resulting in higher production rates, especially if the optical depth approaches unity. Similar effects may also explain the discrepancies observed for the production rates of CO and HNCO. Interestingly, HC_3N shows comparable interferometer and single dish production rates, and of these molecules it has the widest, most symmetrical spectral line profile that is consistent with and extended source of emission.

What physical and chemical processes, as opposed to observational bias, might contribute to such significant differences between the volatile ratios on single dish and interferometric scales? The early assumption of a crust-free nucleus surface inherent in the Haser model was questioned by the results of the spacecraft flybys of comet Halley, which showed strong evidence for the existence of an insulating crust (Sagdeev et al. 1986). As cometary nuclei return to the planetary region, their physical evolution is dominated by the heating they receive from direct solar radiation and other minor processes (see Mumma et al. 1993 for a review). Two processes contribute to formation of a non-volatile crust. On a comet's approach to the Sun, the thermal pulse created by the conversion of amorphous to crystalline water ice propagates inward some 10 to 15 m. The exact penetration depth of the thermal pulse is dependent upon the thermal conductivity of cometary ice, a poorly constrained parameter at present (Greenberg & Li 1999). The second, insolation-related, process is driven by the sublimation of volatile ices at the nucleus surface, which results in the extended cometary coma so widely observed. Larger grains of non-volatile materials not entrained by the escaping gas will begin to form a lag deposit on the nuclear surface,

accumulating to form a crust that will begin to seal the nucleus against further mass loss. The near-surface layers may thus be depleted in many of the more volatile ices.

Indeed, according to numerical calculations, a single perihelion passage should only result in the sublimation of a layer several meters thick, smaller than the range reached by the thermal pulse itself (Prialnik 1997). As a result, gas production rates (relative to water) for species of different volatility should show a marked difference in their radial dependence until water sublimation dominates the outgassing, and such differences are in fact observed for comet Hale-Bopp (Biver et al. 1997b). Further, the active fractional area of the cometary nuclei has been estimated to be 20-30% of the sunlit surface, based on spacecraft imaging and measurements of the gas production rate (Bockelée-Morvan & Rickman 1997). The few active areas serve as pressure release points, resulting in the formation of jets, which plays an important role for bringing volatiles deep in the nucleus to the surface as cracks propagate into the ice. For large comets such as Hale-Bopp, active jets can lift grains larger than 1 mm in size. Once exposed to the Sun, these grains warm rapidly and any volatiles are released. Single dish examinations average over large spatial dimensions, whereas the the resolution and spatial filtering of an array enables the emission associated with the dust/gas jets close to the nucleus to be selectively highlighted.

Thus, single dish and interferometric constraints on the volatile composition of comets should be carefully compared for they may access different regions of the nucleus. Clearly, the most volatile species (such as CO) will be depleted on the surface of the nucleus. In the deeper regions of the comet, especially those below the thermal pulse, the true volatile content of the comet should be maintained, either trapped into clathrate/hydrates or amorphous ices. If clathrates are formed, the high volatile content of comets is such that the nucleus is likely to be segregated, with volatile rich grain boundary phases interspersed throughout the interior, as suggested by laboratory results for H_2O:CH_3OH ices (Blake et al. 1991). This segregation can lead to the build-up of a sufficiently high volatile pressure to disrupt the cometary body and lead to an explosive gas discharge known as jets, or to the disruption of the comet itself as was recently observed for comet LINEAR. Outgassing from these active areas need not be regular, and can be driven by volatiles other than water, especially CO. For example, Samarasinha & Belton (1994) have proposed that the extended source for CO in comet Halley originated in a collimated vent rather than a spherically symmetric source, and such a scenario would naturally explain the narrow CO

spectrum observed by the OVRO Millimeter Array.

Gases sublime from the nucleus as a Knudsen flow through a porous medium, and the most volatile species released must pass through warmer overlying surface layers. Species released from grains in the coma pass through less material but are exposed to intense solar radiation. Interestingly, studies of crystalline ice in the 140-210 K range have shown that a viscous water layer coexists ubiquitously (Jenniskens et al. 1997). Various reactions can take place in this thin liquid layer, with the result that the potential modification of subliming volatiles becomes pathlength dependent, perhaps explaining the differences observed between the jet and nucleus outgassing in the OVRO images. Little is presently known about the stability of high energy species such as HNC against isomerization to HCN as it diffuses through warm ice, water, and dust, but the rapid radial variability of the (HNC/HCN) ratio suggests that some alteration occurs. Further, the acidity of HCN is sufficient to exchange (D/H) even in thin layers of water under laboratory conditions. The $(D/H)_{HCN}$ ratio, and by inference in other trace species with labile hydrogens (NH_3, CH_3OH, HCOOH, etc.), subliming from the nucleus of comets may therefore be controlled by that of the major constituent, water.

If such an exchange process occurs, the $\lesssim$0.025 $(D/H)_{HCN}$ ratios measured in the DCN arcs may be more representative of the ices trapped within the nucleus, ices that would otherwise be detectable only with direct sampling techniques. Since the region of high (D/H) gas is small and mixed with sublimation from the nucleus itself, it is difficult to detect in larger beams, and suggests that the (D/H) ratios in trace species with exchangeable hydrogen atoms should be viewed with caution when averaged over large spatial dimensions. To be consistent with the JCMT (DCN/HCN) ratio, the DCN jets can represent at most 10-15% of the total gas production rate. This is somewhat larger than the mass loss rate of mm-sized grains from Hyakutake (Harmon et al. 1997), but is consistent with the HCN limits noted above.

Given these complications, the volatile composition presented in Table 4.3 has used the total production rates derived interferometrically and single dish measurements taken as close to the OVRO observations as possible. Our interferometry data is comparable to the single-dish data, considering 10-25% of noise level in our data and the uncertainties associated with the resolving out of large scale emission by the array. A number of interesting parallels between the chemistry in comets and that observed during star formation are read-

ily apparent, and have been commented on by many authors (see Bockelée-Morvan et al. 2000; Irvine et al. 2000 for an overview). Most notable is the presence of both reduced and oxidized compounds (H_2S and SO, for example). Comets, like interstellar ices, are clearly the products of kinetically-controlled chemistry, and thus a cometary volatile origin from regions near warm, dense Jovian sub-nebulae is ruled out. The major question at present is where did this kinetically controlled chemistry occur? Bockelée-Morvan et al. (2000) support models in which cometary volatiles formed in the interstellar medium and suffered little processing in the solar nebula, similar to arguments of Greenberg & Li (1999) who suggest that comets consist of accumulations of essentially unaltered interstellar grains. In support of this line of reasoning, the species that are found to dominate the infrared spectra of interstellar ices are also abundant in comets, with comparable overall compositions (Table 4.3, van Dishoeck & Tielens 2000). Furthermore, the high ratio of HDO/H_2O and DCN/HCN (Blake et al. 1999; Bockelée-Morvan et al. 1998; Meier et al. 1998a) observed in comets are comparable to those in hot cores, and the spin temperature of water is of order 20-30 K. Both suggest that cometary materials are synthesized at low temperatures, while the retention of highly volatile species such as CO and H_2S demands that cometary materials remain at very low temperatures throughout their stay in the outer solar system.

As Chapter 3 of this thesis shows, however, due to the presence of UV radiation and cosmic ray ionization in protoplanetary disks, photo- and and cosmic ray-induced chemistry similar to that active in the interstellar medium also makes substantial contributions to the molecular composition of gas and dust in comet-forming regions. In the outer disk, Aikawa & Herbst (1999) show that cosmic ray can penetrate even to the disk mid-plane and initiate deuterium fractionation chemistry either in the gas phase or in grain mantles. It is therefore likely that cometary constituents were processed in the disks before and during comet formation, and that the signposts of this chemistry will be similar to those familiar from studies of molecular clouds. The present observational work on disks is limited to radii beyond the comet forming zone in our own solar system, and at these distances there is some question as to whether the material will be driven inward to the planet-forming region or removed from the system, at least for older disks (Johnstone 2000).

4.4 Summary

In this chapter we have presented interferometric images and spectra of comet Hale-Bopp as observed by the OVRO Millimeter Array during the perihelion passage of Comet Hale-Bopp. These aperture synthesis millimeter-wave molecular line and continuum observations reveal in great detail the inner coma of comet Hale-Bopp. Continuum emission is readily detected and spatially resolved in both the 3 mm and 1.3 mm wavelength bands with synthesized beams of $3''$ and $1''$, respectively. Even in the $1''$ beam the continuum flux is dominated by the thermal emission from large ($\geq$ millimeter-sized) grains in the comet's coma. Consistent estimates of the dust production rate of 2.4×10^5 kg s^{-1} from the 1.3 mm and 3 mm short baseline visibilities requires an emissivity index of $\beta = 0.45 \pm 0.25$ for dust within $20''$ (about 20000 km) of the nucleus. The emissivity index is similar to that observed in the proto-planetary accretion disks around young stars. By subtracting out spherically symmetric models of the coma dust emission, upper limits of 1.9 mJy at 90 GHz and 8.0 mJy at 221 GHz are found for thermal emission from the nucleus itself. For an emissivity of 0.9 and a surface temperature of 195 K, this corresponds to a nucleus radius of 18 km; a value in good agreement with other millimeter-wave and optical measurements of the size of Hale-Bopp.

Observations of over 18 transitions from the species HCN, DCN, HDO, HC_3N, HNC, HNCO, CS, H_2S, SO, OCS, CO, CH_3OH and CH_3OCH_3 were acquired simultaneously with the continuum measurements. At these long wavelengths, the effects of scattering and extinction are negligible, and the good spatial, spectral, and temporal resolution obtained has made it possible to investigate in detail both the rotational and jetting properties of the nucleus as well as a variety of physical and chemical processes in the coma. Such observations are only possible with interferometry, and were made possible in this case by the extraordinarily high production rates of comet Hale-Bopp and its favorable northern declination. Studying cometary emission on short time scales is also necessary for the detection of weak lines from several species such as DCN, HDO and HNC which appear to be coupled to jet activity (Blake et. al. 1999), and which are therefore resolved out by aperture synthesis observations averaged over a significant fraction of the rotation period. The brightness of the line emission from Hale-Bopp combined with its northern declination enabled high spatial resolution millimeter-wave maps of molecules associated with jets to

be generated over averaging times of ~3-5 hours.

Two types of molecules can be identified from the high resolution images. Type I molecules include HCN, CS, H_2S, CO, CH_3OH and CH_3OCH_3. Their emission is peaked on the continuum center, but weak arc features are also detected whose phase changes match those of jets seen optically. Type II molecules only show emission offset from the nucleus, and include DCN, HDO, HNC, HNCO, HC_3N, SO and OCS. Production rates have been derived and compared with those from single-dish measurements. This comparison, along with the spatial and spectral patterns measured interferometrically, can be used to ascertain the nuclear versus coma contributions to the production rates of the molecules observed. HCN and CO sublimate both from the nucleus and grains in the jets, but a larger fraction of CO arises from sources extended compared to the 2-3″ beam. DCN and HDO have intense peaks well removed from the nucleus, resulting in production rates within the jets themselves that are a magnitude larger than those deduced from single-dish measurements. Although HC_3N, HNCO and OCS also show emission peaks only on the jets, the FWHM of their spectrum are wider than those of DCN and HDO. It is therefore likely that additional extended sources, to which the interferometry is not sensitive, contribute to the production rates of these species. CS and SO both result from the photolysis of parent molecules, but the spatial differences between these two molecules indicates that their precursors come from very different sources. The production rates derived in this study and in other observations of comet Hale-Bopp reveal a marked similarity between interstellar and cometary ices, and are consistent with comet formation models in which the nucleus is assembled at low temperatures from a mixture of pristine interstellar and outer nebular grains and ices. While this clearly suggests an evolutionary history in which cometary materials remain at very low temperatures throughout their assemblage and for the bulk of their lives, the complex chemistry revealed in the OVRO images of the cold, outer regions of disks around young stars means that it is difficult to characterize cometary volatiles as being primarily "interstellar" or "nebular" in origin.

This is particularly significant for investigating the true composition and evolutionary history of comets using ground based millimeter-wave imaging, since jets are known to lift off large, icy grains from which direct sublimation can occur as they are exposed to the Sun. Thus, the direct observation of jet-like features can provide information on molecules which might not survive diffusion through overlying layers of ice and dust, and which might

otherwise be impossible to study without directly sampling the comet nucleus itself. High spatial resolution interferometric observations can also yield constraints on the photochemistry and chemical reactions which occur only in the innermost coma since emission on large spatial scales is selectively resolved out. While present arrays are only capable of such studies on the brightest comets, future instruments such as the Combined Array for Research in Millimeter Astronomy (CARMA) and the Atacama Large Millimeter Array (ALMA) will do much better. CARMA will be able to image the dust and molecular line emission from nearly all long period comets which pass within 1-2 AU of the Sun at perihelion, while ALMA will enable the first studies of the critical short period comet population that is thought to be scattered into the inner solar system from the Kuiper belt. Furthermore, the large number of elements in ALMA will enable very rapid, high dynamic range imaging, while its large collecting area will enable even very small or weakly outgassing (e.g. short period) comets to be studied. Such observations will greatly expand our understanding of the composition and processing of icy bodies in the outer solar nebula, and will therefore shed new light on the early stages of planetesimal growth and the assemblage of mature planetary systems.

Chapter 5 Conclusions and Future Possibilities

The research presented in this thesis represents the first steps in the characterization of the chemical composition of circumstellar accretion disks and comets with millimeter-wave interferometry. As such, it is largely preliminary and a great deal of further work, both observational and theoretical, remains to be done. Theoretically, radiative transfer codes that can be coupled to the output of spatially resolved chemical models are badly needed. These models should be able to sample the model emission profiles with the same suite of (u, v) spacings that are acquired observationally so that quantitative fits to the flux densities, including rigorously defined error estimates, can be acquired. The codes should be efficient enough that large regions of parameter space, both physical and chemical, can be searched with workstations of modest computing power. Recent work along these lines is encouraging (Hogerheijde & van der Tak 2000), and can be expected to continue. SE codes should be used whenever possible, but are only available at present for simple molecules due to the lack of laboratory or theoretical estimates of the collision cross sections with H_2 in the case of circumstellar disks or with H_2O for comets.

The observational challenges are also considerable:

- Protoplanetary disks are small, with a complex internal physical and chemical structure. The spatial resolution achieved by millimeter-wave interferometry to date (0.5-1″ $\sim$ 70-140 AU) is still too coarse for detailed analyses of the properties and evolution of disks, especially for the critical planet-forming region between 1-30 AU. Easily detected molecular transitions are optically thick, and detecting the weak isotopes that would be $\sim$optically thin is very difficult with the current sensitivity. By comparing the ratio of those species with similar estimated optical depths to get a rough idea of the actual abundance ratios, we have found that an active, kinetically-controlled chemistry similar to that observed in molecular clouds dominates the composition of the outer reaches of circumstellar disks. For older disks, an interesting question arises as to whether this material will be transported inward to the planet-forming zone, or whether it will be lost by photoevaporation or other disk dissipation processes. To

answer this question, extremely high spatial and spectral resolutions are needed.

- Comets present a different, but no less compelling, suite of challenges to interferometric arrays. The nucleus of most comets is small, and so demands high resolution, high sensitivity imaging to be resolved from the coma. The large size of the coma, however, and the critical role of extended molecular sources, demands rapid imaging with excellent fidelity over at least a decade in angular scale. Careful mapping, or mosaicing, with detailed zero-spacing fluxes is required for truly quantitative numbers to be derived from small arrays such as OVRO since much of the emission is resolved out. Furthermore, since the nucleus and coma are moving and changing the emission with time, comets cannot be analyzed by adding the data from different dates as is commonly done for disk or other astronomical observations. Short integrations with excellent (u, v) coverage and high sensitivity will ultimately be required to image the jet features such as those seen in comet Hale-Bopp toward weaker comets. This is especially true for short period comets, about which very little is known but which form a likely reservoir for volatile delivery to the inner solar system.

Thus, for both disks and comets future interferometry at high spatial and spectral resolution and with excellent sensitivity and (u, v) plane coverage will be essential to disentangle the different physical and chemical regimes therein. A number of new observational capabilities will be coming on line over the course of this decade, from large ground based optical/infrared telescopes and interferometers to the Space Infrared Telescope Facility (SIRTF) and the Stratospheric Observatory For Infrared Astronomy (SOFIA) at short wavelengths, to the Far-Infrared Space Telescope (FIRST/Herschel) and a number of (sub)millimeter-wave aperture synthesis arrays. Given the focus of this thesis, we conclude with a brief overview of what these future interferometric facilities will bring to star formation studies and cometary science.

5.1 The Submillimeter Array (SMA)

The Submillimeter Array (SMA) is a collaborative project of the Smithsonian Astrophysical Observatory (SAO), a research bureau of the Smithsonian Institution, and the Institute of Astronomy and Astrophysics of the Academia Sinica of Taiwan (ASIAA). The SMA will be

sited in Millimeter Valley on Manna Kea, at an elevation of 4080 m. The array will consist of eight 6 m antennas that are reconfigurable to achieve baselines from 8 to 508 m. The array will cover all bands from 180 to 900 GHz and the first complement of receivers will cover the 180-250, 250-350, and 600-720 GHz bands (Moran & Ho 1994).

As interferometric observations at sub-millimeter wavelengths become more commonplace, searches for disk emission in molecules other than CO will be considerably eased due to the variety of transitions which can be imaged, often simultaneously, and to the increasing strength of the emission as shorter wavelength atmospheric windows are accessed. Further, the chemical differentiation in T Tauri/Herbig Ae disks presented in this thesis illustrates that the emission for a variety of species will be easily detected with the SMA, and opens the door to the detailed characterization of the physical and chemical processes at work in protoplanetary accretion disks. For example, the sharpness of the inner boundary of the morphology observed in CN and HCN should reflect both the temperature profile and radial transport within the disk. Due to the limited spatial resolution of the OVRO images, especially those at 3 mm, the research here is concerned primarily with the first quantitative estimates of chemical abundances in the accretion disks around T Tauri and Herbig Ae stars. In order to reach robust conclusions, however, it is necessary to observe various transitions and isotopomers at higher resolution. At higher resolution and at the appropriate disk orientations, it should be possible to measure the vertical mixing rate directly from the images and the estimated chemical lifetimes of CN and HCN. The SMA will be thus invaluable to future work in protoplanetary disk research through its access to frequencies from 180 GHz to 900 GHz and its sub-arcsecond angular resolution. Figure 5.1 summarizes the sensitivities which will be achieved by SMA on integration time of eight hours. For example, using the largest configuration (508 m) SMA can easily detect 10 K lines near 345 GHz at $0.''3$ spatial resolution. Even the 180-350 GHz and 600-720 GHz bands covered by the first complement of receivers alone include more than 20 strong lines from CN near 226, 340 and 680 GHz; from HCN at 267 and 620 GHz; $H^{13}CN$ at 260 GHz; and the important deuterated species DCN at 217 and 289 GHz. Mapping the strong line of HCO^+ at 268 GHz with higher resolution provides an opportunity to investigate in detail the question of whenever the magnetorotational instability (MRI) can operate throughout the disk. In this sense, imaging studies of the distribution of HCO^+, HCN, and CN through submillimeter interferometry at the SMA will provide unique indicators of various dynamical and chemical

SMA Sensitivity[a]

ν^b (GHz)	$T_{sys}{}^c$ (K)	θ^d ($''$)	ΔT^e (K)	ΔS^f (mJy)
230	142	5.9 0.4	0.02 5	0.4
345	340	3.9 0.25	0.04 10	1.0
460	1870	2.9 0.18	0.20 49	5.7
690	2640	2.0 0.12	0.24 62	8.7
820	4870	1.7 0.10	0.44 110	17.0

[a] Noise levels are 1σ values, based on integration time of 8 hours.
[b] Band frequencies are denoted by the frequency of the CO line they contain.
[c] SSB system temperatures with 1 mm of precipitable water and 1.5 airmasses (opacities of 0.075, 0.26, 1.2, 1.2, and 1.2 for 230, 345, 460, 690, and 820 GHz). The (DSB) receiver temperatures are 30, 50, 70, 180, and 500 K, respectively. System temperatures include a room temperature loss of 5% in coupling to the antenna.
[d] Resolution for the 32 m (smallest) and 508 m (largest) configurations.
[e] The Rayleigh-Jeans equivalent rms noise level in brightness temperature with 1 km s^{-1} resolution.
[f] Flux density rms noise level for 2 GHz bandwidth.

Figure 5.1: SMA Sensitivity (table provided by David Wilner)

processes in pre-planetary accretion disks.

5.2 The Combined Array for Research in Millimeter-wave Astronomy (CARMA)

The Berkeley-Illinois-Maryland Association (BIMA) and Caltech are proposing to combine their existing millimeter-wave instruments to form a merged array which will be sited in the Inyo Mountains near the present Owens Valley site. The new array will consist of six 10.4 meter diameter OVRO telescopes and nine 6.1 meter diameter BIMA telescopes, and as such will be the first millimeter-wave heterogeneous array. By combining the 10.4 meter telescopes, which provide collecting area to improve the overall sensitivity of observations, with the 6.1 meter telescopes, that provide a wider field of view and that can be placed in the inner positions of compact arrays to provide good access to (u, v) spacings 6 meters and shorter in projected length, it is possible to provide complete imaging of large scale structures. Indeed, once the arrays are combined, the resulting 105 baselines can produce very broad (u, v) dynamic range and excellent imaging. CARMA will thus have significantly improved sensitivity, resolution, and image fidelity compared to the current OVRO and BIMA arrays. At the high sites currently under consideration, routine operation in the current ν=110 GHz and 230 GHz bands will be possible, and during the winter limited operation should be possible at 345 GHz. The overall gain in continuum sensitivity should be roughly a factor of five due to the better atmospheric transmission and due to anticipation improvements in the receiver performance and wider IF bandwidth. The improvement in sensitivity for line work is more modest, but should be a factor of 2 - 3, especially at the higher frequencies.

The most important aspect of CARMA is its vastly improved imaging ability over current millimeter-wave arrays. Indeed, with fifteen antennas and scaled star configurations, the greatly increased number of baselines and dramatically improved (u, v)-plane coverage of CARMA render its imaging capabilities more like those of the VLA than any existing (sub)millimeter-wave aperture synthesis telescope.

Figure 5.2 presents an example simulation of how CARMA's improved imaging capabilities will benefit the study of disks around young stars. Here, reconstructed images of the dust continuum emission recovered by the current BIMA and OVRO arrays are com-

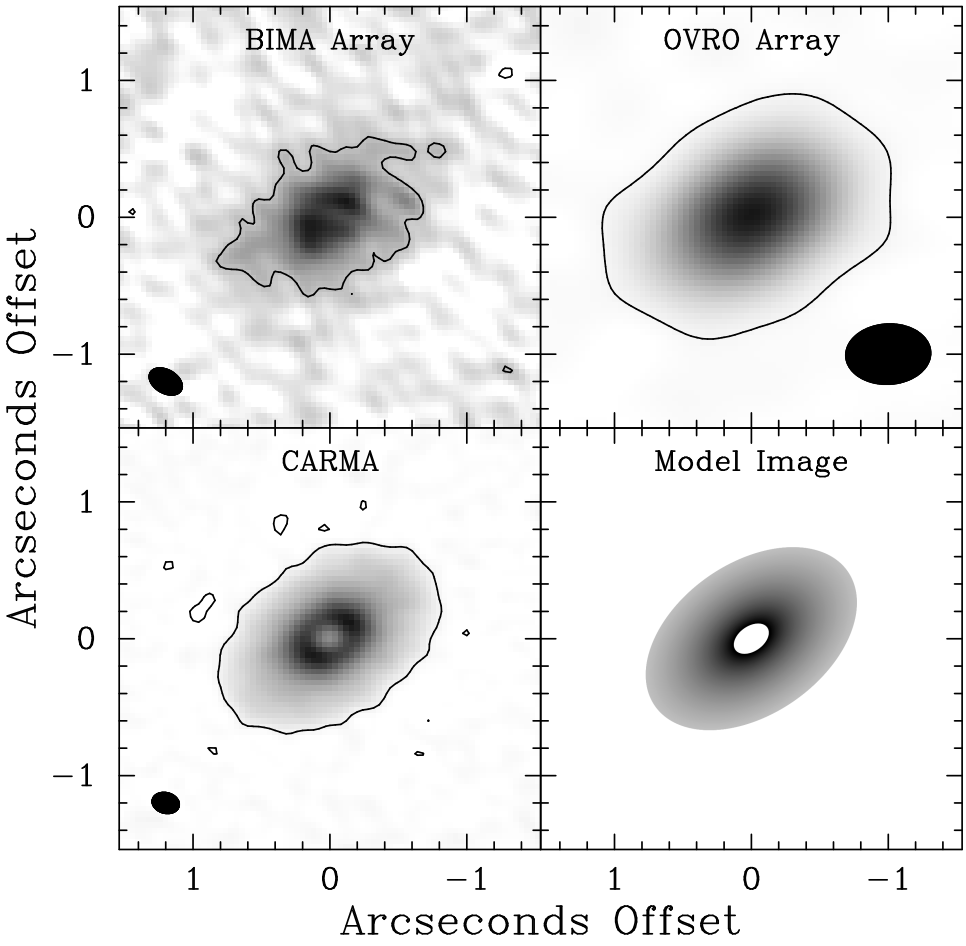

Figure 5.2: Simulated ν=230 GHz dust continuum imaging of a circumstellar disk at a distance of 150 pc using the existing highest resolution capabilities of the BIMA and OVRO arrays, along with the proposed CARMA array. The model disk from which the interferometric images are simulated is presented in the panel at bottom right. From Mundy et al. (2000).

pared with that imaged by CARMA. In this case, the model is shown in the lower right panel, and consists of a 0.01 solar mass disk around a star at the distance of the Taurus molecular cloud (~150 pc). The model disk has an inner and outer radius of 20 and 120 AU, respectively, with power law surface density and temperature distributions that match the millimeter continuum emission of measured disks. In the simulation, the observations utilize only existing configurations for BIMA and OVRO and proposed configurations for CARMA. The noise levels appropriate for each array, under good weather conditions, are also included. Clearly, compared to the existing arrays, the CARMA image has much improved resolution and signal-to-noise, and in fact is the only array that cleanly resolves the central 40 AU diameter hole. Similar or ever larger holes have been observed with scattered light coronography of debris disks, and are argued to be a signpost of planet formation. CARMA will enable similar studies to be conducted at much earlier times.

With about 40% of the collecting area of the originally proposed NRAO Millimeter Array and similar baselines, CARMA represents a major leap in the capabilities of university-based arrays. It can be operational in as little as three to four years, and as such would permit a host of new scientific programs to be carried out during ALMA construction. Upon the completion of ALMA, CARMA will be an excellent northern hemisphere complement to this large array, especially in light of the student access that is anticipated.

5.3 The Atacama Large Millimeter Array (ALMA)

Near the end of this decade, the Atacama Large Millimeter Array (or ALMA) will come into operation. This collaborative effort between the United States, Europe, and Japan aims to construct a 64 element array of 12 meter telescopes at the extraordinarily dry Chajantor plateau in northern Chile.

With its dramatic increase in collecting area and improved atmospheric conditions, ALMA will be able to image the dust and line emission from pre-planetary accretion disk in extraordinary detail. Figure 5.3, courtesy of Lee Mundy at the University of Maryland, illustrates well the expected capabilities of ALMA. The disk has a central hole 3 AU in radius, a roughly 2 AU wide cleared ring centered at 7 AU with a soft edge, a protoplanet overdensity at 9 AU with a Gaussian FWHM of 2 AU and a factor of 9 overdensity, a protoplanet overdensity at 22 AU with a Gaussian FMWH of 1.5 AU and a factor of 6

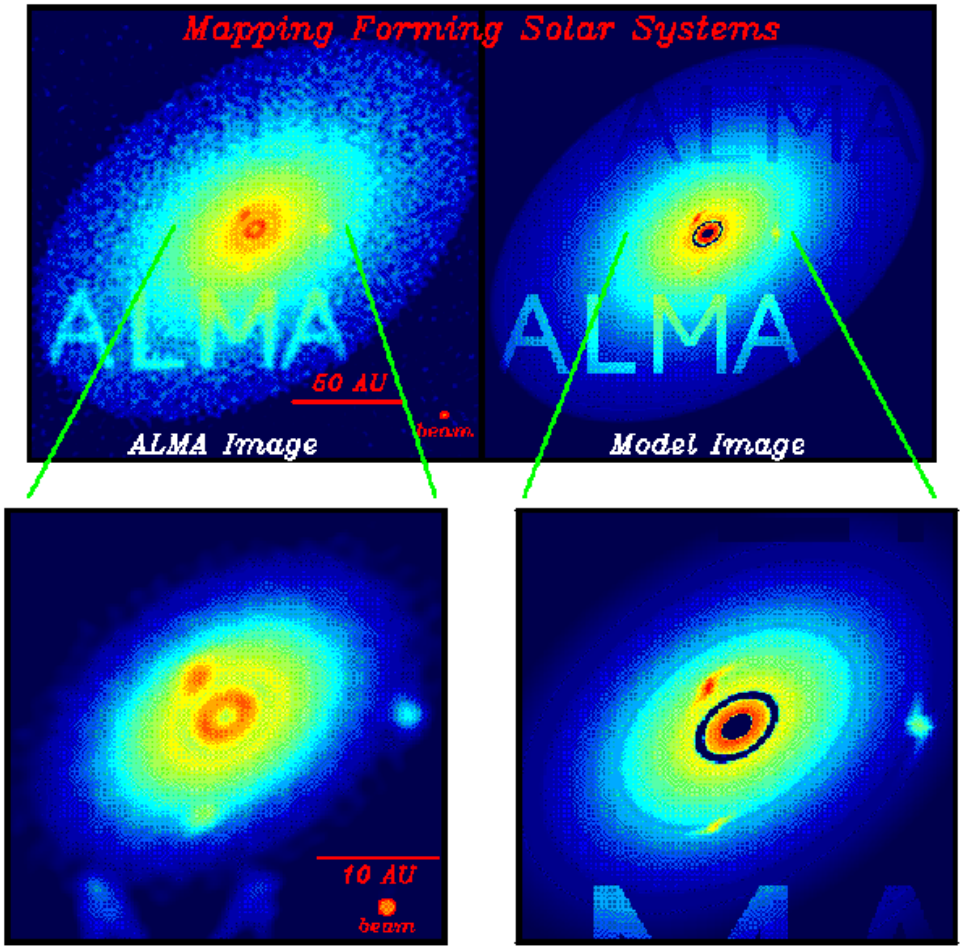

Figure 5.3: Circumstellar disk/protoplanet dust continuum imaging with a single transit in the highest resolution mode of ALMA. Provided by Lee Mundy.

overdensity, and a protoplanet overdensity at 37 AU with a Gaussian FWHM of 3 AU and a factor of 4 overdensity. Each of the protoplanets also has an underdensity of 10 percent in a ring at the same orbital radius. To test the image fidelity, the word ALMA is written in the lower part of the disk with an overdensity of a factor of 2 compared to the underlying disk. The letters are 12 pixels wide and 100 pixels high - that is roughly 4 AU by 35 AU. The word ALMA is also written in the upper part of the disk with an underdensity of 20 percent. The model images are at right, while the simulations from a single ALMA transit with perfect phase calibration but the estimated thermal noise level lie at left. The protoplanets are clearly visible, and chemical gradients such as those discussed in this thesis should be extremely well resolved. Given the rapid degradation in image sensitivity with resolution, only ALMA will make it possible to examine the chemical evolution of circumstellar disks in the terrestrial planet forming zone.

ALMA will also permit the rapid imaging of all comets, including short period comets, within a few AU of the Earth. For the vast majority of short period comets, ALMA will make possible the first measurements of the critical (D/H) ratio in water, as well as the detection of a variety of other rarer isotopomers and complex molecules. By examining a wide range of comets and comparing their composition to that derived for objects in the Kuiper belt, it may well become possible to extract radial gradients in the composition of outer solar system bodies just as such gradients are now observed in the asteroid belt. Combined with our vastly improved understanding of the properties and evolution of circumstellar accretion disks, the next generation of (sub)millimeter-wave interferometers will play pivotal roles in our understanding of the formation of planetary systems such as our own.

Bibliography

Adams, F. C., Lada, C. J., & Shu, F. H. 1987, ApJ, 312, 788

Aikawa, Y. & Herbst, E. 1999, ApJ, 526, 314

Aikawa, Y., Miyama, S. M., Nakano, T., & Umebayashi, T. 1996, ApJ, 467, 684

Aikawa, Y., Umebayashi, T., Nakano, T., & Miyama, S. 1998, in Chemistry and Physics of Molecules and Grains in Space. Faraday Discussions No. 109, 281

Aikawa, Y., Umebayashi, T., Nakano, T., & Miyama, S. M. 1997, ApJ, 486, L51

—. 1999, ApJ, 519, 705

Altenhoff, W. J., Bieging, J. H., Butler, B., Butner, H. M., Chini, R., Haslam, C. G. T., Kreysa, E., Martin, R. N., Mauersberger, R., McMullin, J., Muders, D., Peters, W. L., Schmidt, J., Schraml, J. B., Sievers, A., Stumpff, P., Thum, C., von Kap-Herr, A., Wiesemeyer, H., Wink, J. E., & Zylka, R. 1999, A&A, 348, 1020

Appenzeller, I., Oestreicher, R., & Jankovics, I. 1984, A&A, 141, 108

Bauer, I., Finocchi, F., Duschl, W. J., Gail, H. ., & Schloeder, J. P. 1997, A&A, 317, 273

Beckwith, S. V. W. & Sargent, A. I. 1993, in Protostars and Planets III, 521–541

Beckwith, S. V. W. & Sargent, A. I. 1996, Nature, 383, 139

Beckwith, S. V. W., Sargent, A. I., Chini, R. S., & Guesten, R. 1990, AJ, 99, 924

Bergin, E. A. & Langer, W. D. 1997, ApJ, 486, 316+

Bird, M. K., Huchtmeier, W. K., Gensheimer, P., Wilson, T. L., Janardhan, P., & Lemme, C. 1997, A&A, 325, L5

Biver, N., Bockelée-Morvan, D., Colom, P., Crovisier, J., Davies, J. K., Dent, W. R. F., Despois, D., Gerard, E., Lellouch, E., Rauer, H., Moreno, R., & Paubert, G. 1997a, Science, 275, 1915

Biver, N., Bockelée-Morvan, D., Colom, P., Crovisier, J., Germain, B., Lellouch, E., Davies, J. K., Dent, W. R. F., Moreno, R., Paubert, G., Wink, J., Despois, D., Lis, D. C., Mehringer, D., Benford, D., Gardner, M., Phillips, T. G., Gunnarsson, M., Rickman, H., Winnberg, A., Bergman, P., Johansson, L. E. B., & Rauer, H. 1997b, Earth Moon and Planets, 78, 5

Biver, N., Rauer, H., Despois, D., Moreno, R., Paubert, G., Bockelée-Morvan, D., Colom, P., Crovisier, J., Gerard, E., & Jorda, L. 1996, Nature, 380, 137

Blake, D., Allamandola, L., Sandford, S., Hudgins, D., & Freund, F. 1991, Science, 254, 548

Blake, G. A., Qi, C., Hogerheijde, M. R., Gurwell, M. A., & Muhleman, D. O. 1999, Nature, 398, 213

Bockelée-Morvan, D., Gautier, D., Lis, D. C., Young, K., Keene, J., Phillips, T., Owen, T., Crovisier, J., Goldsmith, P. F., Bergin, E. A., Despois, D., & Wootten, A. 1998, Icarus, 133, 147

Bockelée-Morvan, D., Lis, D. C., Wink, J. E., Despois, D., Crovisier, J., Bachiller, R., Benford, D. J., Biver, N., Colom, P., Davies, J. K., Gérard, E., Germain, B., Houde, M., Mehringer, D., Moreno, R., Paubert, G., Phillips, T. G., & Rauer, H. 2000, A&A, 353, 1101

Bockelée-Morvan, D. & Rickman, H. 1997, in First International Conference on Comet Hale-Bopp, Vol. 79, 55–77

Bouvier, J., Covino, E., Kovo, O., Martin, E. L., Matthews, J. M., Terranegra, L., & Beck, S. C. 1995, A&A, 299, 89

Chiang, E. I. & Goldreich, P. 1997, ApJ, 490, 368

Chiang, E. I., Joung, M. K., Creech-Eakman, M. J., Qi, C., Kessler, J. E., Blake, G. A., & van Dishoeck, E. F. 2001, ApJ, 547, 1077

Choi, M., Evans, N. J., Gregersen, E. M., & Wang, Y. 1995, ApJ, 448, 742

Combi, M. R. 1989, Icarus, 81, 41

Crovisier, J. 1987, A&AS, 68, 223

—. 1994, J. Geophys. Res., 99, 3777

D'Alessio, P., Calvet, N., & Hartmann, L. 1997, ApJ, 474, 397

D'Alessio, P., Calvet, N., Hartmann, L., Lizano, S., & Cantó, J. 1999, ApJ, 527, 893

D'Alessio, P., Canto, J., Calvet, N., & Lizano, S. 1998, ApJ, 500, 411

de Pater, I., Forster, J. R., Wright, M., Butler, B. J., Palmer, P., Veal, J. M., A'Hearn, M. F., & Snyder, L. E. 1998, AJ, 116, 987

de Pater, I., Palmer, P., & Snyder, L. E. 1991, in IAU Colloq. 116: Comets in the post-Halley era, 175–207

Devine, D., Grady, C., Kimble, R., Plait, P., Linsky, J., Woodgate, B., Boggess, A., & Bruhweiler, F. C. 1999, in American Astronomical Society Meeting, Vol. 195, 0207

Devine, D., Grady, C. A., Kimble, R. A., Woodgate, B., Palunas, P., & Linsky, J. L. 2000, in American Astronomical Society Meeting, Vol. 197, 0809+

Dutrey, A., Guilloteau, S., Duvert, G., Prato, L., Simon, M., Schuster, K., & Menard, F. 1996, A&A, 309, 493

Dutrey, A., Guilloteau, S., & Guelin, M. 1997, A&A, 317, L55

Duvert, G., Guilloteau, S., Ménard, F., Simon, M., & Dutrey, A. 2000, A&A, 355, 165

Eberhardt, P., Krankowsky, D., Schulte, W., Dolder, U., Lammerzahl, P., Berthelier, J. J., Woweries, J., Stubbemann, U., Hodges, R. R., Hoffman, J. H., & Illiano, J. M. 1987, A&A, 187, 481

Eberhardt, P., Reber, M., Krankowsky, D., & Hodges, R. R. 1995, A&A, 302, 301

Emerson, D. 1996, "Interpreting astronomical spectra" (Chichester, UK: Wiley, —c1996)

Fernandez, Y. R., A'Hearn, M. F., Kundu, A., Lisse, C. M., Weaver, H. A., Dayal, A., Hanner, M. S., Ressler, M. E., Hoffmann, W. F., Deutsch, L. K., Fazio, G. G., Hora, J. L., & Kaufl, H. U. 1997, in American Astronomical Society Meeting, Vol. 191, 7210

Festou, M. C., Rickman, H., & West, R. M. 1993, A&A Rev., 4, 363

Finocchi, F. & Gail, H. . 1997, A&A, 327, 825

Finocchi, F., Gail, H. ., & Duschl, W. J. 1997, A&A, 325, 1264

Flammer, K. R., Mendis, D. A., & Houpis, H. L. F. 1998, ApJ, 494, 822

Fomenkova, M. & Chang, S. 1997, Meteoritics & Planetary Science, vol. 32, page A44, 32, 44

Fuente, A., Martin-Pintado, J., Cernicharo, J., & Bachiller, R. 1993, A&A, 276, 473

Gammie, C. F. 1996, ApJ, 457, 355+

Gautier, D. & Morel, P. 1997, A&A, 323, L9

Gibb, E. L., Whittet, D. C. B., Schutte, W. A., Boogert, A. C. A., Chiar, J. E., Ehrenfreund, P., Gerakines, P. A., Keane, J. V., Tielens, A. G. G. M., van Dishoeck, E. F., & Kerkhof, O. 2000, ApJ, 536, 347

Glassgold, A. E., Najita, J., & Igea, J. 1997, ApJ, 480, 344

Grady, C. A., Devine, D., Woodgate, B., Kimble, R., Bruhweiler, F. C., Boggess, A., Linsky, J. L., Plait, P., Clampin, M., & Kalas, P. 1999, in American Astronomical Society Meeting, Vol. 195, 0208

Grady, C. A., Devine, D., Woodgate, B., Kimble, R., Bruhweiler, F. C., Boggess, A., Linsky, J. L., Plait, P., Clampin, M., & Kalas, P. 2000, ApJ, 544, 895

Green, S., Maluendes, S., & McLean, A. D. 1993, ApJS, 85, 181

Greenberg, J. M. & Li, A. 1999, Planet. Space Sci., 47, 787

Guilloteau, S. & Dutrey, A. 1998, A&A, 339, 467

Habing, H. J., Dominik, C., Jourdain de Muizon, M., Kessler, M. F., Laureijs, R. J., Leech, K., Metcalfe, L., Salama, A., Siebenmorgen, R., & Trams, N. 1999, Nature, 401, 456

Harmon, J. K., Ostro, S. J., Benner, L. A. M., Rosema, K. D., Jurgens, R. F., Winkler, R., Yeomans, D. K., Choate, D., Cormier, R., Giorgini, J. D., Mitchell, D. L., Chodas, P. W., Rose, R., Kelley, D., Slade, M. A., & Thomas, M. L. 1997, Science, 278, 1921

Hartmann, L., Calvet, N., Gullbring, E., & D'Alessio, P. 1998, ApJ, 495, 385

Hasegawa, T., Volk, K., & Kwok, S. 2000, ApJ, 532, 994

Herbig, G. H. & Goodrich, R. W. 1986, ApJ, 309, 294

Hirota, T., Yamamoto, S., Kawaguchi, K., Sakamoto, A., & Ukita, N. 1999, ApJ, 520, 895

Hogerheijde, M. R. & van der Tak, F. F. S. 2000, A&A, 362, 697

Hu, H., Larson, H. P., & Hsieh, K. C. 1991, Icarus, 91, 238

Huebner, W. F., Buhl, D., & Snyder, L. E. 1974, Icarus, 23, 580

Imhoff, C. L. & Appenzeller, I. 1987, "Pre-main sequence stars" (Exploring the Universe with the IUE Satellite), 295–319

Irvine, W. M., Bergin, E. A., Dickens, J. E., Jewitt, D., Lovell, A. J., Matthews, H. E. Schloerb, F. P., & Senay, M. 1998a, Nature, 393, 547

Irvine, W. M., Dickens, J. E., Lovell, A. J., Schloerb, F. P., Senay, M., Bergin, E. A., Jewitt, D., & Matthews, H. E. 1998b, in Chemistry and Physics of Molecules and Grains in Space. Faraday Discussions No. 109, 475

Irvine, W. M., Schloerb, F. P., Crovisier, J., Fegley, B., & Mumma, M. J. 2000, in Protostars and Planets IV (Book - Tucson: University of Arizona Press; eds Mannings, V., Boss, A.P., Russell, S. S.), p. 1159, 1159

Irvine, W. M., Schloerb, F. P., Hjalmarson, A., & Herbst, E. 1985, in Protostars and Planets II, 579–620

Jackson, W. M., Halpern, J. B., Feldman, P. D., & Rahe, J. 1982, A&A, 107, 385

Jacq, T., Walmsley, C. M., Henkel, C., Baudry, A., Mauersberger, R., & Jewell, P. R. 1990, A&A, 228, 447

Jansen, D. J., van Dishoeck, E. F., Black, J. H., Spaans, M., & Sosin, C. 1995, A&A, 302, 223

Jewitt, D. & Matthews, H. 1999, AJ, 117, 1056

Jewitt, D., Senay, M., & Matthews, H. E. 1996, Science, 271, 1110

Jewitt, D. C. & Matthews, H. E. 1997, AJ, 113, 1145

Johnstone, D. 2000, in Astrochemistry: From Molecular Clouds to Planetary Systems, IAU Symposium Vol. 197, 403–413

Johnstone, D., Hollenbach, D., & Bally, J. 1998, ApJ, 499, 758

Kastner, J. H., Zuckerman, B., Weintraub, D. A., & Forveille, T. 1997, Science, 277, 67

Kenyon, S. J. & Hartmann, L. 1987, ApJ, 323, 714

Koerner, D. W. & Sargent, A. I. 1995, AJ, 109, 2138

Koerner, D. W., Schneider, G., Smith, B. A., Becklin, E. E., Hines, D. C., Kirkpatrick, J. D., Lowrance, P. J., Meier, R., Reike, M., Terrile, R. J., Thompson, R. I., & NICMOS/IDT EONS Teams. 1998, in American Astronomical Society Meeting, Vol. 193, 7314

Koresko, C. D., Blake, G. A., Brown, M. E., Sargent, A. I., & Koerner, D. W. 1999, ApJ, 525, L49

Krist, J. E., Burrows, C. J., Stapelfeldt, K. R., & WFPC2 Id Team. 1997, in American Astronomical Society Meeting, Vol. 191, 0514

Lada, C. J., Muench, A. A., Haisch, K. E., Lada, E. A., Alves, J. ., Tollestrup, E. V., & Willner, S. P. 2000, AJ, 120, 3162

Lagrange-Henri, A. M., Vidal-Madjar, A., & Ferlet, R. 1988, A&A, 190, 275

Langer, W. D., van Dishoeck, E. F., Bergin, E. A., Blake, G. A., Tielens, A. G. G. M., Velusamy, T., & Whittet, D. C. B. 2000, in Protostars and Planets IV (Book - Tucson: University of Arizona Press; eds Mannings, V., Boss, A.P., Russell, S. S.), p. 29, 29+

Lay, O. P. 1997, A&AS, 122, 547

Licandro, J., Bellot Rubio, L. R., Boehnhardt, H., Casas, R., Goetz, B., Gomez, A., Jorda, L., Kidger, M. R., Osip, D., Sabalisck, N., Santos, P., Serr-Ricart, M., Tozzi, G. P., & West, R. 1998, ApJ, 501, L221

Luu, J. X. & Jewitt, D. C. 1990, AJ, 100, 913

Mannings, V., Koerner, D. W., & Sargent, A. I. 1997, Nature, 388, 555

Mannings, V. & Sargent, A. I. 1997, ApJ, 490, 792

—. 2000, ApJ, 529, 391

Marcy, G. W., Butler, R. P., Vogt, S. S., Fischer, D., & Liu, M. C. 1999, ApJ, 520, 239

Meier, R., Owen, T. C., Jewitt, D. C., Matthews, H. E., Senay, M., Biver, N., Bockelee-Morvan, D., Crovisier, J., & Gautier, D. 1998a, Science, 279, 1707

Meier, R., Owen, T. C., Matthews, H. E., Jewitt, D. C., Bockelee-Morvan, D., Biver, N., Crovisier, J., & Gautier, D. 1998b, Science, 279, 842

Millar, T. J., Bennett, A., Rawlings, J. M. C., Brown, P. D., & Charnley, S. B. 1991, A&AS, 87, 585

Montmerle, T. 1992, Memorie della Societa Astronomica Italiana, 63, 663

Moran, J. M. & Ho, P. T. 1994, Proceedings of SPIE, 2200, 335

Muhleman, D. O. & Berge, G. L. 1991, Icarus, 92, 263

Mumma, M. J., Weissman, P. R., & Stern, S. A. 1993, in Protostars and Planets III, 1177–1252

Mundy, L. G., Looney, L. W., Erickson, W., Grossman, A., Welch, W. J., Forster, J. R., Wright, M. C. H., Plambeck, R. L., Lugten, J., & Thornton, D. D. 1996, ApJ, 464, L169

Mundy, L. G., Scott, S. L., & Shepherd, D. S. 2000, in Imaging at Radio through Submillimeter Wavelengths. Edited by Jeff Mangum. Publisher: The Astronomical Society of the Pacific, Conference Series, 2000. The conference was held June 6-8, 1999, in Tucson, Arizona., E51–+

O'dell, C. R. & Wong, K. 1996, AJ, 111, 846

Ossenkopf, V. & Henning, T. 1994, A&A, 291, 943

Padgett, D. L., Brandner, W., Stapelfeldt, K. R., & Krist, J. E. 1999a, in American Astronomical Society Meeting, Vol. 195, 7902

Padgett, D. L., Brandner, W., Stapelfeldt, K. R., Strom, S. E., Terebey, S., & Koerner, D. 1999b, AJ, 117, 1490

Perley, R. A., Schwab, F. R., & Bridle, A. H., eds. 1989, "Synthesis imaging in radio astronomy"

Prasad, S. S. & Huntress, W. T. 1982, ApJ, 260, 590

Prialnik, D. 1997, ApJ, 478, L107

Rodgers, S. D. & Charnley, S. B. 1998, ApJ, 501, L227

Sagdeev, R. Z., Blamont, J., Galeev, A. A., Moroz, V. I., Shapiro, V. D., Shevchenko, V. I., & Szego, K. 1986, Nature, 321, 259

Samarasinha, N. H. & Belton, M. J. S. 1994, Icarus, 108, 103

Sargent, A. & Beckwith, S. 1994, in ASP Conf. Ser. 59: IAU Colloq. 140: Astronomy with Millimeter and Submillimeter Wave Interferometry, 203

Sargent, A. I. 1996, in IAU Symp. 170: CO: Twenty-Five Years of Millimeter-Wave Spectroscopy, Vol. 170, 151

Schilke, P., Walmsley, C. M., Pineau Des Forets, G., Roueff, E., Flower, D. R., & Guilloteau, S. 1992, A&A, 256, 595

Schleicher, D. G., Lederer, S. M., Millis, R. L., & Farnham, T. L. 1997, Science, 275, 1913

Schulze, H. & Stoffler, D. 1997, Meteoritics & Planetary Science, vol. 32, page A116, 32, 116

Scoville, N. Z., Carlstrom, J. E., Chandler, C. J., Phillips, J. A., Scott, S. L., Tilanus, R. P. J., & Wang, Z. 1993, Publ.. Astron. Soc. Pac., 105, 1482

Senay, M., Rownd, B., Lovell, A., Dickens, J., De Vries, C., Schloerb, F. P., Mayhew, L., Yuen, L. M., & Mauskopf, P. 1997, in AAS/Division of Planetary Sciences Meeting, Vol. 29, 3206

Shu, F., Najita, J., Galli, D., Ostriker, E., & Lizano, S. 1993, in Protostars and Planets III, 3–46

Shu, F. H., Adams, F. C., & Lizano, S. 1987, ARA&A, 25, 23

Siess, L., Dufour, E., & Forestini, M. 2000, A&A, 358, 593

Simon, M., Dutrey, A., & Guilloteau, S. 2001, ApJ, 545, 1034

Snyder, L. E., Veal, J. M., Woodney, L. M., Wright, M. C. H., Palmer, P., A'Hearn, M. F., Kuan, Y. ., de Pater, I., & Forster, J. R. 2001, AJ, 121, 1147

Spaans, M. 1996, in IAU Symp. 178: Molecules in Astrophysics: Probes & Processes, Vol. 178, 431

Stapelfeldt, K. & The WFPC2 Science Team. 1997, in Science with the VLT Interferometer, 395

Sternberg, A. & Dalgarno, A. 1995, ApJS, 99, 565

Strom, K. M., Strom, S. E., Edwards, S., Cabrit, S., & Skrutskie, M. F. 1989, AJ, 97, 1451

Thi, F. W. & et al. 2000, in IAU Symposium, Vol. 202, E84–+

Thompson, A. R., Moran, J. M., & Swenson, G. W. 1986, "Interferometry and synthesis in radio astronomy" (New York, Wiley-Interscience, 1986, 554 p.)

Tielens, A. G. G. M. & Hollenbach, D. 1985, ApJ, 291, 747

van Dishoeck, E. F. & Blake, G. A. 1995, Astrophys. Space. Sci., 224, 237

—. 1998, ARA&A, 36, 317

van Dishoeck, E. F., Blake, G. A., Jansen, D. J., & Groesbeck, T. D. 1995, ApJ, 447, 760

van Zadelhoff, G., van Dishoeck, E. F., Thi, W., & Blake, G. A. 2000, in IAU Symposia, Vol. 202, E98–

Ward, W. R. & Hahn, J. M. 2000, in Protostars and Planets IV (Book - Tucson: University of Arizona Press; eds Mannings, V., Boss, A.P., Russell, S. S.), p. 1135, 1135

Weaver, H. & Larmy, P. 1997, in First International Conference on Comet Hale-Bopp, Vol. 79, 17–33

Weaver, H. A., Brooke, T. Y., Chin, G., Kim, S. J., Bockelée-Morvan, D., & Davies, J. K. 1997, Earth Moon and Planets, 78, 71

Westley, M. S., Baragiola, R. A., Johnson, R. E., & Baratta, G. A. 1995, Nature, 373, 405

Willacy, K., Klahr, H. H., Millar, T. J., & Henning, T. 1998, A&A, 338, 995

Willacy, K. & Langer, W. D. 2000, ApJ, 544, 903

Woodney, L. M., A'Hearn, M. F., de Pater, I., Forster, J. R., Kuan, Y. ., Meier, R., Palmer, P., Snyder, L. E., Veal, J. M., & Wright, M. C. H. 1999, in AAS/Division of Planetary Sciences Meeting, Vol. 31, 1722

Wootten, A. 1987, in IAU Symp. 120: Astrochemistry, Vol. 120, 311–318

Wright, M. C. H., de Pater, I., Forster, J. R., Palmer, P., Snyder, L. E., Veal, J. M., A'Hearn, M. F., Woodney, L. M., Jackson, W. M., Kuan, Y. ., & Lovell, A. J. 1998, AJ, 116, 3018